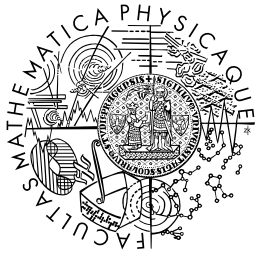

FACULTY
OF MATHEMATICS
AND PHYSICS
Charles University

DOCTORAL THESIS

Vladimír Novotný

Measurement of the energy spectrum of cosmic rays using Cherenkov–dominated data at the Pierre Auger Observatory

Institute of Particle and Nuclear physics

Supervisor of the doctoral thesis:	doc. RNDr. Dalibor Nosek, Dr.
Study programme:	Physics
Study branch:	Particle and Nuclear Physics

Prague 2020

I declare that I carried out this doctoral thesis independently, and only with the cited sources, literature and other professional sources.

I understand that my work relates to the rights and obligations under the Act No. 121/2000 Sb., the Copyright Act, as amended, in particular the fact that the Charles University has the right to conclude a license agreement on the use of this work as a school work pursuant to Section 60 subsection 1 of the Copyright Act.

In Prague, 15th April 2020 .....

Author's signature

Title: Measurement of the energy spectrum of cosmic rays using Cherenkov–dominated data at the Pierre Auger Observatory

Author: Vladimír Novotný

Institute: Institute of Particle and Nuclear physics

Supervisor: doc. RNDr. Dalibor Nosek, Dr., Institute of Particle and Nuclear physics

Abstract: This thesis presents the energy spectrum of cosmic rays deduced from Cherenkov–dominated data measured by the fluorescence detector of the Pierre Auger Observatory. Cherenkov–dominated events, used in the energy spectrum analysis at the Observatory for the first time, enable to decrease the energy threshold for the spectrum measurement down to $10^{15.5}$ eV. This energy is more than one order of magnitude lower than in preceding studies. The fluorescence detector was originally designed to detect the fluorescence light generated by extensive air showers in a hybrid mode with the surface detector of the Pierre Auger Observatory. The reconstruction of events dominated by Cherenkov light is available due to a newly developed reconstruction technique, the profile constrained geometry fit. Its implementation in the Pierre Auger Observatory software is documented. Aspects of the energy spectrum analysis are described. They consist of exposure calculations done with the use of extensive Monte Carlo simulations, unfolding of the detector effects, and inferring the invisible energy correction in the energy region below 10^{17} eV. Systematic uncertainties of the measurement are estimated.

Keywords: cosmic rays, energy spectrum, Cherenkov–dominated events, invisible energy, Pierre Auger Observatory

I would like to thank my supervisor Dalibor Nosek for all his extensive support throughout my studies and I am grateful to all members of the Institute of Particle and Nuclear Physics for their help whenever it was needed. I also thank my colleagues from the Institute of Physics of the Czech Academy of Sciences, namely to Jakub Vícha, Jan Ebr, Jiří Blažek, and my consultant Petr Trávníček for very fruitful discussions. On top of that, I greatly appreciate all the help from the Pierre Auger Collaboration without which the presented work would not be possible to be done.

Special thanks go to Stanislav Štefánik, Michal Kloc, and Tomáš Kadavý for providing me with a very pleasant atmosphere not only during my work.

I am very grateful to my family and especially my wife for supporting me all the time. I would like to dedicate this thesis to my daughters Barborka and Zuzanka.

Contents

Introduction

The study of cosmic rays is one of fundamental topics of the particle physics. Unlike in accelerator studies, a primary beam of charged particles that reach the Earth from space is not controlled by experimentalists. This fact determines some of the basic questions of the astroparticle physics, especially those about the origin of cosmic rays, about their type, and about their propagation through the Universe. In experiments, only properties of particles that reach the observer can be studied.

This work focuses on the energy spectrum of cosmic rays. Specifically, the energy region of $10^{16} - 10^{18}$ eV is investigated. A special subset of the data taken by the fluorescence detector of the Pierre Auger Observatory is used. Unlike in the preceding studies done at the Observatory, the Cherenkov–dominated events are processed.

The Author was involved in all aspects of the analysis of the Cherenkov–dominated data, starting from a detailed description of the trigger system in the detector simulations, going through the codes that are used for the reconstruction of events, and ending in the analysis of the energy spectrum. In addition, the Author also studied in detail the multiple–eye reconstruction [A1, A2, A3] and its utilization in the search for events propagating with anomalous velocity [A4, A5, A6]. He also investigated mass–dependent parameters of air showers with anomalous longitudinal profiles [A7] and described the muon production depth in the context of the Heitler–Matthews's model of extensive air showers [A8]. Particular contributions are specified in the text.

This thesis consists of three Chapters. In Chapter 1, the basic information about extensive air showers initiated by cosmic rays is given together with the description of detection methods that are implemented at the Pierre Auger Observatory. Chapter 2 is focused on techniques that are used to reconstruct the parameters of extensive air showers and summarizes previous results of the Observatory related to this work. Details of the analysis of the energy spectrum from Cherenkov–dominated data, main results, and their interpretation are given in Chapter 3.

1. Cosmic rays at the Pierre Auger Observatory

The Pierre Auger Observatory is the world's largest experiment that measure extensive air showers (EASs) induced by cosmic rays (CRs). It is designed as a hybrid detector that combines an array of water–Cherenkov stations and fluorescence telescopes. The main purpose of the Observatory is to measure the ultra high energy cosmic rays (UHECRs) with energies above 10^{18} eV. Due to the rapid decrease of the flux of CRs in this region, as shown in Fig. 1.1, the dimensions of the Observatory are extreme. The Observatory is located in the Mendoza province, Argentina. The surface detector (SD) covers an area of $\sim$ 3000 km^2 and is overlooked by the fluorescence detector (FD) placed at four sites. Their construction was completed in 2008. During over 10 years of operation, the largest–ever collection of CR showers has been acquired. Further details are given in Section 1.3 and can be found also in Refs. [1, 2].

This Chapter is partially based on the Author's Master's thesis [A1]. In Section 1.1, the energy spectrum of cosmic rays as it has been measured by different experiments is presented. It is the most decisive parameter which determines the detection techniques that can be used to measure CRs in a particular energy range. The detection methods itself are summarized in Section 1.3. Section 1.2 gives a brief description of EASs and methods of their simulation.

1.1 Flux of cosmic rays

The term flux of CRs is used in this thesis for a quantity expressed in the units of $(\text{m}^2\ \text{s}\ \text{sr}\ \text{eV})^{-1}$ or equivalent. This quantity is also commonly named the intensity of CRs and more generally the energy spectrum of CRs.

In Fig. 1.1, the flux of CRs compiled from recent experiments is depicted. An overall power law trend following a cubic decrease with energy ($\sim E^{-3}$) is visible. A detailed view of the high–energy part of the spectrum is shown in Fig. 1.2. In this figure, the flux of CRs is multiplied by energy to 2.6 ($E^{2.6}$) to point out the features that deviate from the overall trend. The most important features are the Knee at the energy of about $10^{15.5}$ eV and the Ankle at about $10^{18.7}$ eV. The so called 2$^{\text{nd}}$ Knee around 10^{17} eV is addressed in detail in Chapter 3.

Above 10^{14} eV, the flux is too low that a direct detection of CRs is hardly possible. As a consequence, the extensive air showers of secondary particles are used to detect the incoming primaries. The rate of incoming CRs around the Ankle region is as low as 1 particle/km^2/year which implies the necessity of a large collection area that needs to be covered by any potential detector of UHECRs.

1.2 Extensive air showers

After a primary CR particle hits the Earth's atmosphere, an extensive air shower (EAS) composed of secondary particles is produced. EASs provide us with the

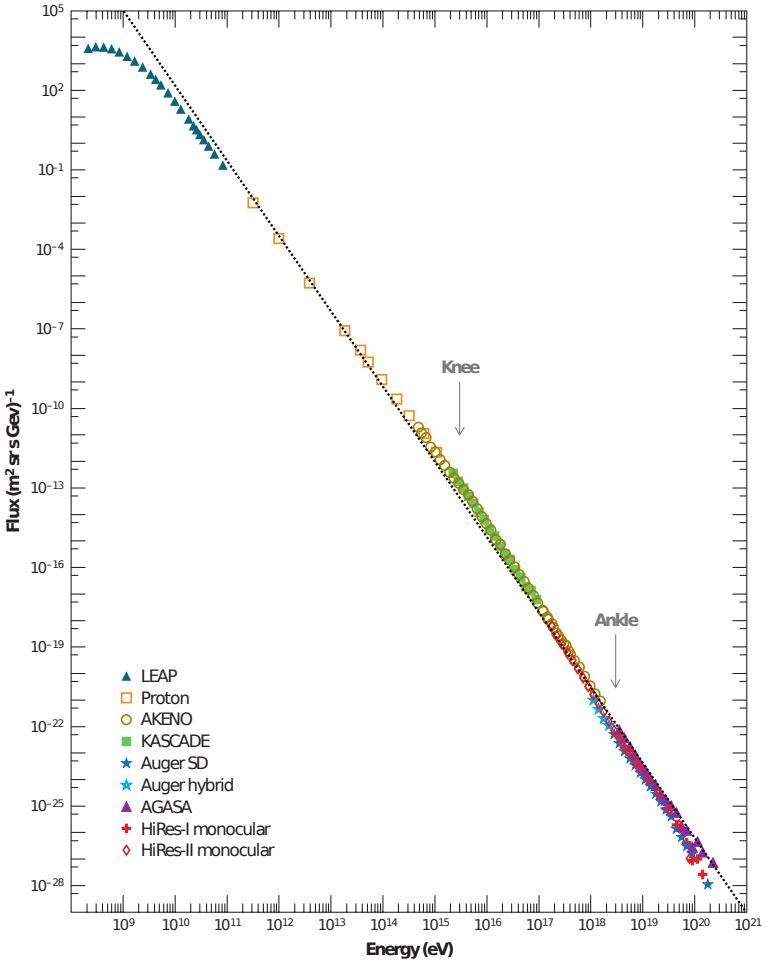

Figure 1.1: Energy spectrum of CRs in the energy range of $10^8 - 10^{21}$ eV. Knee and Ankle regions are marked. Overall trend following a cubic decrease with energy is shown by dotted line. Picture is adopted from Ref. [3].

best information about the most energetic CRs that is available. In the EAS, four components can be distinguished

- Electromagnetic (EM) component is composed by electrons, positrons, and photons created through neutral pion decay. The numbers of photons and electrons are very closely linked. A vast majority of particles arriving at the ground level are photons, followed by electrons. The EM component is responsible for the largest amount of energy which is deposited in the atmosphere by EAS. It also produces the dominant part of the Cherenkov radiation.

- Muonic component consists of muons which are the third most abundant particles arriving to the ground. Muons come from π^+, π^-, K^+, and K^- decays. This component also feeds the EM component through the decays of muons.

- Hadronic component is formed by remnants of smashed air molecules and atoms, and also by protons, neutrons, pions, and kaons. This component is less abundant at the ground level. It is difficult to detect it due to the small

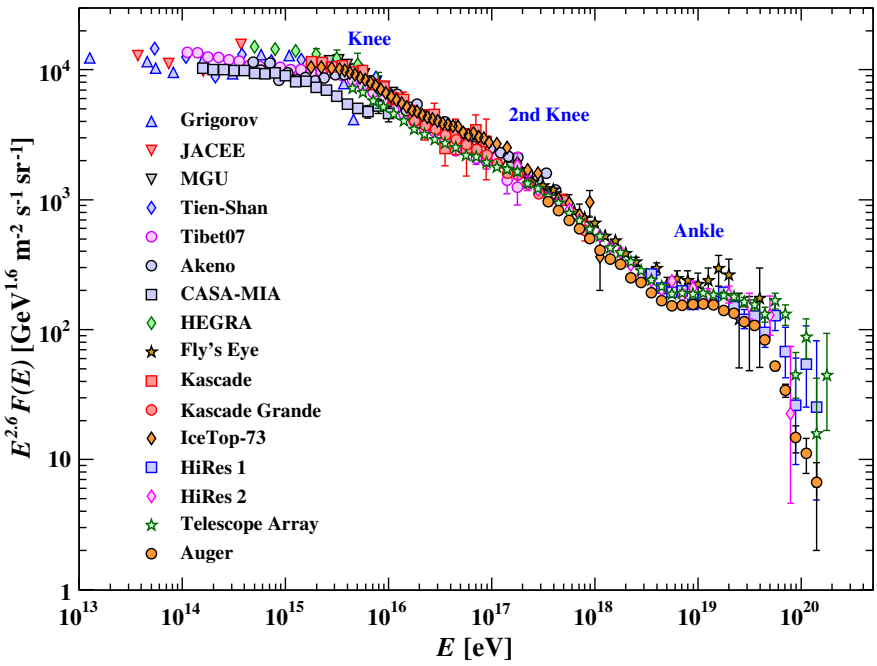

Figure 1.2: Energy spectrum of CRs from air shower data obtained in different experiments. The flux of CRs is multiplied by energy to 2.6. Picture is taken from Ref. [4].

size of its footprint on the ground. It gives rise to all other components into which it is transformed very fast.

- Neutrinos are not visible in detectors of CRs. They originate in the decays of shower pions, muons, and kaons. The energy taken away by neutrinos is related to the energy carried by muons.

A schema of the components of EAS is shown in Fig. 1.3.

1.2.1 Air shower simulations

To derive properties of the primary particle from detected air shower, a theoretical prediction of the EAS is necessary. The most simple description is the Heitler's model [6] valid for EM showers. In the case of hadron–initiated showers, the Heitler–Matthews's model [7] may be adopted. These models can be used to estimate even complex features of EASs like the muon production depth, see Ref. [A8]. Unfortunately, these simple analytical models predict only the average development of EASs. They provide no information about fluctuations in shower evolution which are essential in many cases. Because of that, the sophisticated Monte Carlo simulation codes have to be used to make reliable predictions of the shower properties.

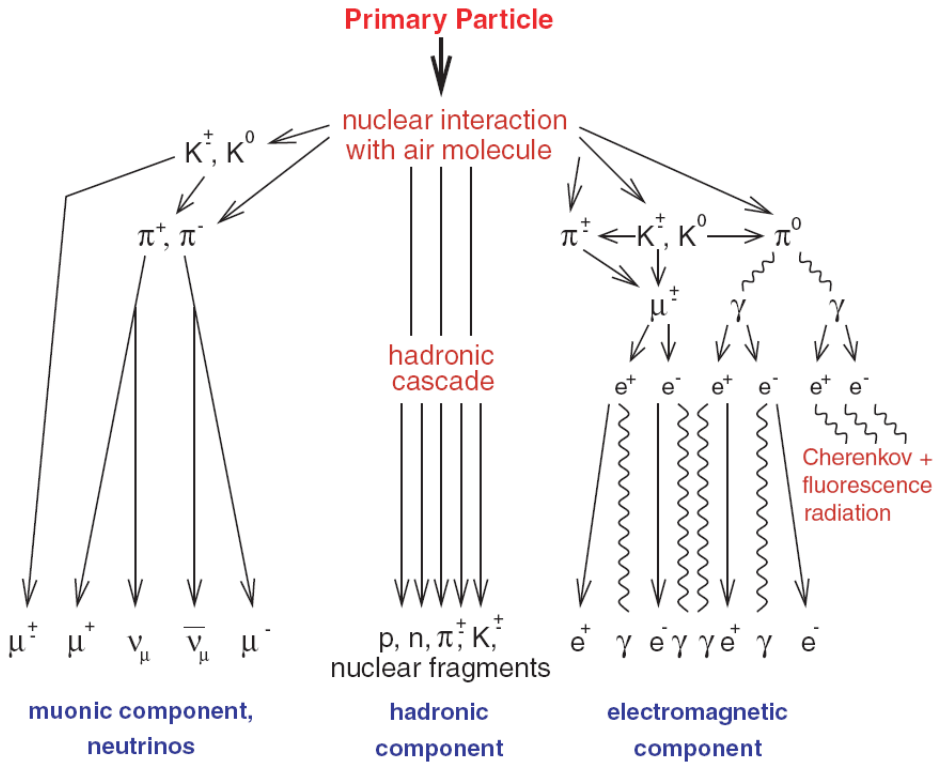

Figure 1.3: Components of a secondary EAS induced by a primary CR particle of high energy. Picture comes from Ref. [5].

In this work, two simulation codes are used. The CONEX program [8] is widely utilized to prepare simulations where a large sample is needed. Besides, the CORSIKA code [9] is used to cross-check and tune the details of the model of Cherenkov light production in EASs, see Appendix A. An advantage of CONEX is in a much faster simulation because it utilizes cascade equations to predict the number of particles at latter stages of the EAS. A disadvantage is in a purely 1D simulation that results only in longitudinal profiles of the number of particles and energy deposit in air. The opposite holds for CORSIKA. It evaluates each particle of EAS in detail and produces a 3D description of EASs at the cost of a long computation time.

The longitudinal profile of the shower, $N(X)$, is usually parametrized by the Gaisser-Hillas's (GH) function [10]

$$N(X) = N_{\max}\left(\frac{X - X_0}{X_{\max} - X_0}\right)^{\frac{X_{\max}-X_0}{\lambda}} \exp\left(\frac{X_{\max} - X}{\lambda}\right). \tag{1.1}$$

Here X stands for the atmospheric slant depth at altitude h

$$X(h) = \int_h^\infty \frac{\rho(l)}{\cos\theta} \mathrm{d}l, \tag{1.2}$$

where $\rho(l)$ is the density of air at altitude l and θ is the local zenith angle of the shower axis. In Eq. (1.1), $X_{\max}$ denotes the depth of shower maximum, X_0 and λ are shape parameters, and $N_{\max}$ is the size of EAS in its maximum. Two simulated profiles of showers induced by proton and iron nucleus are shown in

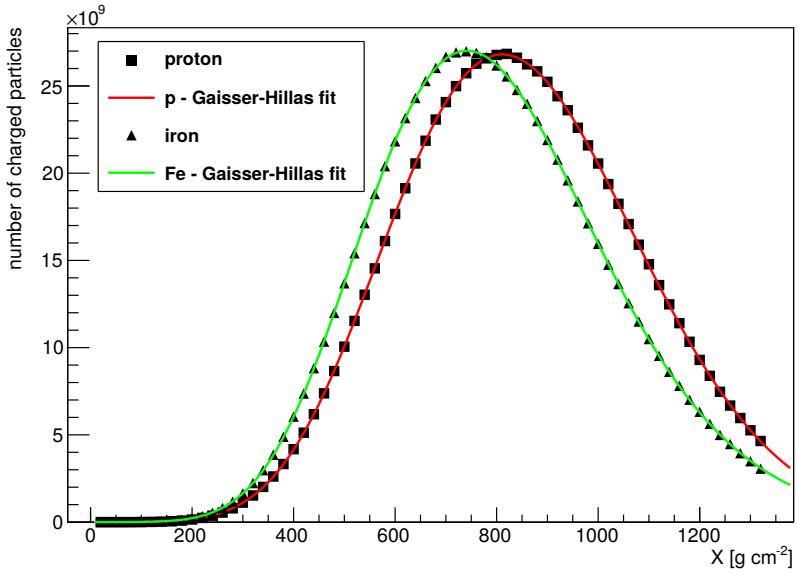

Figure 1.4: Longitudinal profile of EAS initiated by proton and Fe nucleus represented by squares and triangles, respectively. GH fits are shown by solid lines. Picture is taken from Ref. [A1].

Fig. 1.4 by squares and triangles, respectively. The GH fits are depicted as well by solid lines.

The central part of both above mentioned Monte Carlo simulation programs consists of a high–energy interaction model. Currently, three main models are used in the astroparticle community – EPOS LHC [11, 12], QGSJetII-04 [13, 14], and Sibyll 2.3c [15, 16]. They differ between each other in a theoretical approach that is used to calculate particle interactions. Although all of them are tuned to the current LHC data, their predictions are not quantitatively consistent. Nevertheless, qualitative trends are similar in all models. It is illustrated by predicted averages, $\langle X_{\max} \rangle$, and standard deviations, $\sigma_{X_{\max}}$, of the $X_{\max}$ distributions that are shown in Fig. 1.5. The prodictions for EPOS LHC, QGSJetII-04, and Sibyll 2.3c are shown in this figure. Particular choice of the model is important in the interpretation of EAS parameters related to the mass composition of primaries as described in the next Section 1.2.2.

1.2.2 Mass composition

Even from the simple analytical Heitler–Matthews's model [6, 7], two parameters of EASs that are related to the mass of primary particles can be derived. They are $X_{\max}$ and the number of muons that reach the ground, N_μ. In analytical calculations, the superposition model is usually applied. It assumes that an interaction of a nucleus with the mass number A and the total energy E_0 initiates the same shower as A interactions of a proton with the energy of E_0/A. In the context of Heitler–Matthews's and superposition models, the following equations

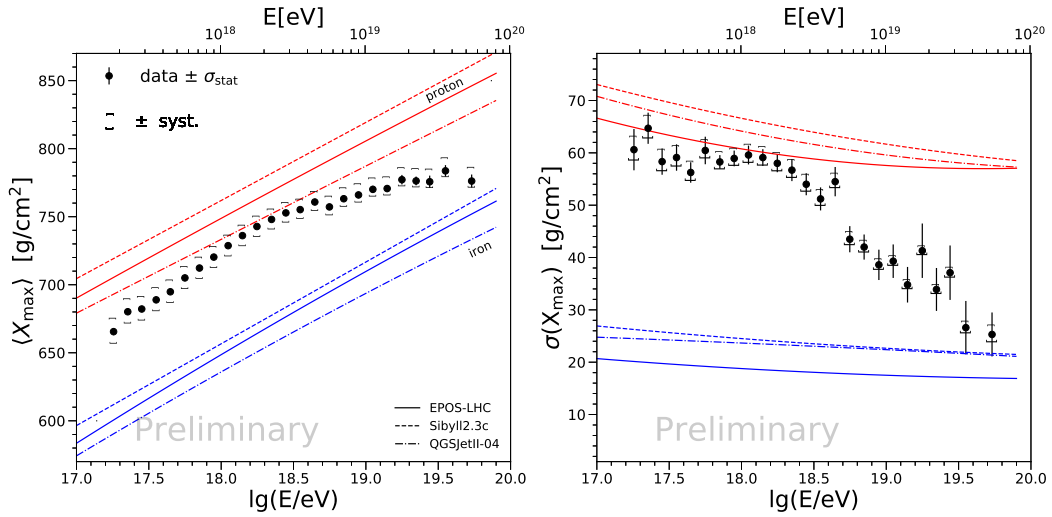

Figure 1.5: Average (left) and standard deviation (right) of $X_{\rm max}$ distributions measured at the Pierre Auger Observatory (points). Predictions of high–energy interaction models are shown by solid, dashed, and dashed–dotted lines for EPOS LHC, QGSJetII-04, and Sibyll 2.3c, respectively. Pictures are taken from Ref. [18].

hold for $X^A_{\rm max}$ and N^A_μ [17]

$$X^{\rm p}_{\rm max} = \lambda_i^{\rm p-air} \ln 2 + X_0 \ln \left(\frac{\kappa E_0}{3 N_{\rm ch} \epsilon_{\rm c}^e} \right), \tag{1.3}$$

$$X^A_{\rm max} = X^{\rm p}_{\rm max} - X_0 \ln A, \tag{1.4}$$

$$\beta = \frac{\ln N_{\rm ch}}{\ln \frac{3}{2} N_{\rm ch}}, \tag{1.5}$$

$$N^A_\mu = \left(\frac{E_0}{\epsilon_{\rm c}^\pi} \right)^\beta A^{1-\beta}, \tag{1.6}$$

where $\lambda_i^{\rm p-air}$ is the interaction length of a primary proton, X_0 is the radiation length, κ is the inelasticity of interactions, ϵ_c^e and ϵ_c^π are the critical energies for electrons and pions[1)] , respectively, and $N_{\rm ch}$ is the number of charged pions produced after one interaction length. These simple properties of shower development are used in estimating the invisible energy carried away by neutrinos and other undetected particles, see Section 3.1.

In practice, results of the mass analysis are compared with air shower simulations. As an example, the measurement of an average and a standard deviation of the $X_{\rm max}$ distributions performed at the Pierre Auger Observatory in the energy range of $10^{17.2} - 10^{19.9}$ eV is depicted in Fig. 1.5. N_μ used as a mass composition estimator is shown in Fig 1.6, where the measurement of the average muon density at the ground done by the IceTop experiment is depicted.

With the use of simulations done with a particular high–energy interaction model, the moments of measured quantities can be translated into the moments

[1)] The critical energy of pions is defined here as the energy at which the probability of interaction of charged pions is the same as the probability of their decay.

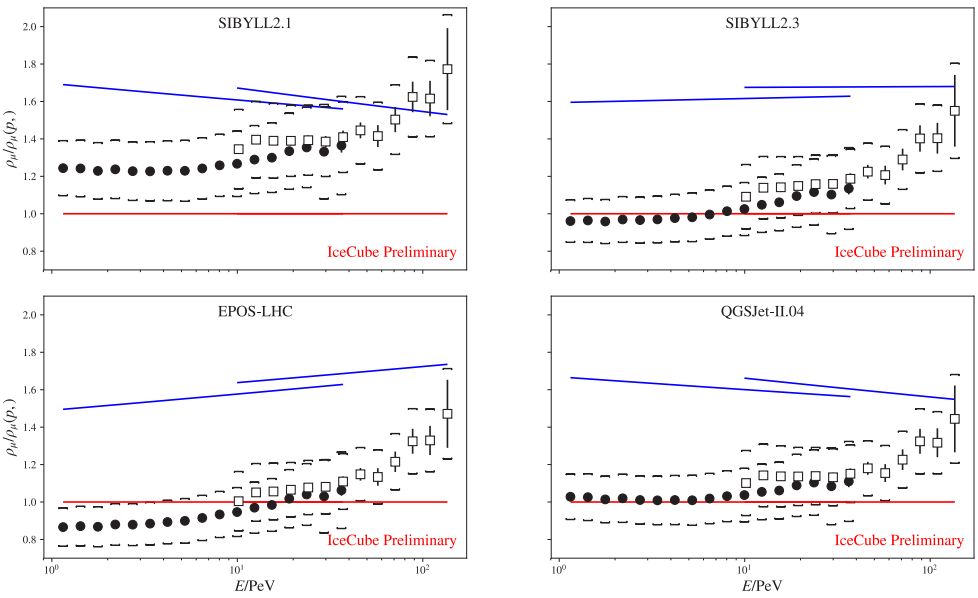

Figure 1.6: Muon densities measured by the IceTop experiment. Values are normalized to the densities obtained for proton initiated showers. Calculations are done with four high–energy interaction models that label insets. Predictions for pure proton and iron nucleus primary beams are shown by red and blue lines, respectively. Circles and squares correspond to the IceTop measurements at lateral distances of 600 m and 800 m, respectively. Figure comes from Ref. [19].

of logarithmic mass, $\ln A$, of the primary beam. Such calculations are done by each experiment separately, but also the global spline fit (GSF) approach which takes into account the differences in energy scales of individual experiments was presented in Ref. [20]. Estimates of the average $\ln A$ together with the fitted fluxes of individual CR components done within the GSF model are shown in Fig. 1.7.

1.3 Detection methods

EASs can be measured by several techniques. Some of the techniques, as implemented at the Pierre Auger Observatory, are briefly described in this Section.

Two categories of detectors are distinguished. The first type provides us with the information about the longitudinal profile of showers and the second type measures evolution in one level of shower development only. The first category is represented by the fluorescence detector (FD) that is described in Section 1.3.1. In addition, the measurement of radio emission from EASs falls partially into this category, see Section 1.3.3. Various types of particle detectors that work in coincidence are classified into the second category of detectors. They can either be placed on the groud like the surface detector (SD) array of the Pierre Auger Observatory introduced in Section 1.3.2, or under the ground like the Auger Muons and Infill for the Ground Array (AMIGA) mentioned in Section 1.3.3. Moreover, the detectors can either be more sensitive to the EM or the muonic

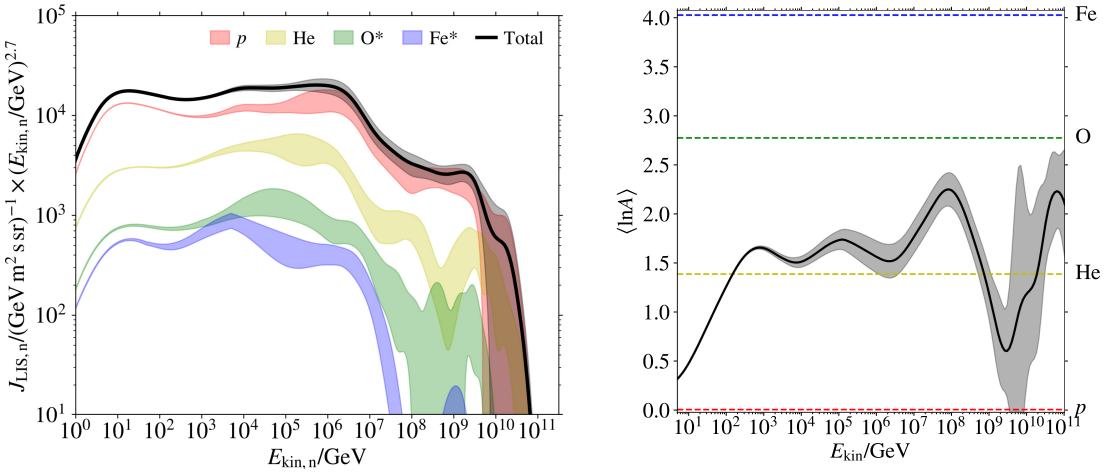

Figure 1.7: Individual components of CR flux (left) together with the average logarithmic mass, $\langle \ln A \rangle$ (right) fitted within the GSF model. Results of several experiments are combined. Pictures are based on Ref. [20] and produced by Hans Dembinski for the UHECR 2018 conference.

component of EASs. It gives us further possibilities to distinguish between masses of primary particles. Also the description of EASs by Monte Carlo simulation codes is challenged by these measurements.

A great advantage of the Pierre Auger Observatory is in the hybrid regime of the detection. The subset of showers that are registered by both the SD and the FD forms a calibration sample where the SD energy scale is adjusted to the energies measured by the FD which suffer from much lower systematic uncertainties. This approach is described in Section 2.10.

Map of the Pierre Auger Observatory is shown in Fig. 1.8. It is located near the city of Malargüe in Argentina. An altitude of the Observatory is about 1400 m a.s.l which corresponds to about 875 g cm^{-2}. Four FD stations and the SD array are depicted. Blue lines and black points correspond to the field of view of the FD telescopes and positions of individual stations of the SD, respectively.

1.3.1 Fluorescence telescopes

The FD is an essential instrument used in this thesis. At the Pierre Auger Observatory, it is realized by 27 telescopes that are designed to measure the air fluorescence light induced by EASs. They are situated at four stations named Los Leones, Los Morados, Loma Amarilla and Coihueco. At each site, 6 telescopes share the same building as depicted in Fig 1.9. On top of that, 3 telescopes of the High Elevation Auger Telescopes (HEAT) are placed about 170 m apart from the main building of the Coihueco station in a separate cover. The field of view of HEAT is shown by orange lines in Fig. 1.8. All telescopes overlook the SD array and have the same field of view of 30° azimuthally and 28.1° vertically. All 24 telescopes in the main buildings look at the fixed elevation of 1.51° above horizon and HEAT covers an elevation range up to 60°.

As an EAS develops in the atmosphere, it dissipates most of its energy by exciting and ionizing the molecules of air along its path. Excited nitrogen molecules

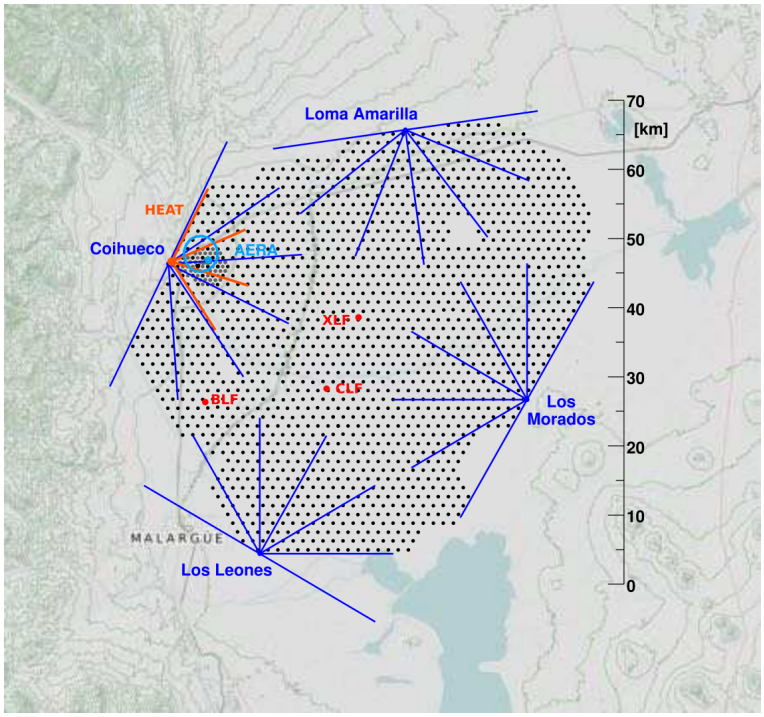

Figure 1.8: Map of the Pierre Auger Observatory. Four FD stations and the SD array are depicted. Blue and orange lines correspond to the field of view of the horizontally looking FD telescopes and HEAT, respectively. Black points depict the positions of individual SD stations. Picture is adopted from Ref. [21].

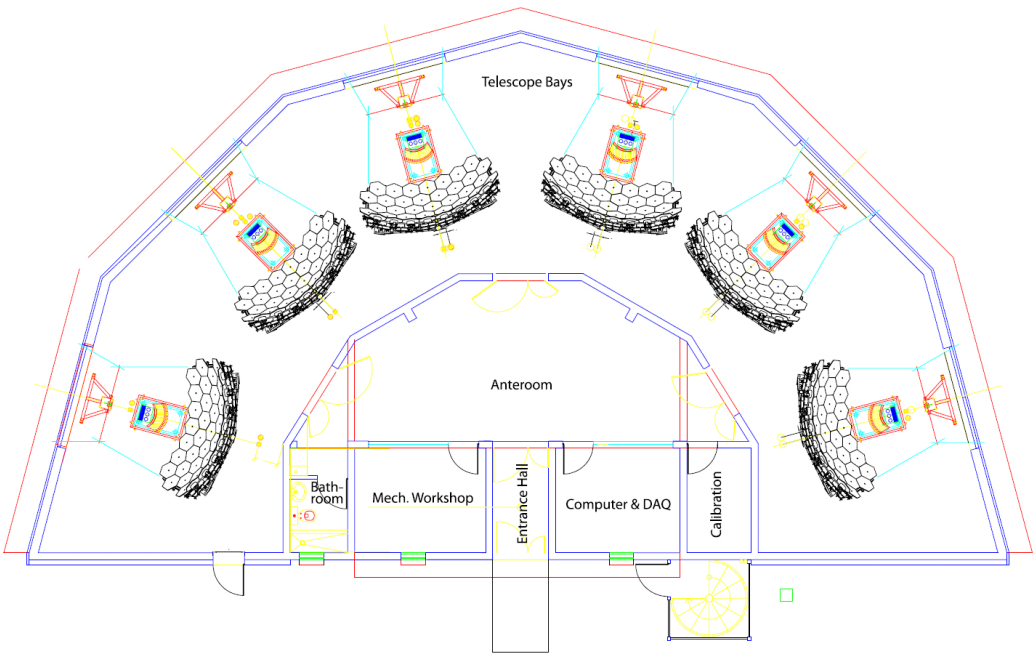

Figure 1.9: Scheme of the FD station. Positions of six FD telescopes are shown. Picture is taken from Ref. [22].

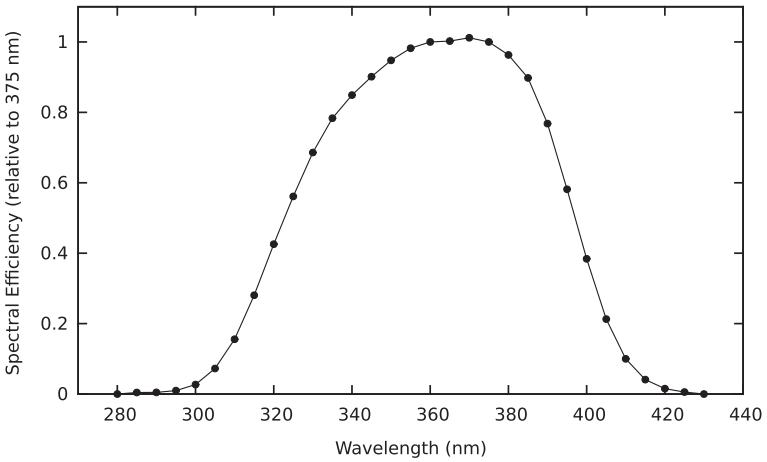

Figure 1.10: Relative spectral efficiency between 280 nm and 430 nm measured for telescope No. 3 at Coihueco site. The curve is taken relative to the efficiency of the telescope at 375 nm. Picture is taken from Ref. [2].

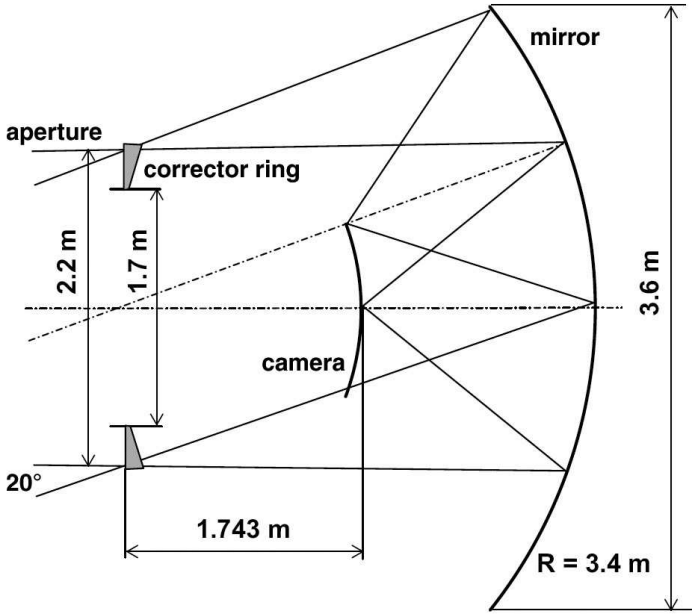

Figure 1.11: Geometrical parameters of the FD telescopes. Picture comes from Ref. [22].

fluoresce. They produce near ultraviolet radiation with approximately 80% of the light emitted between 300 nm and 450 nm [1]. This is reflected in the design of the FD telescopes, particularly in the throughput band of the UV filters which are installed in their apertures. The relative spectral efficiency of the FD telescope is shown in Fig. 1.10.

In the focal point of every telescope a camera is placed. Each camera consists of 440 hexagonal phototubes. Each phototube pixel fills the viewing angle of about $1.5° \times 1.5°$. The geometrical configuration of the FD telescope is shown in Fig. 1.11. More details about the FD can be found in Refs. [2, 22].

The fluorescence light is emitted isotropically with an intensity proportional to

the number of charged particles in the shower. The proportionality is given by the fluorescence yield. This quantity is precisely measured [23, 24]. In addition to the fluorescence light, showers produce a large number of Cherenkov photons. The Cherenkov emission angle in the atmosphere is about 1° with respect to particle trajectory, but slightly varying with altitude [1]. Nevertheless, an angular image of an EAS spreads to the angles of a few tens of degrees from the shower axis due to the scattering of particles in air. Details about the light emission from EASs are given in Sections 2.2.

The measurement of the fluorescence and Cherenkov light allows to determine the longitudinal profile of the shower, especially the atmospheric depth of the shower maximum $X_{\max}$. The energy and direction of incoming primary particle can be extracted as well. Several techniques used to reconstruct EASs from the FD data are summarized in Chapter 2.

1.3.2 Surface detector array

The SD array of the Pierre Auger Observatory was primarily designed to consist of individual water–Cherenkov stations whose cover is called a tank. The SD stations work in coincidence to allow the detection of EASs with footprint dimensions ranging from kilometers to tens of kilometers. The footprint area depends strongly on the energy of a primary particle and on the zenith angle of its incoming direction.

A scheme of the SD station is depicted in Fig. 1.12. Tanks have cylindrical shape. They are filled by 12 m^3 of pure demineralized water. The Cherenkov radiation is produced when charged particles with velocities higher than the speed of light in water travel through the volume of the tank. Emitted light is reflected by the Tyvek liner to the three photomultipliers. Digitalized data are transmitted through communication antennas to the central data acquisition system. Energy needed for the operation of stations is taken from batteries charged by solar panels.

The SD array consists of 1660 stations and covers an area about 3000 km^2. Stations are formed into a regular triangular grid with a spacing of 1500 m. The spacing is chosen according to the aim of measuring the EASs initiated by UHECRs [1]. Besides the regular array with the 1500 m spacing, the Infill array with the spacing of 750 m is located near the Coihueco site. It is designed to measure EASs of lower energies together with HEAT and Coihueco FD telescopes.

In addition, currently ongoing upgrade of the Observatory [21, 25] with scintillator detectors placed on top of the SD stations should help to distinguish between the EM and muonic signals detected by both water–Cherenkov and scintillator parts of the station. This way, useful information about primary mass will be collected. The AugerPrime upgrade is planned to be fully operational in 2025.

From the SD array measurement, the energy of an incoming primary particle and its arrival direction can be estimated through the energy of the EAS and the direction of the shower axis. The SD reconstruction methods are summarized in Sections 2.8 and 2.9.

The energy spectrum measured by the Infill array (spacing 750 m) is the essential result of the Pierre Auger Observatory with which the spectrum from

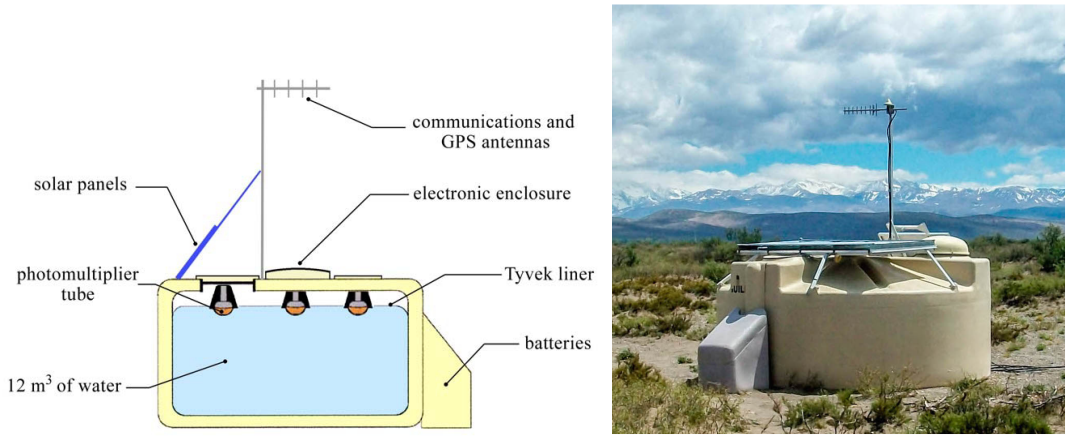

Figure 1.12: Water–Cherenkov station used at the Pierre Auger Observatory. Sketch of station before the AugerPrime upgrade and an image of the station with mounted scintillator are shown in the left and the right panel, respectively. Photomultipliers take the Cherenkov radiation reflected by the Tyvek liner. Solar panels, communication antennas, and batteries are depicted. Pictures are taken from Refs. [26, 21].

Cherenkov–dominated FD data is compared in Chapter 3. A direct comparison is possible in the common energy range of $10^{17} - 10^{18}$ eV.

1.3.3 Additional methods

Besides the SD array and four FD stations described above, the Pierre Auger Observatory is equipped with several additional instruments.

The Auger Muons and Infill for the Ground Array (AMIGA) [27, 2] is the underground detector dedicated to the direct measurement of muonic content of EASs. Formally, the Infill of the SD array with 750 m spacing is a part of AMIGA extension although the buried scintillators measure independently of densely placed SD stations. Nevertheless, AMIGA scintillators are located in the Infill region. Currently, the Unitary Cell of 7 scintilator stations is operational and during the AugerPrime upgrade the rest of 61 SD stations of the 750 m array will be enhanced by the buried scintillators. These scintilator detectors are placed 2.3 m under ground to minimise the contamination from EM shower particles. The segmented structure of the detector allows to count individual muons. The layout of the AMIGA station is shown in Fig. 1.13.

Other experimental methods are tested at the Pierre Auger Observatory as well. The radio emission from EASs in MHz region and microwave emission in GHz region are studied. The Auger Engineering Radio Array (AERA) studies the MHz emission from air showers and the Air–shower Microwave Bremsstrahlung Experimental Radiometer (AMBER), the Extensive Air Shower Identification using Electron Radiometer (EASIER) and the Microwave Detection of Air Showers (MIDAS) experiments study the microwave emission. For details about the radio and microwave detection see Refs. [28] and [29], respectively.

An important part of the AugerPrime upgrade [21] is related to the radio detection. Radio antennas will be placed on top of SD stations. This detection

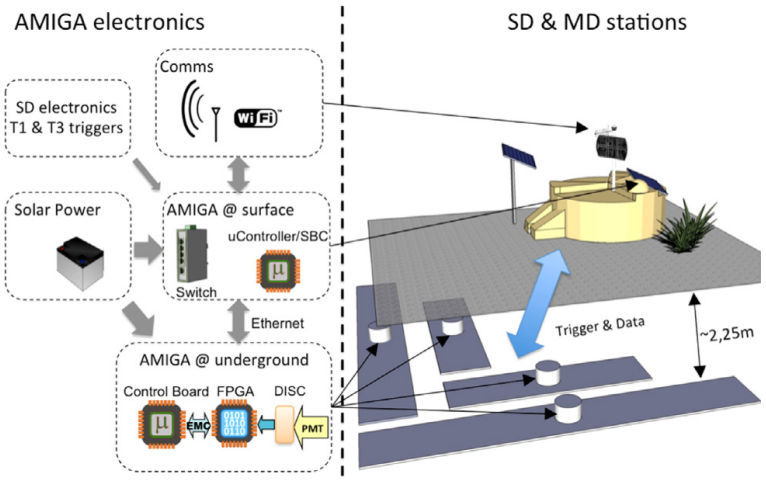

Figure 1.13: AMIGA station consisting of the SD station and buried muon detector. Picture is taken from Ref. [2].

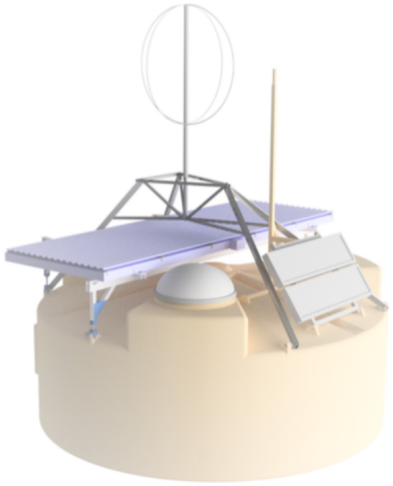

Figure 1.14: Sketch of the radio antenna mounted atop of the SD station. Picture is adopted from Ref. [25].

method is designed to measure the radio emission from the EM component of highly inclined showers that have a sufficient radio footprint on the ground to trigger several stations spanned 1500 m apart from each other. It will provide integral information about longitudinal profiles of inclined showers. Thus, the radio detection is complementary to the scintillator measurements of vertical events. Depiction of the radio antenna mounted atop of the SD station is shown in Fig. 1.14.

2. Reconstruction techniques

This Chapter summarizes methods that are used for the reconstruction of parameters of EASs which enable us to derive characteristics of primary particles causing these showers. Techniques that are currently established at the Pierre Auger Observatory are introduced. Their applications to the energy spectrum measurement are shown in Section 2.10. To this end, preceding studies of the Author [A1, A2, A3, A9, A10, A11, A12, A13, A14] are used.

The majority of the Chapter is dedicated to the reconstructions done using the FD data. Details about the light production from EASs and the trigger sequence of the FD are given in Section 2.2 and 2.3, respectively. The most basic type of the geometry reconstruction, the monocular time fit, is described in Section 2.4. The hybrid reconstruction that utilizes both the SD and the FD equipment is shortly mentioned in Section 2.5.

In Section 2.6, the multiple–eye reconstruction is introduced. It uses FD telescopes at more than one FD sites. The reconstruction was modified by the Author to allow for the measurement of shower velocities [A4, A5, A6]. In addition, the precision of the multiple–eye reconstruction was studied in other works done by the Author [A1, A2, A3].

The profile constrained geometry fit (PCGF), introduced in Section 2.7, is used in the analysis of the energy spectrum derived from Cherenkov–dominated events presented in Chapter 3. The implementation of the PCGF method is the Author's most important contribution to the reconstruction techniques. The code is implemented in the Auger $\overline{\text{Off}}\underline{\text{line}}$ software [30] described in Section 2.1. The implementation itself is presented in Appendix E.

For completeness, the reconstructions of EASs that utilize exclusively SD stations are sketched in Sections 2.8 and 2.9.

The calibration procedure of the SD measurements and a comparison of different estimates of the energy spectrum done at the Pierre Auger Observatory are given in Section 2.10. It is based on the results presented at the ICRC 2019 conference [31]. The contribution that describes the Cherenkov spectrum measurement was written by the Author for the Pierre Auger Collaboration [A14].

2.1 Auger $\overline{\text{Off}}\underline{\text{line}}$ reconstruction software

At the Pierre Auger Observatory, two reconstruction frameworks are used. They are the *Herald*, that is capable to deal with the SD events only, and the Auger $\overline{\text{Off}}\underline{\text{line}}$ [30], that is used to reconstruct both SD and FD data. Because the main focus of this thesis is on the FD events, only the $\overline{\text{Off}}\underline{\text{line}}$ software and reconstruction procedures implemented in it are described. Due to its modular architecture, the Auger $\overline{\text{Off}}\underline{\text{line}}$ is used for simulations of the detector response as well. It is equipped with modules that are able to read simulation outputs of various Monte Carlo software packages including the CORSIKA and the CONEX codes described in Section 1.2.1.

The $\overline{\text{Off}}\underline{\text{line}}$ framework consists of three principal parts

- A collection of processing modules that can be assembled and sequenced by instructions provided in `XML` files.

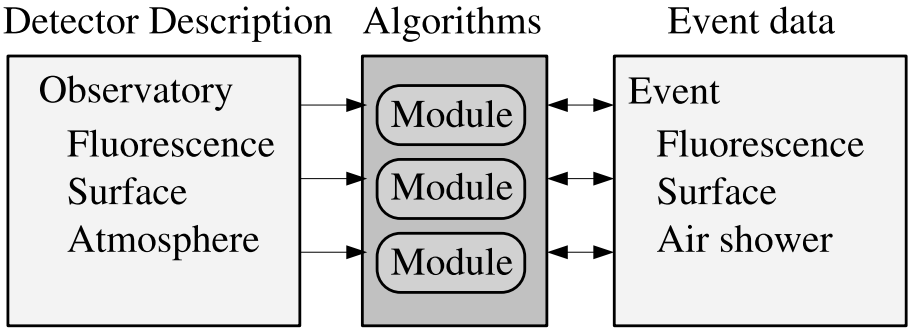

Figure 2.1: General structure of the Offline framework. Simulation and reconstruction tasks are broken down into modules. Each module is able to read information from the detector description and/or the event, process the information, and write the results back into the event. Picture is taken from Ref. [30].

- An event data model through which the modules can pass data from one to another and which accumulates all simulation and reconstruction information.

- A detector description that provides the data that describe the configuration and performance of the Observatory as well as the atmospheric conditions as a function of time.

Its schema is shown in Fig. 2.1.

Data reconstructed by the Auger Offline are stored in special ROOT data files [32], Advanced Data Summary Trees (ADST). The ADSTs contain all necessary information about reconstructed events, regardless they are measured or simulated. Data files can be read either by standard C++/ROOT programs with appropriate classes or by the EventBrowser program included in the Auger Offline which is a graphical tool for investigation of events. Most of figures that depict events in this Chapter are prepared with the EventBrowser software.

For more details about the Auger Offline see Ref. [30].

2.2 Light emission from extensive air showers

For the detection of EASs by the FD telescopes, a description of the light that they produce while they pass through the atmosphere is essential. Fluorescence telescopes are designed to measure the fluorescence light produced by nitrogen molecules, N_2, see Section 1.3.1. Moreover, a significant amount of Cherenkov radiation can be detected in the spectral region where the FD telescopes collect light, see Fig. 1.10. Due to the strong collimation of the Cherenkov beam this light is observed only for events with special geometries that point towards FD telescopes.

Besides the direct light, also the Mie and Rayleigh scattered, and eventually multiple–scattered, contributions to the light flux have to be taken into account. Details about the treatment of the scattered light in simulations and reconstructions of EAS events can be found in Refs. [2, 22, 33, 34, 35].

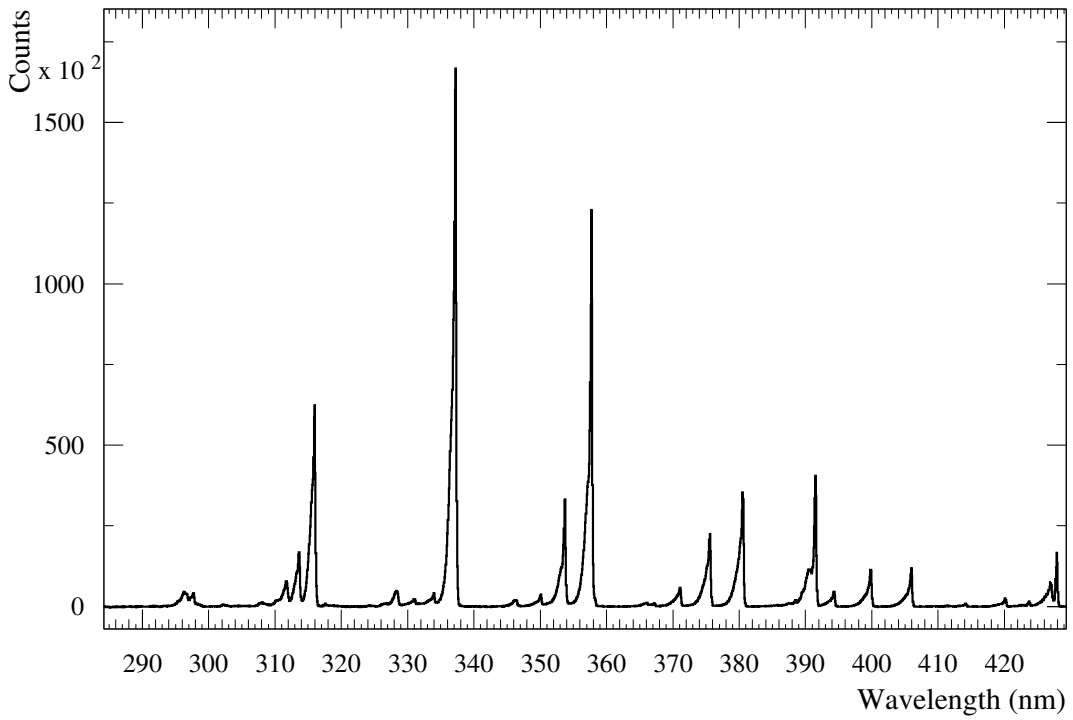

Figure 2.2: Relative intensities of N_2 fluorescence measured in dry air at 800 hPa and 293 K. Picture is taken from Ref. [23].

2.2.1 Fluorescence light

The fluorescence emission is the most important source of light in the FD telescopes for showers with energies above about 10^{17} eV. The proportionality between the amount of isotropically emitted photons and the energy deposit caused by EASs is given by the fluorescence yield. Several spectral lines are found in the N_2 emission spectrum, for their relative intensities see Fig. 2.2.

Because the light induced by EASs is of interest, the most precise estimates of the fluorescence yield are done with the use of an electron beam with an energy of several MeV. This configuration is chosen because it resembles the EM component of EASs. Such measurement has been performed by the AIRFLY experiment [23, 24]. Obtained results are used at the Pierre Auger Observatory in the $\overline{\text{Off}}\underline{\text{line}}$ modules responsible for the description of the light production in EASs.

The absolute scale of the emission, the absolute yield, is usually quantified with respect to the most intensive spectral line, i.e. the 337 nm band for the N_2 fluorescence, Y_{337}, see Fig. 2.2. Moreover, the absolute yield evolves with pressure as depicted in Fig. 2.3. According to the AIRFLY experiment, the fluorescence yield of the 337 nm band in air at 1013 hPa and 293 K has been found to be [24]

$$Y_{337} = 5.61 \pm 0.06_{\text{stat}} \pm 0.21_{\text{syst}} \text{ photons/MeV}. \tag{2.1}$$

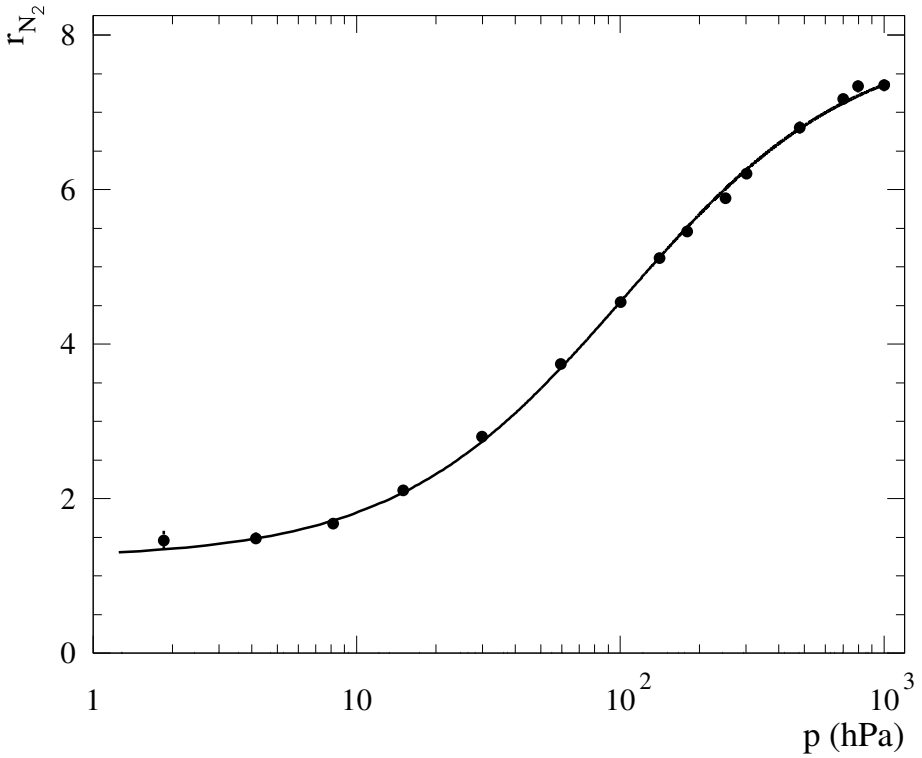

Figure 2.3: Evolution of the fluorescence yield with pressure. The ratio of the 337 nm band signal in pure N_2 atmosphere to the signal in dry air is shown. Picture is adopted from Ref. [23].

2.2.2 Cherenkov light

In contrast to the fluorescence emission, the Cherenkov light induced by EASs is produced anisotropically. Its emission angle, θ, with respect to the trajectory of individual particle is given by

$$\cos\theta = \frac{1}{n\beta}, \tag{2.2}$$

where n is the the refractive index of air and β denotes the velocity of the particle with respect to the speed of light in vacuum, c. The refractive index n depends on the pressure, temperature, humidity, and wavelength of emitted light. Under the conditions of the real atmosphere, the emission angle of a single particle is around 1°. Nevertheless, the Cherenkov emission from the whole EAS is much wider, as shown in Fig. 2.4. It is caused by scattering of individual particles inside EASs. The number of Cherenkov photons per track length that are produced by a charged particle of the total energy E and charge Z in a wavelength interval between λ_1 and λ_2 is given by

$$\frac{\mathrm{d}N_\gamma}{\mathrm{d}l} = 2\pi\alpha Z^2 \int_{\lambda_1}^{\lambda_2} \left(1 - \frac{1}{\beta^2 n^2}\right) \frac{\mathrm{d}\lambda}{\lambda^2}, \tag{2.3}$$

which means that the emission is continuous, unlike in the case of fluorescence radiation.

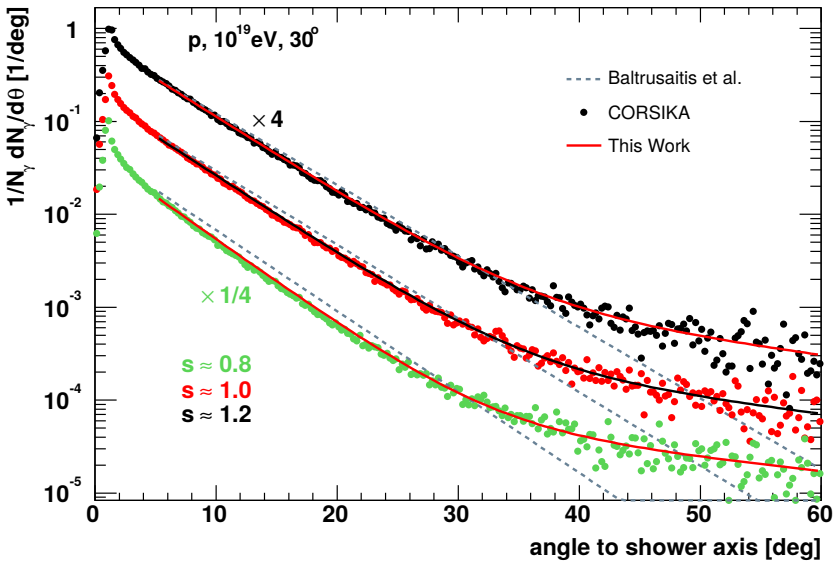

Figure 2.4: Angular distribution of produced Cherenkov photons with respect to the shower axis in a single CORSIKA shower for shower age $s = 0.8$, 1.0, and 1.2, see Eq. (2.6). The Monte Carlo results (points) are compared with predictions from Ref. [36] (solid lines) from which the picture is adopted.

The absolute amount of photons emitted by an EAS is proportional to the number of charged particles with energy above the Cherenkov threshold. This threshold in air roughly reads

$$E_{\rm thr} = \frac{mc^2}{\sqrt{2\,(n-1)}}, \tag{2.4}$$

where m is the mass of the particle emitting Cherenkov light. For electrons and positrons it reads about 21 MeV at the sea level. Muons have the threshold energy at the sea level of about 4.4 GeV and contribute to the total amount of light emission by less than 1%. The contribution from other particles is negligible.

In order to realistically estimate the Cherenkov emission from EASs, detailed Monte Carlo simulations are usually produced and their output is parametrized by the Cherenkov emission model. The contribution from electrons and positrons is essential. Actually, only the emission from electrons and positrons is assumed by up–to–date emission models and other contributions are completely neglected. Hence the main focus is on the parametrization of the electron energy spectra under the different conditions in EASs. This approach has been used in Refs. [36, 37] where more details about the Cherenkov light emission from EASs and its parametrization can be found. Results of these works are used in the modules of Offline to reproduce the Cherenkov light emission [30].

A correction to the parametrization given in Ref. [36] done by the Author is described in Appendix A. It is necessary to make the emission model to be in agreement with low energy CORSIKA simulations.

During the reconstruction process of EASs, a disentanglement between the fluorescence and Cherenkov light has to be done, see Section 2.4.1. To make

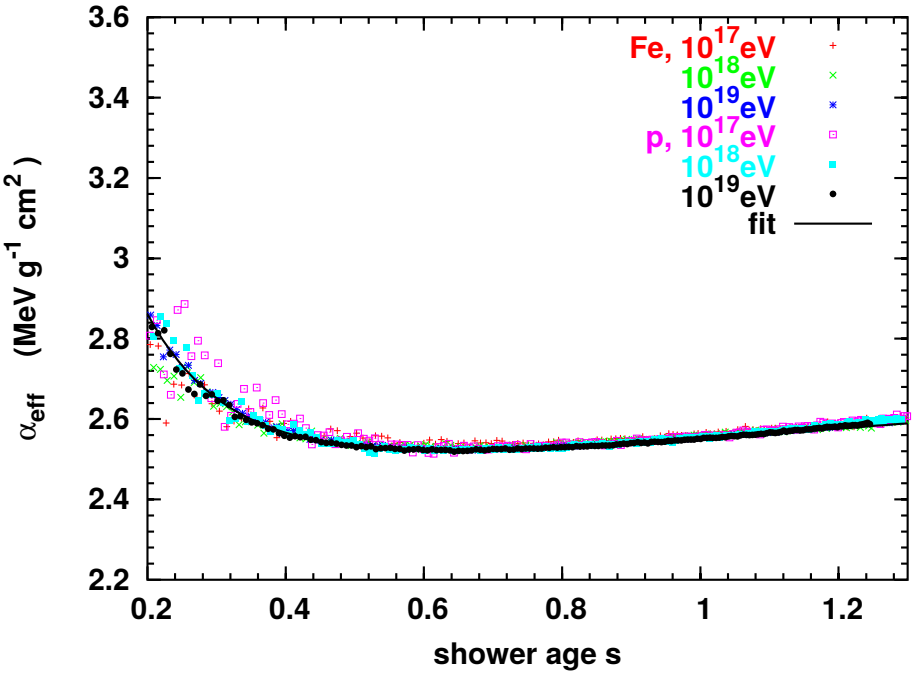

Figure 2.5: Average energy deposit per charged particle, i.e. the mean ionization loss rate, obtained from CORSIKA simulations of EASs. Universality for p and Fe primaries and three different incident energies is documented. Picture if taken from Ref. [36].

this possible, a relation between the energy deposit, $\frac{\mathrm{d}E}{\mathrm{d}X}$, and the number of charged particles, N_{ch}, that controls the fluorescence and Cherenkov emission, respectively, has to be known. Using simulations [36], the relation is given by

$$\alpha_{\mathrm{eff}}(X) = \frac{1}{N_{\mathrm{ch}}(X)} \left(\frac{\mathrm{d}E}{\mathrm{d}X}\right)(X), \tag{2.5}$$

where α_{eff} is the mean ionization loss rate and X stands for the slant depth defined in Eq. (1.2). The results of CORSIKA simulations are shown in Fig. 2.5. Obtained dependence is approximately universal for different primaries and primary energies. The dependence on the shower age, obtained by

$$s = \frac{3}{1 + 2X_{\mathrm{max}}/X}, \tag{2.6}$$

is not large and is tracked by the parametrization.

The Author contributed to this topic by pointing out the differences between the α_{eff} coefficient calculated with the use of CORSIKA and CONEX in Refs. [A9, A10]. As a consequence, the CONEX code was fixed to reasonably agree with more detailed CORSIKA simulations.

2.3 Triggers

In this Section, the trigger system of the FD is explained. The SD triggers independently of the FD operation[1)] and its trigger system is not important for

[1)] Except for the case in which the FD triggers and sends the T3 request to the SD treatment.

Table 2.1: Trigger sequence for FD events. At each telescope, events are selected based on channel thresholds (FLT), track shape (SLT), and lightning rejection (TLT). Events passing the TLT are merged by the EventBuilder on the FD EyePC. If the event passes further quality cuts for a simple reconstruction, a hybrid trigger (T3) is sent to the CDAS. Table is reproduced from Ref. [22].

FD Trigger Sequence			
Trigger Level	Location	Purpose	Event Rate
FLT	FE sub–racks (FLT boards)	pixel threshold trigger	100 Hz/pixel
SLT	FE sub-racks (SLT boards)	track shape identification	0.1-10 Hz/telescope
TLT	MirrorPCs (software)	lightning rejection	0.01 Hz/telescope
T3	EyePC (software)	EventBuilder, hybrid trigger	0.02 Hz/building

the Cherenkov spectrum analysis. Thus, the SD trigger system is not discussed. The detailed information can be found in Ref. [2].

The FD triggers are divided into four levels, namely the First Level Trigger (FLT), the Second Level Trigger (SLT), the Third Level Trigger (TLT), and the T3 trigger. Their characteristics are summarized in Tab. 2.1 where the location of their implementation, their purpose, and estimated event rates are shown. The FLT and SLT triggers are implemented directly on the boards of the FD electronics while the TLT and the T3 are PC software based. The latter two triggers are placed on the MirrorPC and the EyePC, respectively. The MirrorPCs collect events corresponding to individual FD telescopes placed in one FD building. The EyePC then merges the mirror events with the use of the EventBuilder program, store them, and check for the T3 trigger conditions. If the T3 trigger is matched, the EyePC sends[2)] the T3 request to the CDAS and consequently to the SD treatment.

The FLT works on individual FD pixels as a sliding boxcar sum of analog–to–digital converter (ADC) counts in 10 or 20 consecutive time bins in the case of main–building FD telescopes and HEAT, respectively. The difference between HEAT and other FD telescopes is caused by different electronics used by HEAT that has finer time binning of 50 ns instead of 100 ns for the rest of FD telescopes. If the FLT boxcar sum is larger than some threshold, the FLT pixel trigger is produced. The threshold is adjusted dynamically during the data acquisition to produce a stable 100 Hz trigger rate for each individual FD pixel. This is needed because the night sky background changes during the FD measurements.

The SLT is designed to search for spacial patters of FLT triggered pixels that match the appearance of an EAS on the FD camera. The fundamental types of patterns are shown in Fig. 2.6. The SLT algorithm demands at least four FLT triggered pixels out of the five (black) shown in Fig. 2.6. The complete set of 108 patterns arise from rotations of the fundamental patterns on a hexagonal grid of the FD camera.

[2)] Unless the delay veto or rate limitation veto prevents it to do so.

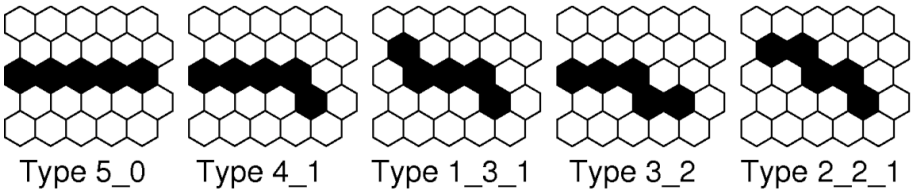

Figure 2.6: Fundamental types of SLT patterns regarded as straight track segments. Picture if adopted from Ref. [22].

The TLT is a software algorithm designed to divide the noise events that survive the low–level hardware triggers from the air shower data. It is optimized for the fast rejection of triggers caused by lightning, direct muon impacts on the camera, and randomly triggered FD pixels. The TLT rejects about 94% of all background events and only 0.7% of true showers. The documentation of the TLT trigger is present in Refs. [38, 22].

The T3 algorithm calculates a preliminary shower direction and a ground impact time with the use of a simple online reconstruction based on the monocular time fit, see Section 2.4. The T3 trigger is produced if, besides the spatial pattern checked by the SLT, also the time pattern resembles an EAS. Consecutively, the T3 request is sent to the SD and a part of the SD array that is close to the estimated shower core position is read out around the estimated ground impact time. This behaviour enhance the hybrid capability of the Pierre Auger Observatory.

For the analysis of Cherenkov–dominated data, a classification of events done by the TLT and the T3 triggers is essential, because it determines if a particular event is stored or thrown away. All events classified by the T3 algorithm as Shower Candidate, Close Shower, or Horizontal Shower are stored in the so called run data stream. Those that are T3 rejected, i.e. classified as Muon+Noise, Muon, Long Muon, Noise, Rejected by Burst Filter, Rejected by Rate Filter, and Large Event are subject to the further random rejection. Ten percent[3)] of these events are passed to the minimum bias data stream and stored. Only HEAT minimum bias data are used in the Cherenkov–dominated data analysis. Because the temporal characteristics of the Cherenkov–dominated events, especially at low energies, often cause the T3 rejection of the event[4)], an inclusion of the minimum bias stream substantially increases the statistics of the data and helps to decrease systematic uncertainties. Although 1% of the TLT rejected data are also stored in the minimum bias stream, only the TLT accepted data classified as Shower Candidate are used in the analysis.

All the trigger machinery that is described above is one–to–one implemented in the Auger Offline software, in modules responsible for the FD triggers. Even parts of the code that runs on the EyePC are identical to those called by the Offline modules. Because the software triggers have adjustable parameters, it is necessary to exactly track in Monte Carlo the settings used for each kind

[3)] 10% and 1% of the T3 rejected data are stored in HEAT and the rest of FD telescopes, respectively. The fraction of stored events also changed during the operation of the Observatory.

[4)] Actually, the T3 algorithm was developed also to reduce the number of Cherenkov–dominated events in the data stream to not overwhelm the SD with T3 requests. Hence, this behaviour is intentional.

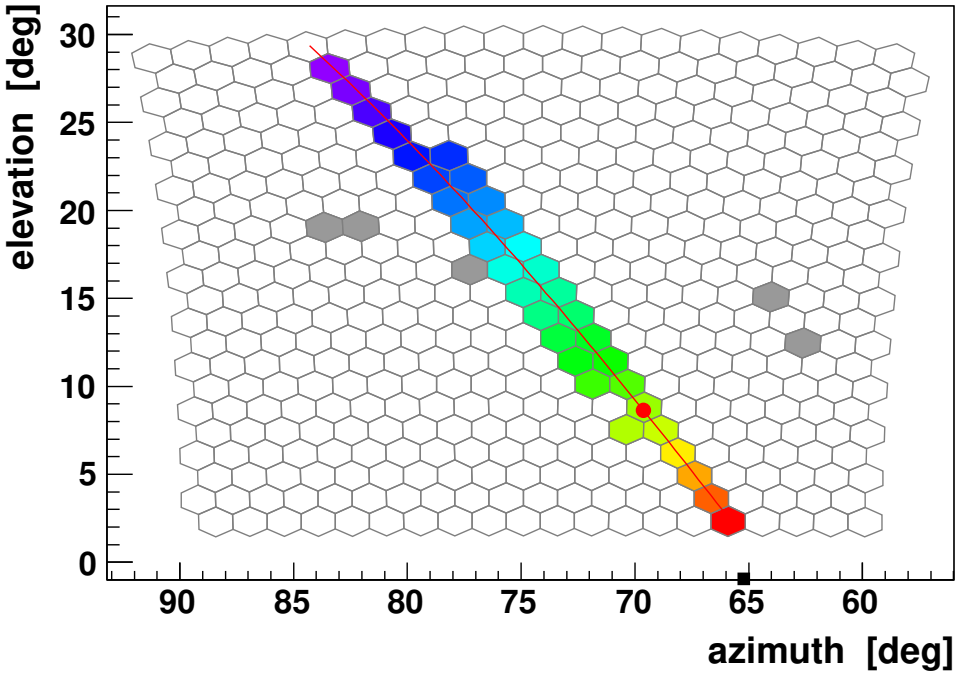

Figure 2.7: Signal on the FD camera of event No. 200827505541 registered by Coihueco telescope No. 3. The red line shows the reconstructed SDP, i.e. the projection of the shower axis into the camera plane. Colours correspond to the trigger time of the pixels – a sequence from former to latter times of detection is visualized by colors from magenta to red. Grey pixels are those that are randomly triggered.

of FD telescopes during the data acquisition. It is another contribution of the Author, who implemented in Offline the right switching between parameters used by HEAT and the rest of FD telescopes during different periods of data taking.

2.4 Monocular time fit reconstruction

When a signal from an EAS is detected in the FD, several techniques can be used to reconstruct the EAS in order to extract parameters of the primary particle that initiated it. Usually, the reconstruction starts by the determination of the shower axis. The most basic technique of the axis estimation is a monocular time fit.

The majority of the light coming from EASs is produced close to the shower axis. Thus, the axis is visible as a line of triggered pixels in the FD camera, as shown in Fig. 2.7.

The first step of the monocular reconstruction is the determination of a shower–detector plane (SDP). It is defined as the plane in which the shower axis and the fluorescence telescope lay, see Fig. 2.8. This plane is the same for all telescopes placed in the same building as they share the same position. This is also a limitation of the method, since it can be used only for events recorded by telescopes placed at only one location. The SDP is estimated by the fit pro-

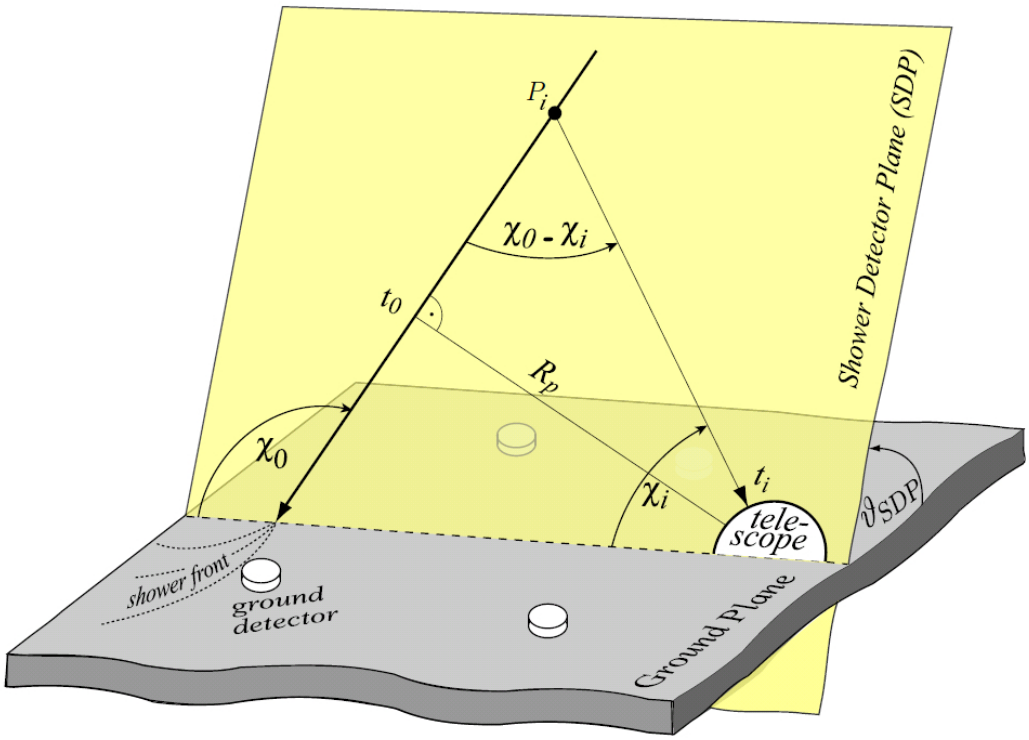

Figure 2.8: Geometry of the shower axis. Different quantities used in the reconstruction procedure are visualized (see text). In the following, the angle $\psi = \pi - \chi_0$ is defined as a complement to the angle χ_0. The light emmited at the point P_i reaches the FD telescope at the time t_i. The reference time t_0 corresponds to the light emission time at the closest point of the shower axis to the FD telescope.

cedure that uses the pointing directions of each phototube together with the time–integrated signal in the pixels. The tigger times are not used yet. The SDP fit minimizes the sum of residuals between the SDP and the pointing directions of phototubes with respect to $\vartheta_{\rm SDP}$ and $\varphi_{\rm SDP}$, where $\vartheta_{\rm SDP}$ is the zenith angle and $\varphi_{\rm SDP}$ denotes the azimuth angle of the SDP normal vector, respectively. The angle $\vartheta_{\rm SDP}$ also assigns the angle between the ground plane and the SDP, see Fig. 2.8.

Once the SDP is determined, the time information from phototubes is used to infer the geometry of the shower axis inside the SDP. The parameters that define the geometry are given in Figs. 2.8 and 2.9. The angle χ_i points in the SDP to the $i-$th phototube. The angle ψ, or equivalently χ_0, assigns the angle of the shower axis in the SDP.

To determine the geometry of the shower axis, a timing relation given in Eq. (2.10) is employed. Assuming the fluorescence light to be emitted by a point–like object moving at the light velocity (c) along the shower axis, the shower propagation time $\tau_{{\rm s},i}$ from the point P_i to the point at reference time t_0 on the shower axis is

$$\tau_{{\rm s},i} = \frac{R_{\rm p}}{c\tan(\chi_0 - \chi_i)}. \tag{2.7}$$

Here $R_{\rm p}$ is a perpendicular distance from the shower axis to the FD telescope

and χ_0, in accordance with the previous definition, is the angle between the horizontal line in the SDP and the shower axis, see Fig. 2.8. Photons are assumed to propagate on straight lines with the light velocity (c), so the light propagation time $\tau_{\mathrm{l},i}$ from P_i to the FD telescope is

$$\tau_{\mathrm{l},i} = \frac{R_\mathrm{p}}{c\sin(\chi_0 - \chi_i)}. \tag{2.8}$$

Assuming the light emitted immediately at the point P_i, an expected arrival time to the FD camera is

$$\begin{aligned} t_i &= t_0 - \tau_{\mathrm{s},i} + \tau_{\mathrm{l},i} \\ &= t_0 + \frac{R_\mathrm{p}}{c}\left(\frac{1}{\sin(\chi_0 - \chi_i)} - \frac{1}{\tan(\chi_0 - \chi_i)}\right) \\ &= t_0 + \frac{R_\mathrm{p}}{c}\tan\left(\frac{\chi_0 - \chi_i}{2}\right). \end{aligned} \tag{2.9}$$

It follows that the timing relation is given by

$$t(\theta_i) = \frac{R_\mathrm{p}}{c}\tan\frac{\theta_i}{2} + t_0, \tag{2.10}$$

where t_0 is the time when the shower reaches the point on the shower axis closest to the FD (point A in Fig. 2.9) and $\theta_i = \chi_0 - \chi_i = \pi - \psi - \chi_i$. Eq. (2.10) holds only under the assumption that the shower velocity and the light propagation velocity coincides. This is, strictly speaking, not true, but the differences are so small that they can be neglected. In practice, the speed of light in vacuum (c) is used. This derivation and a more general discussion about the fluorescence light propagation, the time delays caused by fluorescence deexcitation, and about other effects can be found in Ref. [39]. In Appendix A, a correction to the timing relation needed in the case of Cherenkov light description is discussed. The correction is caused by finite dimensions of EASs. In the case of observing the fluorescence–dominated or far away showers, Eq. (2.10) is a perfect approximation.

Once the timing relation (Eq. (2.10)) is derived, a proper fit of the data to this equation is performed. This is done by minimizing the time residuals with respect to the R_p distance, the shower axis angle ψ, and the time t_0. For each set of the parameters (R_p, ψ, and t_0), expected arrival times of photons to the FD camera, $t_{\mathrm{exp},i}$, are calculated. They are compared with the measured times in the sum of squared residuals

$$\rho^2_{\mathrm{FD}} = \sum_{i=1}^{n} \frac{(t_i - t_{\mathrm{exp},i})^2}{\sigma^2_{ti}}, \tag{2.11}$$

where $t_i (i = 1, 2, ..., n)$ are the time centroids of the detected pulses in phototubes, σ_{ti} are their uncertainties and n is the total number of firing phototubes.

After the time fit, the angles ϑ_{SDP} and φ_{SDP} as well as ψ inside the SDP are known. They are easily recalculated into the zenith angle ϑ and the azimuth angle φ of the shower axis.

The above described method is in principle sufficient for the reconstruction of the shower geometry. It was used for the geometry reconstruction at the Fly's

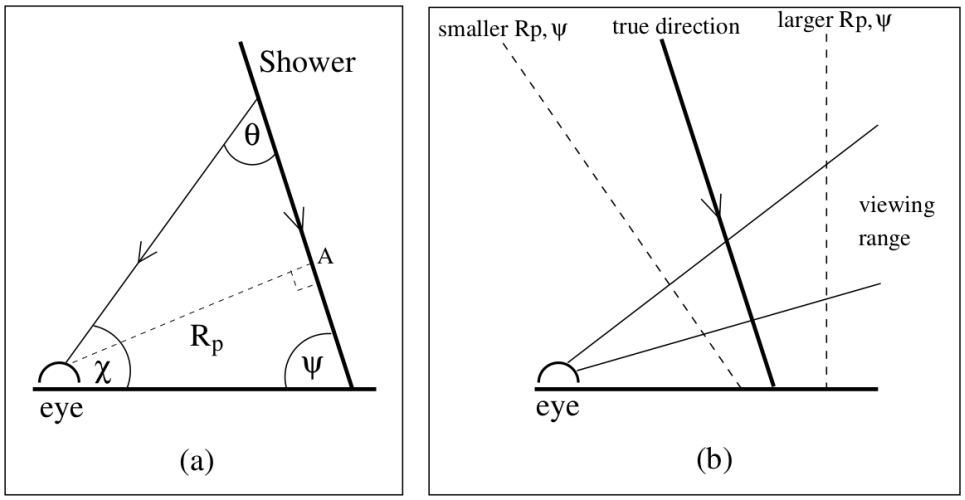

Figure 2.9: Monocular reconstruction (a) and an ambiguity of the axis in the SDP (b). Each of the three shower tracks at (b) would pass through the field of view of the detector with similar (and approximately uniform) angular velocity. Picture is taken from Ref. [1].

Eye and HiRes experiments [40]. Nevertheless, in comparison with the hybrid reconstruction or the multiple–eye reconstruction the monocular procedure is much less accurate, see Sections 2.5 and 2.6. This is caused by the fact that the timing relation given in Eq. (2.10) is fitted with respect to three parameters $R_{\rm p}$, ψ, and t_0. However, because the field of view of the FD telescope is limited, the range of the pointing angles θ_i available for the fit is also limited. If the time–angle track in the FD camera is too short, it can be accurately fitted by a line that corresponds to a uniform angular velocity. Consequently, an ambiguity in the determination of the shower axis parameters arises, see Fig. 2.9. In the case of an insufficiently short track, a strong correlation between the parameters is present which results in a very uncertain reconstruction of the EAS geometry, see Fig. 2.12. If no other information besides the one from a single FD station is present the profile constrained geometry fit (PCGF) described in Section 2.7 can be used to improve the precision of the shower reconstruction.

2.4.1 Energy and longitudinal profile

After the geometry of the EAS is accurately determined, the energy of the shower is estimated. In this section, we assume that the information from the FD measurement is available. The energy of the EAS is determined from its longitudinal profile. The shower profile is calculated by the Cherenkov–Fluorescence Matrix (CFM) method described in Ref. [33].

The CFM uses a system of linear equations to relate the light flux measured by the FD telescope, $\mathbf{y}$, and the energy deposited in the atmosphere by the EAS, $\mathbf{w}$. More precisely, the vector $\mathbf{y}$ represents the total number of photons detected in given time bins and the vector $\mathbf{w}$ is defined as the total energy deposited in

given slant depth bins, namely,

$$w_i = \int_{X_{i-1}}^{X_i} \frac{\mathrm{d}E}{\mathrm{d}X} \mathrm{d}X, \tag{2.12}$$

where X is the slant depth and i labels bins under consideration. With the use of Eq. (2.10), the arrival times of photons to the FD telescope and the slant depths of the emission points are easily related. The longitudinal profile reconstruction is based on the following equation

$$\mathbf{y} = \mathbf{C} \cdot \mathbf{w}, \tag{2.13}$$

where $\mathbf{C}$ is the CFM that contains all information about the light emission and propagation through the atmosphere as explained below.

Numbers of emitted fluorescence and Cherenkov photons in the slant depth bin ΔX_i, $N_\gamma^f(X_i)$ and $N_\gamma^C(X_i)$, respectively, are given by

$$N_\gamma^f(X_i) = Y_i^f w_i \Delta X_i, \tag{2.14}$$

$$N_\gamma^C(X_i) = Y_i^C N_i^e \Delta X_i, \tag{2.15}$$

where Y_i^f is the fluorescence yield discussed in Section 2.2.1, Y_i^C is an effective Cherenkov yield that takes into account the electron distributions within EASs, see Section 2.2.2, and N_i^e is the number of electrons and positrons at the slant depth X_i. More precisely, if the light is generated from a simulated EAS, some cutoff energy is usually applied. Hence the N_i^e corresponds to the number of particles above this cutoff. The Cherenkov yield then takes into account also the cutoff dependence of the electron energy distributions. To relate w_i and N_i^e, the mean ionization loss rate given by Eq. (2.5) is used. It also takes into account the cutoff dependence. The light flux detected by the FD telescope coming from the total number of generated fluorescence and Cherenkov photons, y_i^{fd} and y_i^{Cd}, respectively, is calculated according to

$$y_i^{fd} = \epsilon T_i \frac{A}{4\pi r_i^2} N_\gamma^f(X_i), \tag{2.16}$$

$$y_i^{Cd} = \epsilon T_i \frac{A}{4\pi r_i^2} f_C(\beta_i) N_\gamma^C(X_i), \tag{2.17}$$

where ϵ is a light detection efficiency of the FD telescope, A is its aperture, r_i is the distance from the telescope to the emission point, T_i is the atmospheric attenuation factor, and $f_C(\beta_i)$ is the fraction of Cherenkov photons per solid angle emitted at an angle β_i with respect to the shower axis, see Fig. 2.4. The equations above describe the direct fluorescence and Cherenkov light contributions. They are illustrated in the left panel in Fig. 2.10.

Moreover, the scattered Cherenkov light from the beam accumulated around the shower axis should be also taken into account as it can significantly contribute to the observed light flux. The number of Cherenkov photons in the beam is given by

$$N_\gamma^{beam}(X_i) = \sum_{j=0}^{i} \tau_{ji} N_\gamma^C(X_j), \tag{2.18}$$

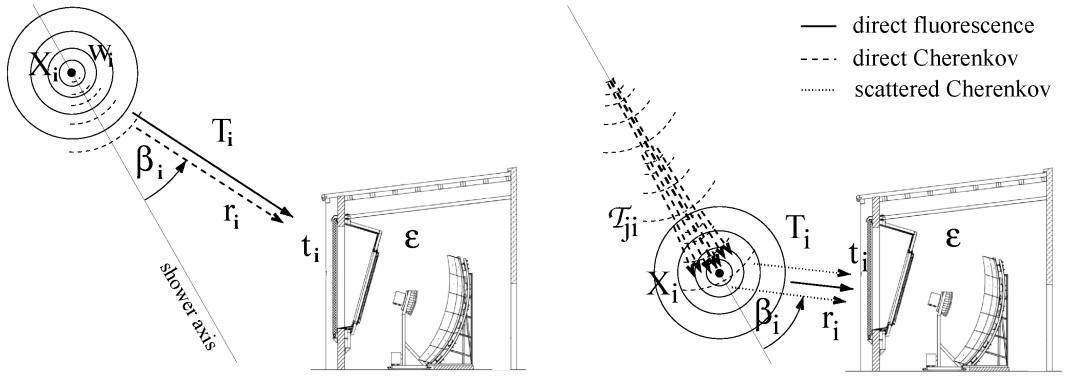

Figure 2.10: Illustrations of the light contributions to the CFM. Isotropic fluorescence emission (solid circles), Cherenkov beam along the shower axis (dashed arcs), and the direct (dashed lines) and scattered (dotted lines) Cherenkov light contributions are depicted. Also relevant quantities are shown schematically. Picture is taken from Ref. [33].

where τ_{ji} is the attenuation factor between slant depths X_j and X_i. Thus, the scattered Cherenkov contribution to the light flux at the observer position is

$$y_i^{Cs} = \epsilon T_i \frac{A}{4\pi r_i^2} f_s(\beta_i) N_\gamma^{beam}(X_i). \tag{2.19}$$

The fraction of the light beam that is scattered towards the detector is described by $f_s(\beta_i)$. It follows that the total light flux at the FD telescope is given by

$$y_i = y_i^f + y_i^{Cd} + y_i^{Cs}. \tag{2.20}$$

The matrix $\mathbf{C}$ (CFM) is composed of the coefficients in Eqs. (2.14–2.19) and it turns out to be lower triangular. The first estimate of the energy deposit profile is calculated with the use of the inversion of the matrix $\mathbf{C}$

$$\hat{\mathbf{w}} = \mathbf{C}^{-1}\mathbf{y}. \tag{2.21}$$

After that, the GH function given by Eq. (1.1) is fitted to the deposited energies represented by vector $\hat{\mathbf{w}}$. This defines the first estimate of the shower profile. In the following procedure, the parameters of the GH function are varied until the best match between the predicted and the measured light flux profiles is found. The fit is performed using the maximum likelihood method and all the details of the detector response are taken into account in a likelihood function.

The Author contributed also to this reconstruction procedure. He implemented the anti–aliasing filter response of the FD electronics to the likelihood function [A15] and he also improved technically the final fit to allow for finer binning of the CFM [A16]. These improvements are very important for the precise description of the short and time compressed light traces produced by Cherenkov–dominated events.

The calorimetric energy of the EAS is estimated by the integral of the GH function describing its longitudinal profile. The calorimetric energy, $E_{\rm cal}$, is ex-

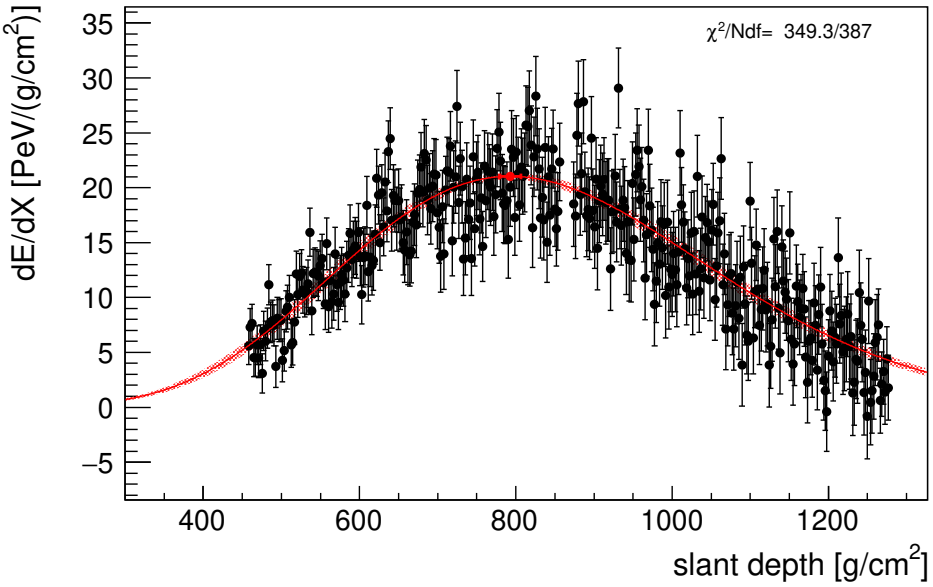

Figure 2.11: Longitudinal profile of event No. 171226109000. The energy deposited in the atmosphere is shown as a function of the slant depth. The event is dominated by the fluorescence light.

pressed in an analytical form as

$$E_{\mathrm{cal}} = \int_0^\infty \mathrm{GH}\left(X\right) \mathrm{d}X = \left(\frac{\mathrm{d}E}{\mathrm{d}X}\right)_{\mathrm{max}} \lambda \left(\frac{e}{\xi}\right)^{\xi} \Gamma\left(\xi + 1\right), \tag{2.22}$$

$$\xi = \frac{X_{\mathrm{max}} - X_0}{\lambda}, \tag{2.23}$$

where $\left(\frac{\mathrm{d}E}{\mathrm{d}X}\right)_{\mathrm{max}}$ is the value of the GH function (Eq. (1.1)) in the shower maximum and Γ stands for the Gamma function. The total energy of the EAS (E_{FD}) and consequently of the primary particle is given by E_{cal} corrected for the invisible energy (E_{inv}) carried away mainly by muons and neutrinos. The data driven corrections applied at the Pierre Auger Observatory at energies above 10^{17} eV are described in Ref. [41], their prolongation to lower energies is discussed in Section 3.1.

To determine accurately the longitudinal profile of the air shower, it is necessary to know the air density as a function of an altitude, the fluorescence yield, the concentration of aerosols and other parameters of the atmosphere. More information about aerosols is summarized in Ref. [42]. For the atmospheric conditions at the Pierre Auger Observatory see Ref. [43]. Monitoring of the atmosphere is done by the system of four lidar stations [44], cloud cameras [45], the data from GOES satellites [46], the GDAS database [47], and the central laser facility (CLF) [48].

The longitudinal profile reconstruction summarized in this Section is used, besides the monocular time fit, also after other types of shower axis estimations described in the following. An example of the longitudinal profile reconstructed with the use of the CFM matrix is shown in Fig. 2.11.

2.5 Hybrid reconstruction

The hybrid reconstruction of the shower axis is one of the key methods used at the Pierre Auger Observatory. It is based on adding information from the SD stations to the FD reconstruction time fit. In the beginning, it follows the procedure of the monocular time fit method described in Section 2.4. The SDP fit is performed and the timing relation written in Eq. (2.10) is adopted. Then, the two parts of residuals are stated

$$\rho^2 = \rho^2_{\mathrm{FD}} + \rho^2_{\mathrm{SD}}, \tag{2.24}$$

where ρ^2_{FD} stands for the fluorescence timing term and ρ^2_{SD} assigns the SD residuals. The form of the ρ^2_{FD} is the same as in the monocular time fit reconstruction, see Eq. (2.11). Following Ref. [1], the ρ^2_{SD} is given by

$$\rho^2_{\mathrm{SD}} = \frac{(t_i - t_{\mathrm{exp}})^2}{\sigma^2_{ti}}, \tag{2.25}$$

where the measured time t_i and expected time t_{exp} represent arrival times of particles to the i–th SD station with the largest particle count. The uncertainties of the measured times are

$$\sigma_{ti} = \frac{\sigma_{0i}}{\sqrt{n_i}}, \tag{2.26}$$

where σ_{0i} is a dispersion in the particle arrival times and n_i denotes the total number of particles detected in the SD station. The parameter t_{exp} is computed from a position of the station and a curvature of the shower front estimated from simulations. The geometry of the shower axis is obtained by minimizing the residual ρ^2 with respect to the axis–defining parameters.

The hybrid reconstruction of EASs is much more accurate in comparison with the monocular time fit reconstruction. It is caused by effectively larger time–angle track due to the incorporated SD signal. Because of that, the fit of Eq. (2.10) has no degeneration and all relevant parameters R_{p}, ψ, and t_0 can be accurately obtained, see Fig. 2.12. The hybrid reconstruction time fit of the detected event is shown in Fig. 2.13.

At the Pierre Auger Observatory, the hybrid reconstruction is the most used method for events detected by the FD. The possibility to measure in the hybrid regime is one of the biggest advantages of the Observatory. The only reconstruction technique that is in principle equally accurate is the multiple–eye reconstruction described in Section 2.6.

2.6 Multiple–eye reconstruction

Hitherto presented methods use information from the SD station and/or from the FD telescopes placed at only one location. Multiple–eye reconstruction is based on the fact that if telescopes at more than one FD station are used, the degeneration of the time fit described in Section 2.4 and illustrated in Fig. 2.9 no longer exists. One of the advantages of the multiple–eye reconstruction is that this method is, in principle, equally accurate as the hybrid reconstruction but it does not need any information from the SD array. Thus, the multiple–eye

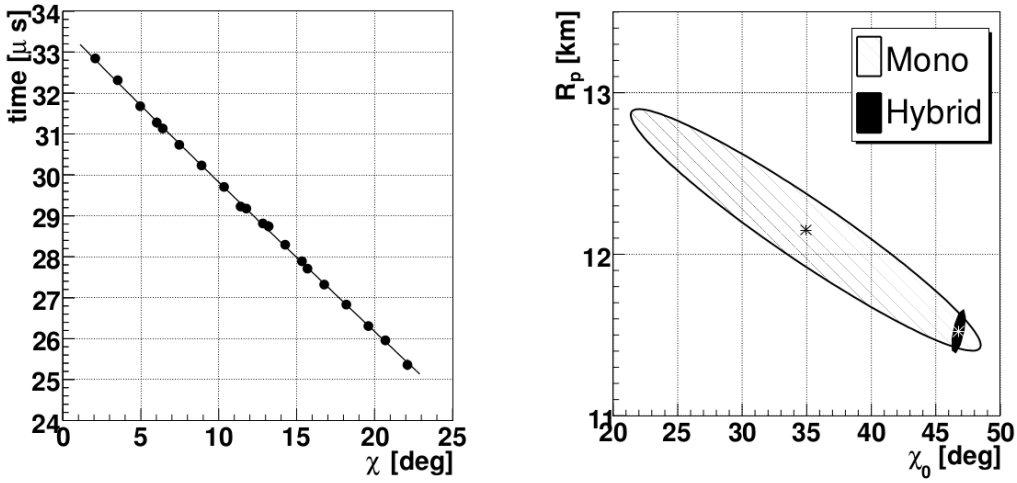

Figure 2.12: Time–angle track used in the monocular reconstruction of the air shower (left) and the improvement in the R_{p} and χ_0 determination in the case of the hybrid reconstruction (right). Ellipses correspond to the 68% confidence level regions. Picture is taken from Ref. [49].

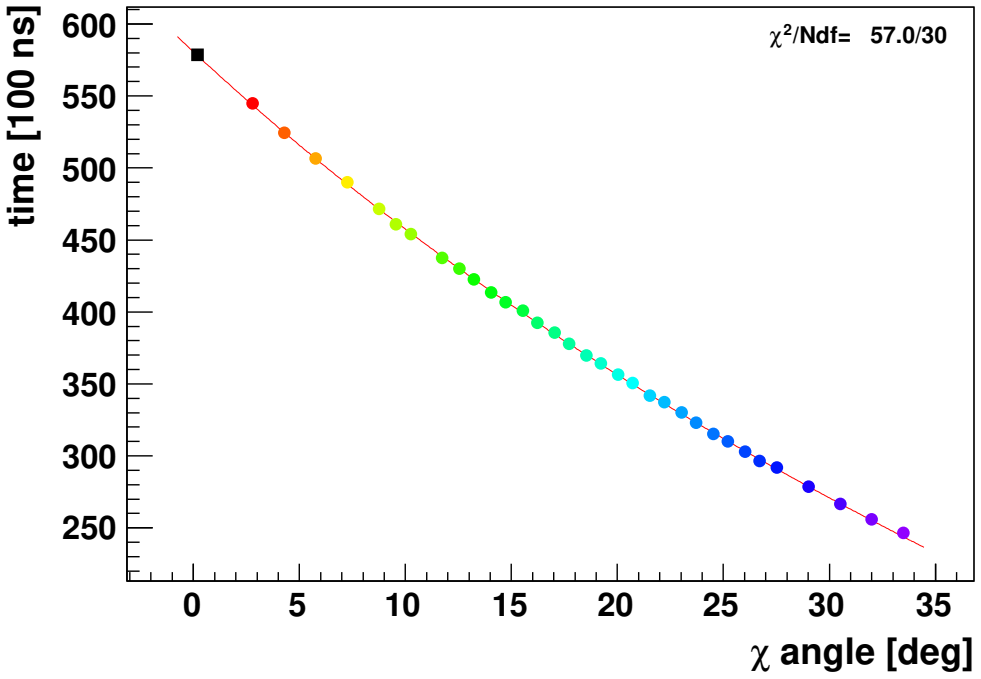

Figure 2.13: Hybrid reconstruction time fit of event No. 200827505541 registered at Coihueco site by telescope 3. The red line corresponds to the reconstructed shower axis. Colour dots represent values measured by the FD and the black dot comes from the SD station.

reconstruction is an independent test of the functionality of the whole detector. Moreover, events in which no SD information is present are analysed within the multiple–eye method. However, the suitable EASs have to be detected by at least

two FD stations.

In the future, the multiple–eye reconstruction could be used in projects where no SD array is possible to be build, e.g. in the space. There is also the Fluorescence detector Array of Single–pixel Telescopes (FAST) [50, 51] project that is designed as many telescopes with small number of wide–angle phototubes that will cover a large area. Although it is currently in the prototype phase placed at the Telescope Array [52] and the Pierre Auger Observatory, the FAST data will be eventually reconstructed in the multiple–eye mode.

Two types of the multiple–eye reconstruction exist, namely the multiple–eye SDP fit and the multiple–eye time fit methods. In practice, both techniques are usually performed simultaneously with appropriate weights.

The idea of the multiple SDP fit is sketched in Fig. 2.14. An intersection of the two or more shower–detector planes forms the shower axis. Practically, the fit is represented by a minimization of a sum of individual off–plane–angle residuals for all triggered pixels in all FD telescopes included in the multiple–eye SDP fit. The fit is performed with respect to the zenith angle ϑ, the azimuth angle φ, and an impact point of the shower axis. The impact point is the point where the shower axis intersects the ground level or selected horizontal plane. In this type of the reconstruction, no time information from phototubes is needed. On one hand, this is an advantage because potential time offset problems can be overcome this way. On the other hand, it is also a disadvantage because the measurement of the time is very accurate in comparison to the measurement of the pointing angle. The sum of off–plane–angle residuals is given by

$$\rho^2_{\mathrm{SDP}} = \sum_{i=1}^{n} \frac{\left(\frac{\pi}{2} - \Delta\phi_i\right)^2}{\sigma_i^2}, \tag{2.27}$$

where n is the number of firing phototubes in all involved FD telescopes, $\Delta\phi_i$ is the angle between the normal of the shower axis projection in the FD camera and the pointing direction of the phototube, and σ_i is the uncertainty of this angle. This uncertainty is estimated to be 0.35° at the Pierre Auger Observatory.

The multiple–eye time fit is based on the same procedure as the monocular time fit, see Section 2.4. The only difference is that the time information from all k included FD stations contribute to the total sum of time residuals

$$\rho^2_{\mathrm{FDtot}} = \sum_{i=1}^{k} \rho^2_{\mathrm{FD}i}, \tag{2.28}$$

where $\rho^2_{\mathrm{FD}i}$ belongs to $i-$th FD station and has the form given in Eq. (2.11). In the case that Eqs. (2.11) and (2.27) are used in the multiple–eye fit, the individual terms in the summations are, optionally, weighted by the total charge detected by the given phototube to reduce the dependence on the randomly triggered pixels.

An example of the real event reconstructed by the multiple–eye reconstruction is shown in Fig. 2.15.

The multiple–eye reconstruction was studied in detail by the Author in his previous works [A1, A2, A3] in order to estimate the directional precision of the reconstruction. The SDP type of the method was used by the Author in the search for events with anomalous velocity [A4, A5]. An accuracy of the velocity determination was tested on the laser shots from CLF [A6]. The latter study is

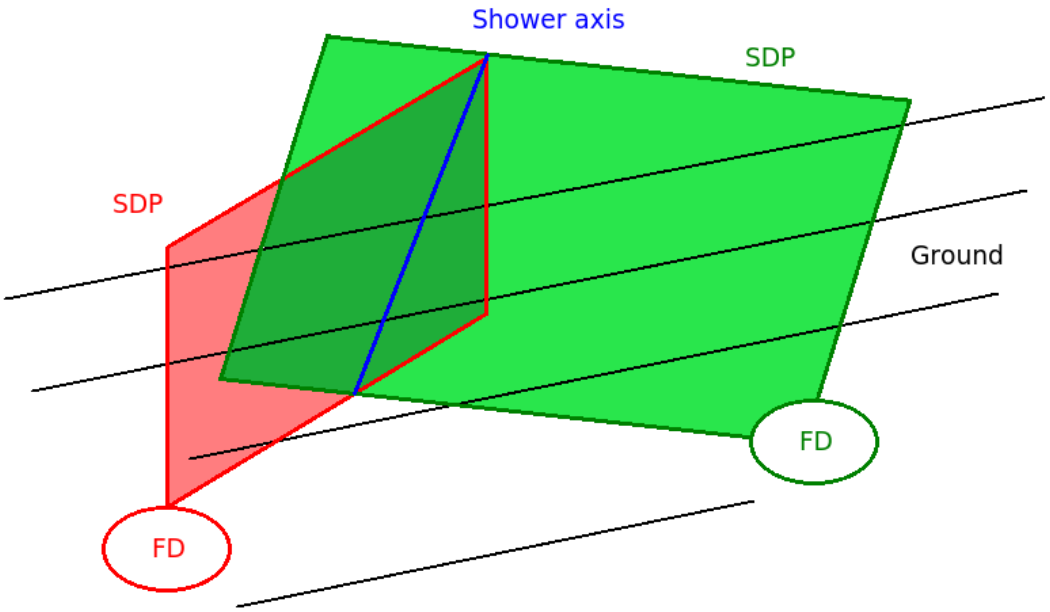

Figure 2.14: Schematic view of the stereo SDP reconstruction. Two SDPs intersect in the shower axis.

also a robust cross–check of the pointing of the FD telescopes and of the time synchronization of the FD telescopes at the Pierre Auger Observatory.

2.7 Profile constrained geometry fit

The PCGF is a method of the shower geometry reconstruction that works for a monocular view of an extensive air shower. It is favoured over the simple monocular time fit, described in Section 2.4, because the time fit suffers from correlations between shower axis parameters visualized in Fig. 2.12. Within the PCGF approach, the correlation is removed by an additional requirement on the energy deposit profile of the shower in the atmosphere. Specifically, the compatibility of the energy deposit profile calculated for a given geometry with the GH function (Eq. (1.1)) is required. The PCGF was invented at the HiRes experiment [53] for fluorescence–dominated events and is currently used by TALE [54] for Cherenkov–dominated data.

Technically, a scan in the angle χ_0 is performed. For each fixed value of χ_0 the two remaining parameters, R_p and t_0, are calculated by linear regression using Eq. (2.10). For the geometry fixed in this way, a fit of the GH function (Eq. (1.1)) to the energy deposit profile of the shower is done as follows. Four free parameters X_0, X_max, λ, and $\left(\frac{\mathrm{d}E}{\mathrm{d}X}\right)_\mathrm{max}$ are varied, and for each of the combinations, the light flux that would be measured in the FD telescopes is predicted and compared to the measured flux. This procedure is explained in more details in Section 2.4.1. To this end, the likelihood that is used to quantify the level of agreement between the particular χ_0–defined geometry and initial assumptions is composed of parts corresponding to the time fit Eq. (2.10), constraints on GH parameters, and the observed light flux in the FD telescopes. Finally, the most likely geometry is

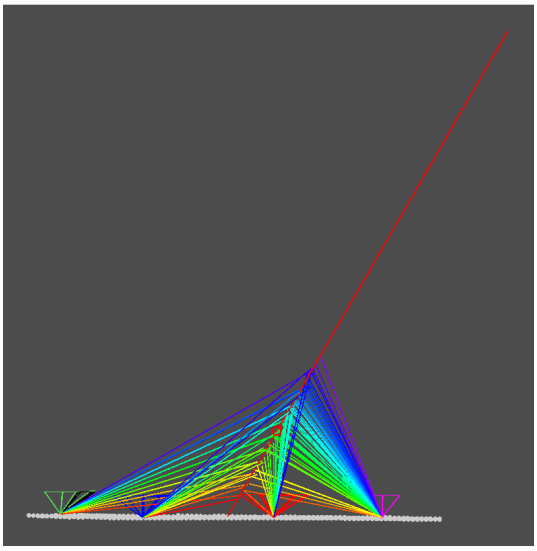

(a) Front view

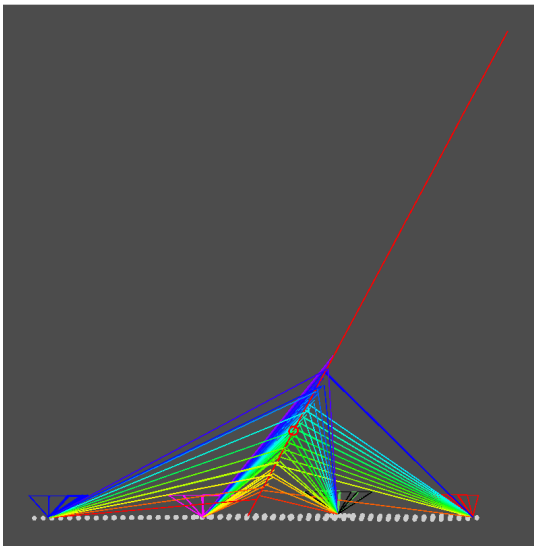

(b) Side view

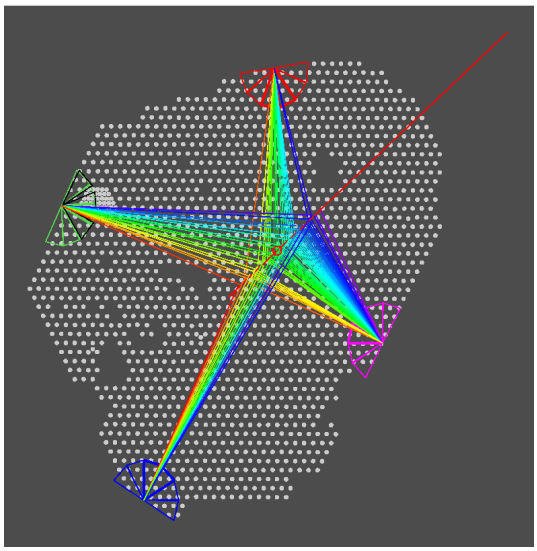

(c) Top view

Figure 2.15: Multiple–eye reconstruction of event No. 201001804541. Colour lines indicate the rays of fluorescence light with the time information matching the colours. The colour coding is the same as in Fig. 2.7. Three different views are presented.

selected. For this geometry, the resulting energy deposit profile is fine–tuned in the following reconstruction steps.

Besides the implementation of the basic method described above, the PCGF reconstruction module is able to deal with FD telescopes placed at different positions, see Appendix E. It allows us to use the HEAT together with the Coihueco building FD telescopes (Coihueco and HEAT buildings are placed about 170 m apart), effectively working in a partial stereo observation regime for showers seen by both detectors. An example of a shower detected simultaneously by HEAT and Coihueco FD telescopes which was reconstructed by the PCGF is shown in Fig. 2.16.

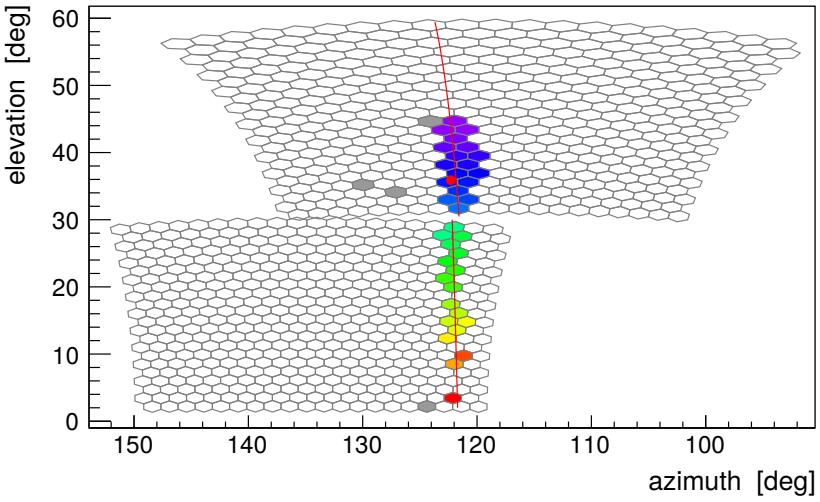

(a) Camera view

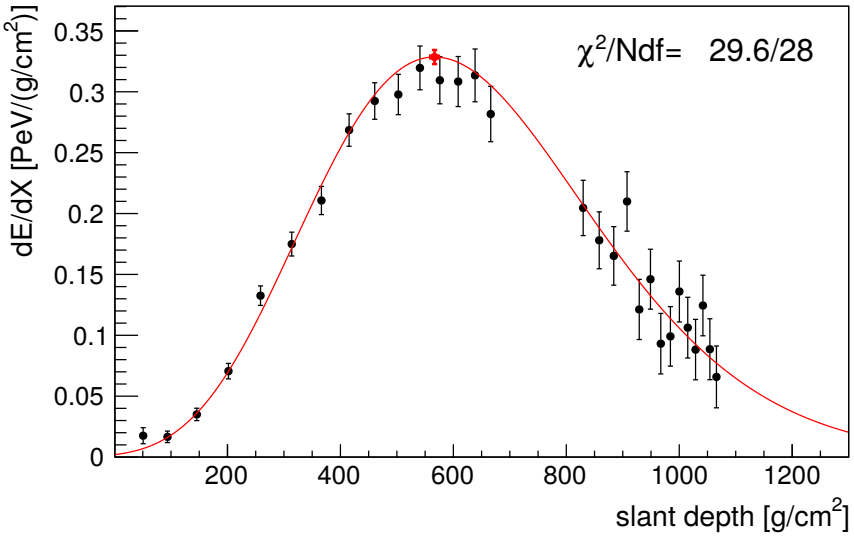

(b) Energy deposit profile

Figure 2.16: PCGF reconstruction of event No. 152295820800. The camera view (top panel) together with the reconstructed energy deposit profile of the shower in the atmosphere (bottom panel) are shown. The reconstructed calorimetric energy reads $E_{\mathrm{cal}} = 2.1 \times 10^{17}$ eV. The gap in the profile corresponds to the crossing between two FD telescopes. The event is dominated by the Cherenkov light, for the energy deposit profile that arises from the fluorescence dominated event see Fig. 2.11.

Although the PCGF works also in principle for fluorescence–dominated events, the main interest is focused on the Cherenkov–dominated data. The first reason is due to a better accuracy of the geometry reconstruction which is connected to the strong collimation of the Cherenkov beam produced by showers. This option improves the sensitivity of the reconstruction to small changes in the mutual telescope–shower axis position. The second reason is the fact that low energy showers are detectable thanks to the Cherenkov radiation, while fluorescence is mostly absent. Thus, the most important application of the PCGF is in the low–

energy part of the cosmic ray spectrum whereas the high–energy part is better analysed by hybrid measurements. Furthermore, the flux of cosmic rays at low energies is sufficient to fill the limited phase space of the Cherenkov–dominated events.

The PCGF is currently the only method that is used to derive the energy spectrum below 10^{17} eV from events detected by the FD. Based on other $\overline{\text{Off}}\underline{\text{line}}$ modules developed in the Pierre Auger Collaboration, the Author implemented the PCGF as a module into the Auger $\overline{\text{Off}}\underline{\text{line}}$ software [A11, A12, A14] described in Appendix E.

It is worth to mention that the low–energy spectrum of cosmic rays derived by the Author in Chapter 3 relies mostly on the use of the PCGF reconstruction.

2.8 SD vertical reconstruction

Besides the FD–based reconstructions described above, also independent SD reconstructions are used. Such methods are used if no FD signal is present. The SD reconstruction is necessary because the SD array works all the time while the FD measures only at moonless nights, i.e. only about 13% of the time of the SD operation. The duty cycle is the main advantage of the SD. On the other hand, the SD–based reconstructions of energies of EASs are less accurate than the estimates done with the use of the FD which, in contrast to the SD detection, allows to measure the longitudinal profiles of EASs as well.

Two types of the SD reconstruction are used, the SD vertical and the SD inclined methods. The SD vertical method differs from the SD inclined reconstruction, see Section 2.9, in the component of EASs that contributes the most to the detected signal in the SD stations. In the case of the SD vertical reconstruction, which is used for showers with zenith angles below 60°, the electromagnetic (EM) component dominates the signal. The SD inclined reconstruction is used for showers with zenith angles above 60° for which the muonic component of the EAS dominates at the ground level.

The SD vertical reconstruction is based on the processing of time information from triggered stations of the SD array combined with their total signals [2]. A first estimate of the arrival direction of the shower is obtained by fitting the start times of the signals, t_i, in individual SD stations to a plane shower front. The t_i times are defined by the time when the flash analog–to–digital converter (FADC) signal in the SD station exceeds the threshold of 4 VEM (vertical equivalent muon). For events with enough triggered stations, these times are described by a more detailed model that approximates the evolution of the shower front with a speed–of–light inflating sphere given as

$$c(t_i - t_0) = |\mathbf{x}_{\rm sh} - \mathbf{x}_{\rm i}|, \tag{2.29}$$

where $\mathbf{x}_{\rm i}$ are the positions of the SD stations on the ground, $\mathbf{x}_{\rm sh}$ is a virtual origin of the shower and t_0 is a virtual start time of the shower development. From this 4–parameter fit, the radius of curvature of the inflating sphere is determined. The impact point of the EAS on the ground, $\mathbf{x}_{\rm gr}$, is obtained from the lateral distribution function (LDF) fits of the signals in the SD stations [55].

The LDF fit is based on a maximum likelihood method that also takes into account the probabilities of the non–triggered stations and the saturated stations

close to the shower axis. In this procedure, the signal S in the station is considered as a function of a distance from the shower axis r. Traditionally, the modified Nishimura–Kamata–Greisen function is chosen [56]

$$S(r) = S(r_{\text{opt}}) \left(\frac{r}{r_{\text{opt}}} \right)^{\beta} \left(\frac{r + r_1}{r_{\text{opt}} + r_1} \right)^{\beta+\gamma}, \tag{2.30}$$

where r_{opt} is the optimal distance, $r_1 = 700$ m and $S(r_{\text{opt}})$ is an estimator of the shower size. The LDF depends on a zenith angle ϑ through the β parameter. Initial estimates of β and γ are given by

$$\beta_0 = 0.9 \sec \vartheta - 3.3, \tag{2.31}$$
$$\gamma_0 = 0, \tag{2.32}$$

and, in the fit procedure, their coefficients are adjusted.

The optimal distance $r_{\text{opt}} = 1000$ m and $r_{\text{opt}} = 450$ m for the SD arrays with 1500 m and 750 m spacing, respectively. The corresponding size estimators of the SD signals are $S(1000)$ and $S(450)$, respectively. To account for the attenuation of the shower in the atmosphere, the constant intensity cut (CIC) [57] method is used to recalculate the size estimator to the estimator of the shower energy. The attenuation curve $f_{\text{CIC}}(\vartheta)$ is fitted with a third degree polynomial [58]

$$f_{\text{CIC}}(\vartheta) = 1 + ax + bx^2 + cx^3, \tag{2.33}$$
$$x = \cos^2 \vartheta - \cos^2 \bar{\vartheta}, \tag{2.34}$$
$$S(r_{\text{opt}}) = S_{\bar{\vartheta}} f_{\text{CIC}}, \tag{2.35}$$

where the coefficients are calculated for events above a certain intensity threshold (number of events per steradian that defines the size thresholds with respect to the zenith angle) and differ for the 1500 m and 750 m arrays. The reference zenith angles are $\bar{\vartheta} = 38°$ (S_{38}) and $\bar{\vartheta} = 35°$ (S_{35}) for the regular and the Infill array, respectively. Details about the implementation of the CIC method at the Pierre Auger Observatory can be found in Ref. [58].

The results of the SD are usually presented above the energy threshold where the trigger efficiency is above 99% regardless the primary particle. This means that the exposure of the SD is calculated geometrically from the number of active hexagon cells of the SD stations and is energy independent. The very same holds also for the inclined type of the SD reconstruction.

2.9 SD inclined reconstruction

Events with incident zenith angle above 60° detected by the SD are subjects of the inclined reconstruction [59]. These events significantly differ from the vertical data because the electromagnetic (EM) part of the shower is almost completely attenuated in the atmosphere. Subsequently, the signal in the SD is dominated by positively and negatively charged muons. The EM contamination accounts for roughly 20% of the signal, but even this signal originates mostly from muons through their decay. Oppositely charged muons are deflected in the Earth's magnetic field in the opposite way. Because of that, the measured SD

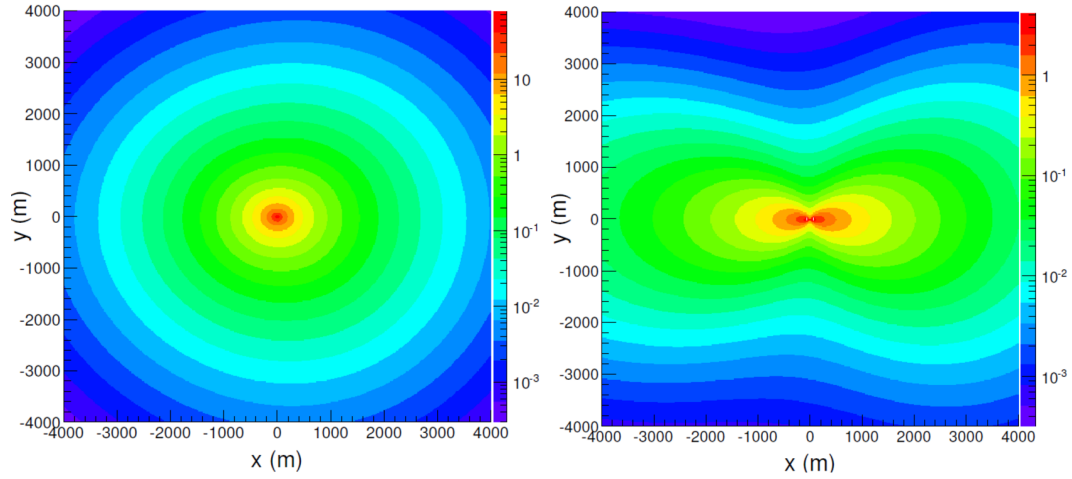

Figure 2.17: Contour plot of the muon density for the simulated proton shower with the energy of 10^{19} eV and zenith angle of 70° (left) and 84° (right). The azimuth angle was set to 0° and the y–axis is oriented in the projected direction of the Earth's magnetic induction field. Coordinates correspond to the perpendicular plane to the shower axis. Picture comes from Ref. [59].

pattern is asymmetric. This effect is taken into account in the reconstruction which is based on fitting maps of the muon distribution on the ground to the measured SD signals. An example of the asymmetric muon map is depicted in Fig. 2.17.

The resulting relation between the simulated distribution ρ_{sim} and measured signals ρ is

$$\rho(\mathbf{r}) = N_{19}\rho_{\text{sim}}(\mathbf{r}, \vartheta, \varphi), \tag{2.36}$$

where ϑ and φ are the zenith and azimuth angles of the shower axis, respectively. N_{19} is the normalization factor which is the energy estimator of the inclined analysis.

More details about the inclined reconstruction can be found in Ref. [59].

2.10 Energy calibration and spectrum

The energy scale of the Pierre Auger Observatory is fixed by the FD measurements.

In order to determine the energy of an EAS from the FD measurement, it is necessary to obtain a relation between ADC counts from individual phototubes of the FD cameras and the light flux and consequently the energy deposit in the atmosphere. For this purpose, three types of calibration take place at the Pierre Auger Observatory – the absolute calibration, the relative calibration, and the calibration that uses the laser shots to the atmosphere. The absolute calibration uses a portable source of homogeneous light flux which is mounted on the FD telescopes. This type of calibration has been performed several times for each telescope during the Pierre Auger Observatory operation. Before and after each night of data taking, series of relative calibration measurements are performed. They are used to monitor the detector response between absolute calibrations.

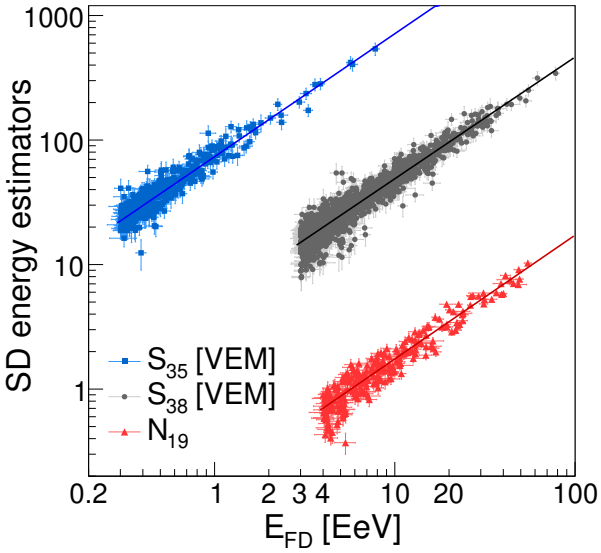

Figure 2.18: Energy calibration curves. Energy estimators of the SD 1500 m vertical (gray), the SD 1500 m inclined (red), and the SD 750 m vertical (blue) methods are shown. Units of S_{35} and S_{38} are vertical equivalent muons (VEM), N_{19} is dimensionless [2]. Figure is taken from Ref. [61].

The combined uncertainty of the absolute and relative calibrations is about 9.9% [60]. Calibration using laser shots is done from the central laser facility (CLF) station located in the centre of the SD array. To properly cover the field of view of all four FD sites, also the extended laser facility (XLF) is used the same way as the CLF. These facilities consist of a nitrogen laser with the wavelength of 370 nm that provides 100 mJ pulses into the atmosphere [48]. A scattered light from the laser is then measured by the FD telescopes. This procedure is performed during the whole measurement of the FD and allows to correct for varying optical depth of the atmosphere.

The energy calibration of the SD measurements is obtained using the FD. This method does not depend on simulations. The three energy estimators described in Sections 2.8 and 2.9 are calibrated to the hybrid measurements. This is done on the sub–set of Golden events, those events that are separately reconstructed by the hybrid and the corresponding SD reconstruction at the same time. The calibration function has the form of

$$E_{\mathrm{FD}} = A\Sigma^{B}, \tag{2.37}$$

where $\Sigma = S_{38}, N_{19}, S_{35}$, see Sections 2.8 and 2.9, while A and B denote the calibration constants. Calibration curves are shown in Fig. 2.18. The most recent calibration constants [58] are listed in Tab. 2.2.

The energy spectrum measurements are done at the Pierre Auger Observatory with the use of the above described reconstruction techniques including the calibration procedure. The latest energy spectra that were presented by the Collaboration at the ICRC 2019 conference [58] are shown in Fig. 2.19. The energy spectrum from Cherenkov–dominated data was prepared by the Author [A14]. The most recent low–energy spectrum is described and discussed in Chapter 3.

Table 2.2: Parameters of the SD energy calibration. The type of reconstruction is marked in the first column and Σ is corresponding energy estimator. Calibration constants A and B obtained with the help of Eq. (2.37) are given in two rightmost columns. S_{35} and S_{38} are expressed in vertical equivalent muons (VEM). Values come from Ref. [58].

reconstruction	Σ	A	B
SD 1500 m vertical	S_{38}	(0.186 ± 0.003) EeV	1.031 ± 0.004
SD 1500 m inclined	N_{19}	(5.51 ± 0.07) EeV	1.04 ± 0.02
SD 750 m vertical	S_{35}	$(1.32 \pm 0.04) \cdot 10^{-2}$ EeV	1.006 ± 0.009

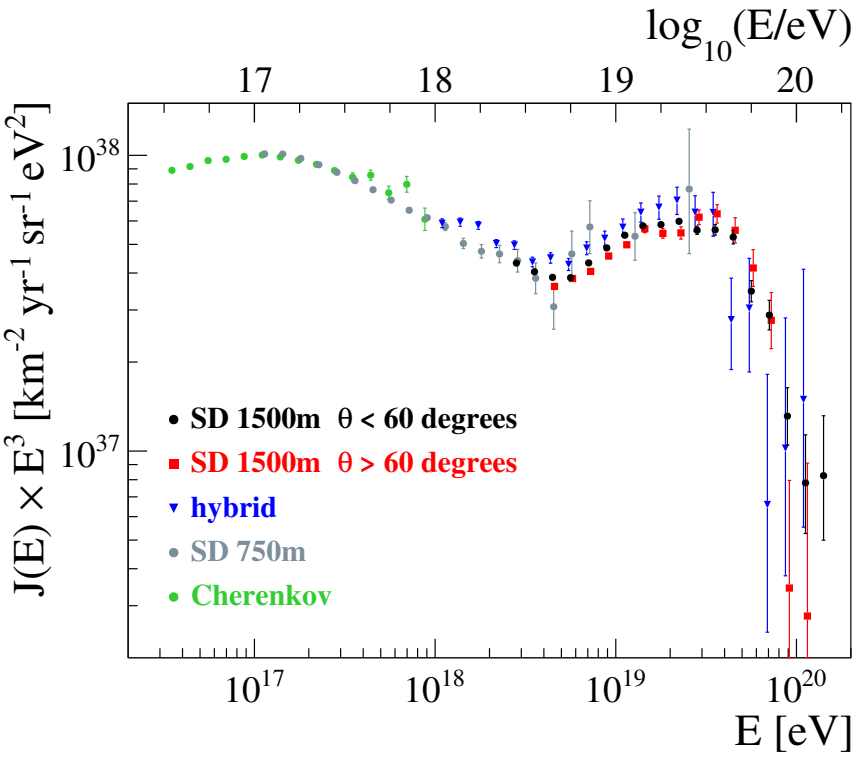

Figure 2.19: Energy spectra of cosmic rays presented by the Pierre Auger Collaboration at ICRC 2019. Cosmic ray flux multiplied by the third power of energy is shown as a function of energy. Picture is adopted from Ref. [58].

3. Energy spectrum from Cherenkov–dominated events

The main analysis of the Author deals with the determination of the energy spectrum of CRs from Cherenkov–dominated events. To this end, the PCGF method of the shower axis reconstruction described in Section 2.7 is used.

Necessary ingredients, the invisible energy model and Monte Carlo (MC) simulations of response of the Pierre Auger fluorescence detector (FD), are summarized in Sections 3.1 and Appendix B, respectively. The data sample is described in Section 3.2. In Section 3.3, details about the exposure calculation are given. Unfolding correction for to the detector response is estimated in Section 3.4. Systematic uncertainties are discussed in Section 3.5. Finally, a combination of all currently available measurements of the energy spectrum at the Pierre Auger Observatory is determined in Section 3.6. In addition, a brief summary of measurements done by other experiments is given is Section 3.7 where possible implications of the results are discussed.

3.1 Invisible energy

In Section 2.4.1, a description of the reconstruction of the calorimetric energy is given. To estimate the total energy of an extensive air shower (EAS) and obtaining thus the energy of the incoming high–energy particle, the invisible energy has to be taken into account. This energy is not deposited in the atmosphere being taken away by particles that can not be detected by the used measurement technique. The main focus of this Section is to infer the invisible energy down to the energies needed for the calculation of the energy spectrum from Cherenkov–dominated events.

At the highest energies, it is possible to infer the invisible energy of the FD measurements by investigating signals in the surface detector [41]. However, the results show that there is an apparent discrepancy between predictions of MC models of EASs and the data–driven estimates of the invisible energy, see Fig 3.1. Unfortunately, in the energy region below $10^{18.2}$ eV, no direct measurement is available yet.

In Fig. 3.1, the dashed line show the extrapolation of the Auger mesurements of the invisible energy down to 10^{17} eV. The idea of the extrapolation from the highest energies was also presented in Ref. [41]. A dependence of the mean logarithmic mass, $\langle \ln A \rangle$, on the calorimetric energy is used in order to constrain the estimate of the invisible energy. The extrapolation model of the invisible energy, $E_{\rm inv}$, is given by

$$E_{\rm inv} = \frac{K E_{\rm cal}^{\beta} A^{1-\beta}}{1 - \beta K E_{\rm cal}^{\beta-1} A^{1-\beta}}, \tag{3.1}$$

where K and β are model dependent parameters and $E_{\rm cal}$ is the calorimetric energy, respectively. This equation follows from the superposition model described in Section 1.2.2.

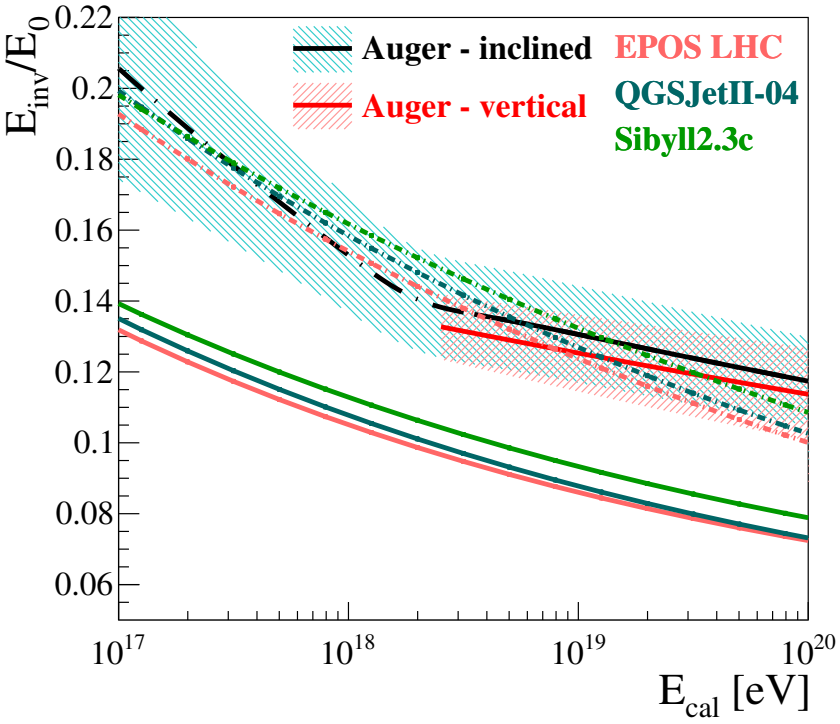

Figure 3.1: Invisible energy measured at the Pierre Auger Observatory. The result of the analysis of inclined showers is shown by black solid line, the black dashed line is an extrapolation to low energies. Uncertainty of the inclined measurement and its extrapolation is shown by blue band. The red line accompanied by the red uncertainty band depicts the result of the analysis of vertical showers. Predictions of MC simulations done with the three contemporary high–energy interaction models are shown by other color lines for protons (solid) and iron nuclei (dashed–dotted). The plot is taken from Ref. [41].

In the analysis of Cherenkov–dominated events, the Auger result, that includes the measured values of invisible energy from inclined showers as well as its extrapolation, is used down to 10^{17} eV. Below 10^{17} eV, the IceTop data are used as described in Section 3.1.1.

3.1.1 IceTop data

Estimation of the invisible energy from the data is based on the equation

$$E_{\mathrm{inv}} = \epsilon_{\mathrm{c}}^{\pi} N_{\mu}, \tag{3.2}$$

which comes from the Heitler–Matthews's model [7, 6]. In this equation, N_{μ} is the number of muons in an EAS that reach the ground and $\epsilon_{\mathrm{c}}^{\pi}$ is the pion critical energy, see also footnote [1)] in Section 1.2.2. Justification of Eq. (3.2) based on the detailed MC simulations is provided in Ref. [41].

Although no direct measurement of the invisible energy in the energy range of $10^{15} - 10^{17}$ eV exists, the number of muons can be extracted from the data published by the IceTop experiment [19]. The extraction of N_{μ} from the muon

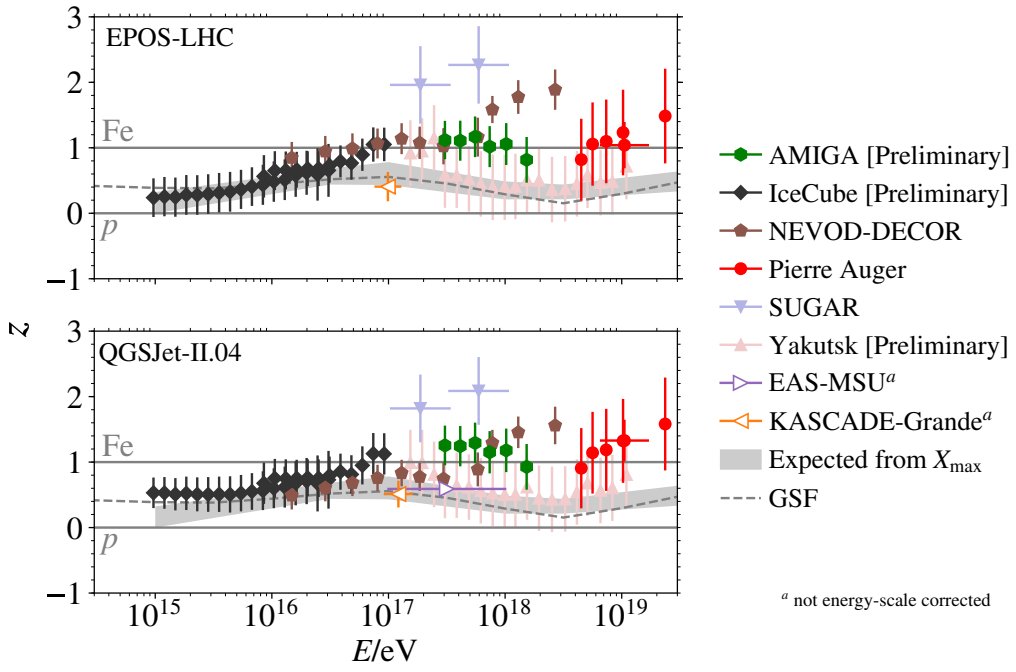

Figure 3.2: Number of muons at the ground recalculated to z reported by different experiments as a function of energy. The GSF was used to match the energy scales. Results under the condition of the EPOS LHC (upper panel) and the QGSJetII-04 (lower panel) high–energy interaction models are shown. Picture is adopted from Ref. [62].

densities at the ground reported by the IceTop was done in Ref. [62]. During the extraction, the global spline fit (GSF) model [20] has been used to compare results of different experiments. Within the GSF model, different experiments are matched utilizing their CR energy spectra which allows to compare their energy scales. Thus, the N_μ values coming from the IceTop data are attributed to the energies that would be reported by the Pierre Auger Observatory.

Technically, in Ref. [62] the z quantity is defined by

$$z = \frac{\ln(N_\mu^{\rm det}) - \ln(N_{\mu,{\rm p}}^{\rm det})}{\ln(N_{\mu,{\rm Fe}}^{\rm det}) - \ln(N_{\mu,{\rm p}}^{\rm det})}, \tag{3.3}$$

where $N_\mu^{\rm det}$ is the muon number estimate as seen in the detector, while $N_{\mu,{\rm p}}^{\rm det}$ and $N_{\mu,{\rm Fe}}^{\rm det}$ are the simulated muon number estimates for p and Fe induced showers, respectively, after a full detector simulation. The advantage of the z scale is in the cancellation of the systematic biases of the form of $\ln(N_\mu^{\rm det}) = A + B\ln(N_\mu)$. However, the simulated number of muons is dependent on the particular model of high–energy interactions, see Fig. 3.2. For the purpose of the invisible energy calculation, the QGSJetII-04 model [13] is chosen.

Utilizing Eqs. (3.2) and (3.3), the formula for the invisible energy is

$$E_{\rm inv} = E_{\rm inv,p}\left(\frac{E_{\rm inv,Fe}}{E_{\rm inv,p}}\right)^z, \tag{3.4}$$

where $E_{\rm inv,p}$ and $E_{\rm inv,Fe}$ are the invisible energies estimated by the chosen high–energy interaction model for protons and iron nuclei, respectively. Values of $E_{\rm inv,p}$

Table 3.1: Parameters of the invisible energy model below 10^{17} eV. Above 10^{17} eV, the values reported in Ref. [41] are used.

polynomial	a	b	c
P	4.213	-0.463	0.013
$P_{\rm low}$	3.838	-0.420	0.012
$P_{\rm up}$	4.623	-0.509	0.015

and $E_{\rm inv,Fe}$ are parametrized using CONEX simulations and z is taken directly from Ref. [62]. After a proper correction for the zenith angle dependence (average zenith angle of the IceTop showers used in the muon density analysis is 13° while for the Auger SD vertical showers it is 41°) of the invisible energy [41] and after the energy shift to the Auger energy scale, the invisible energy is evaluated according to Eq. (3.4). In the GSF, the Auger and IceCube energy scales are 87% and 108% of the GSF energy scale, respectively. The results are shown in Fig. 3.3 by green and orange points for the IceTop measurements at 600 m and 800 m core distances, respectively.

To combine these estimates with those at higher energies [41], a fit of the 2$^{\rm nd}$ order polynomial P

$$E_{\rm inv}/E_{\rm tot} = P(x) = a + bx + cx^2, \quad (3.5)$$

$$x = \log_{10}(E_{\rm cal}/{\rm eV}), \quad (3.6)$$

was performed to the data derived from IceTop in the energy range of $10^{15} - 10^{17}$ eV. The upper energy point at 10^{17} eV was fixed to the value reported in Ref. [41]. Systematic uncertainties were estimated combining the uncertainty reported in Ref. [41] and the one obtained by fitting the polynomials $P_{\rm low}$ and $P_{\rm up}$ to the IceTop lower and upper uncertainty bounds, respectively. For coefficients see Tab. 3.1. In Fig. 3.3, the black lines corresponds to the invisible energy model given in Eq. (3.5) above with systematic uncertainties shown by dashed lines.

In the estimate of the invisible energy, two breaks at calorimetric energies of 10^{17} eV and $10^{18.3}$ eV are present[1)]. They can be assigned to the changes in the composition of the primary beam of CR particles, see $\langle \ln A \rangle$ in Fig. 1.7 calculated using Ref. [20]. Although the current measurements of the mass composition in the energy range of $10^{15} - 10^{17}$ eV are largely uncertain, the change in the composition is evident. The very same $\langle \ln A \rangle$ from the GSF composition is used for the exposure calculation in Section 3.3.

However, the data–driven invisible energy is inconsistent with the expected invisible energy from MC simulations assuming the GSF composition [20]. Down to 10^{17} eV, this fact was reported by Auger in Ref. [41]. Below 10^{17} eV, the difference is getting smaller with decreasing energy and the data become consistent with the MC predictions within the reported systematic uncertainties.

[1)] The break at $10^{18.3}$ eV is present by construction which follows the change in $\langle \ln A \rangle$ measured by Auger as described in Ref. [41].

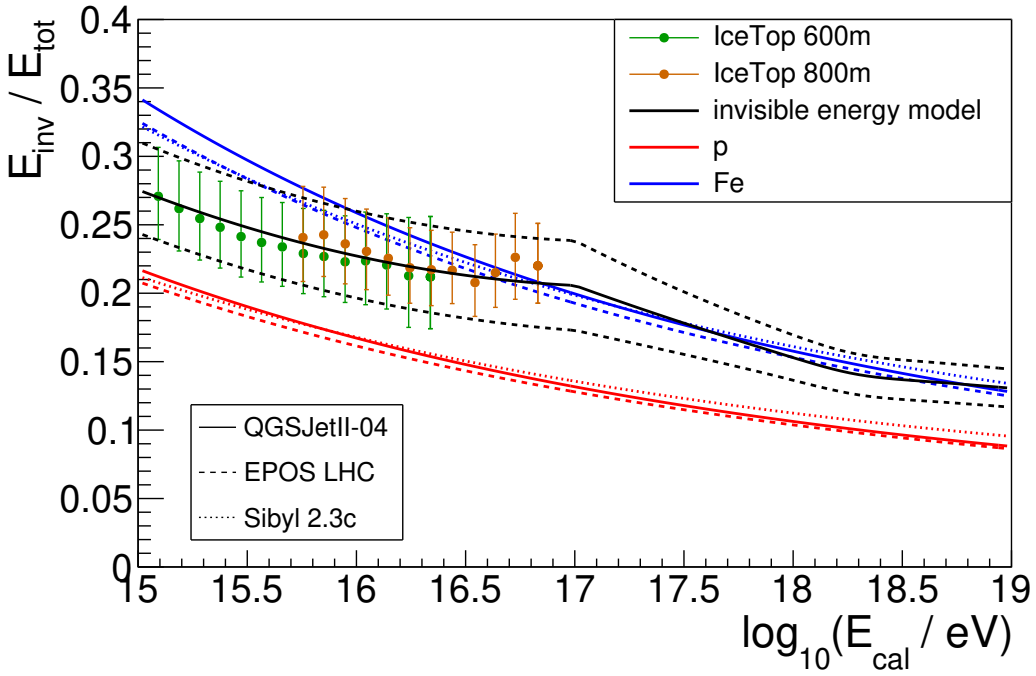

Figure 3.3: Invisible energy model (black line) estimated with the use of the IceTop data [19] (points). The high energy part above 10^{17} eV is fixed to the values reported in Ref. [41]. Dashed black lines show the systematic uncertainties. Error bars of the points correspond to the combined statistical and systematic uncertainties of the IceTop measurements. Red and blue lines correspond to the MC predictions for protons and iron nuclei, respectively. Picture comes from Ref. [A14].

3.2 Data set

The data set used for the calculation of the energy spectrum from Cherenkov–dominated data consists of two parts. The first part, dominating at higher energies, comes from the fully T3 triggered data recorded by the HEAT and/or Coihueco FD telescopes. The events that are measured by telescopes in both FD buildings are merged together with the standard procedure based on the trigger times[2)]. The second part of the data set is composed of HEAT events that do not pass the T3 level of the FD trigger. They are stored in the minimum bias data files[3)]. These files contain 10% of the TLT accepted but T3 rejected events, see the description of the FD triggers in Section 2.3. The loss of 90% of the T3 rejected data causes the necessity of weighting the minimum bias sample with respect to the T3 accepted data. It is done in a way that minimum bias data are weighted by a factor of 3 in the data sample (correspondingly, they are weighted by a factor of 0.3 in the Real–MC simulations where all TLT accepted events are available). This value turned out to be an optimal compromise between the loss of the statistical power of the data and the systematic uncertainty in exposure discussed in Section 3.5.2.

[2)] The full set of raw data after merging is available in the `ad_*.root` files.
[3)] Available as the FDAS `minbias_*.root` files.

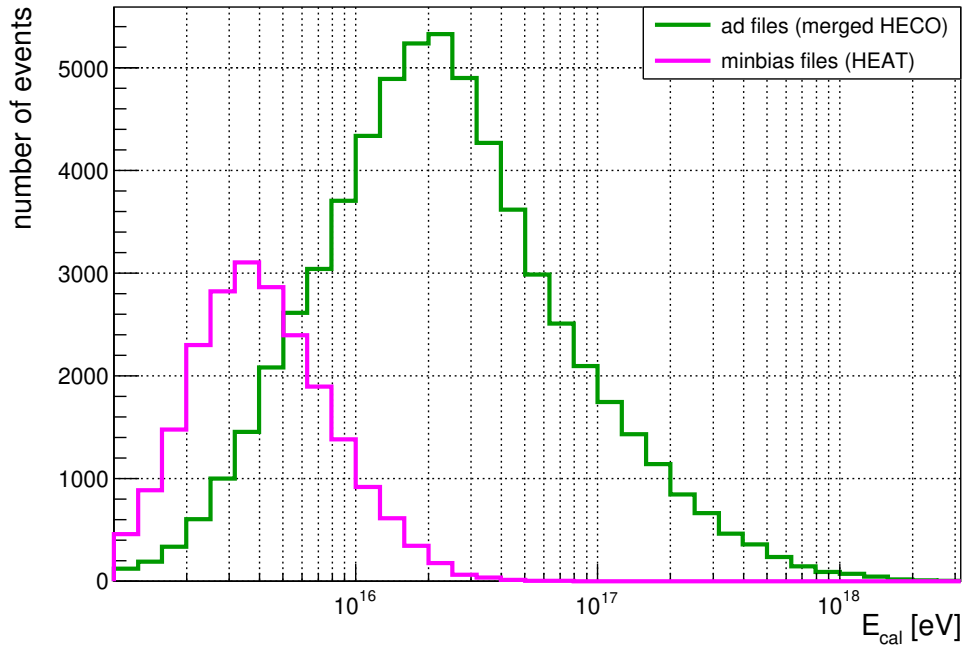

Figure 3.4: Energy distribution of the data. The green and magenta histograms represent the HEAT and Coihueco T3 triggered data and the HEAT minimum bias data, respectively. Both Detector and Quality cuts described in the text are applied.

The time period of the investigated data is between June 2012 and December 2017. It is limited by the trigger settings that are stable since the start of this period and the availability of the atmosphere monitoring database that has been released until the end of the year 2017.

The energy distributions of the data subdivided into the minimum bias and the T3 triggered data sets are shown in Fig. 3.4. They are processed by the same reconstruction algorithm that uses the PCGF method as described in Section 2.7. Details about the reconstruction settings are given in Appendix E.

A set of HEAT telescope No. 3 data is intentionally omitted in the analysis due to the technical problems with calibration. Also those time periods are cut from the analysis in which the detector and/or atmosphere status was not good enough. To achieve that, the Detector status cuts are applied, see their list in Appendix B. Moreover, the Quality cuts that ensure the necessary quality of the reconstruction are applied. They are listed and described in Appendix B. The fiducial volume cuts, described in Section 3.5.2, are treated as a part of the Quality cuts.

3.3 Exposure

In order to derive the energy spectrum, an exposure of the detector to the cosmic ray particles has to be calculated. The exposure of the FD measurements is not simply geometrical as for the SD measurements. Special attention has to be paid

to properly estimate the effect of the night sky background. This factor influences the T1 trigger, as described in Section 2.3, and effectively limits the distance until which the EASs can be detected. Therefore, detailed time dependent MC simulations of both the light emission from the EASs and the response of the FD telescopes are necessary. At the Pierre Auger Observatory, such simulations are called Real–MC. Details about the Real–MC method and the FD detector uptime calculations are described in Ref. [63]. The implementation of the detector simulations to the Cherenkov–dominated data is described in Appendix B.

Using the Monte Carlo approach to the exposure calculation, the Real–MC has to be adjusted to cover the same time period and the same FD telescopes as the data set described in Section 3.2. The most important assumption is that no event outside of the simulation region is able to trigger the detector. If this criterion is met, the total exposure, A, can be estimated through the fraction of triggered, reconstructed and selected events, N_{sel}, out of the total number of generated events, N_{gen}, which corresponds to the exposure A_{gen}

$$A = \frac{N_{\mathrm{sel}}}{N_{\mathrm{gen}}} A_{\mathrm{gen}}. \tag{3.7}$$

The generated exposure A_{gen} includes information about the time interval ΔT, area S and space angle Ω in which the simulations were performed

$$A_{\mathrm{gen}} = \Delta T S \Omega. \tag{3.8}$$

If isotropically distributed simulations are used, the exposure corresponds to the isotropic flux. To ensure that the isotropic particle flux on a flat surface S is used, the zenith angle, ϑ, distribution of generated showers follow

$$\frac{\mathrm{d}N_{\mathrm{gen}}}{\mathrm{d}\cos\vartheta} \propto \cos\vartheta, \tag{3.9}$$

as described in Appendix B.

The exposure of the HEAT and Coihueco FD telescopes to the Cherenkov–dominated events in the time period of 06/2012–12/2017 is shown in Fig. 3.5 as a function of energy. Both the Detector status and the Quality cuts are applied. To reduce the artificial fluctuations caused by limited MC statistics, the exposure is fitted by the polynomial function in log–log scale

$$A(E) = \exp\left(P_{12}\left(x\right)\right), \tag{3.10}$$

$$x = \log_{10}\left(E/\,\mathrm{eV}\right) - 17, \tag{3.11}$$

where P_{12} is the 12^{th} order polynomial. The order of the polynomial comes from the maximization of the χ^2 probability of the fit (≈ 0.16). The fit by the above mentioned function in Eq. (3.10) is motivated by the fact that the exposure exhibits a fine structure. It is associated with the admixture of the minimum bias data, with the limited field of view of the FD telescopes, and with the collimated emission of the Cherenkov light. This largely differs from the isotropic fluorescence emission used in the hybrid exposure calculation [63]. Moreover, in the hybrid exposure case, the fiducial field of view cuts are used to limit the composition dependence of the exposure. These cuts are not developed for the use with the Cherenkov–dominated data, so they are not used in the Cherenkov

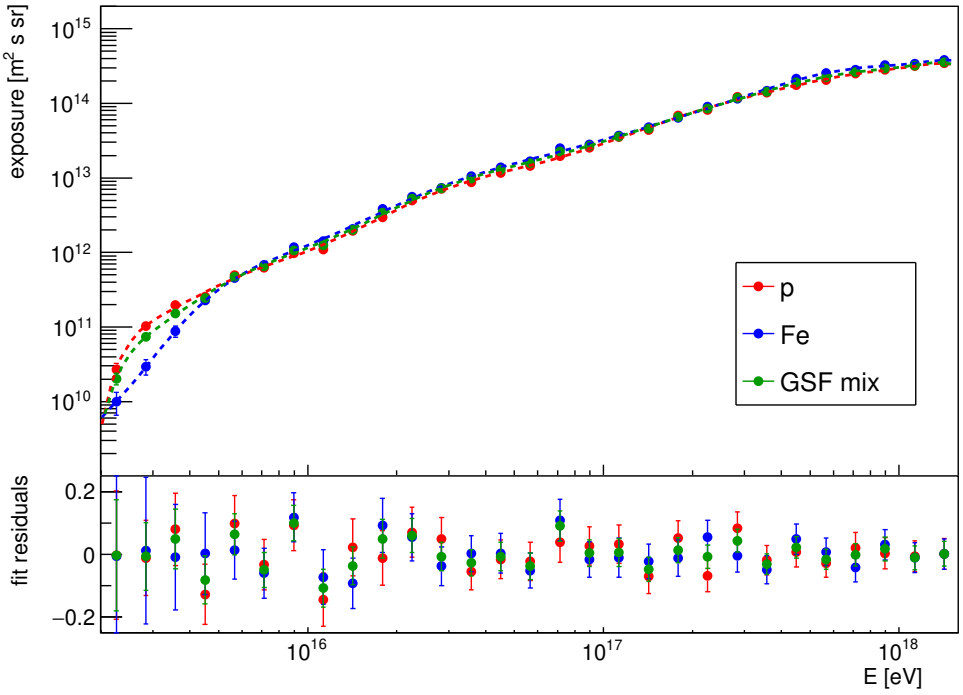

Figure 3.5: Exposure of the HEAT and Coihueco FD telescopes to the Cherenkov–dominated events in the time period of 06/2012–12/2017. Composition assumptions of pure protons, pure iron nuclei, and the mixed composition according to the GSF model are shown in red, blue, and green, respectively. Residuals to the fitted functions are shown in the bottom inset.

analysis. The fiducial field of view cuts should not be confused with the fiducial volume cuts described in Section 3.5.2.

This means that the exposure is dependent on a mass composition of primary particles. Actually, it is connected to the different acceptance of the FD for showers developed at different slant depths. A detailed view of how this affects the exposure is depicted in Fig. 3.6. Above the energy of 10^{16} eV, this effect is not large, but rather comparable to the statistical fluctuations of the Real–MC simulations shown in Fig. 3.5. The systematic uncertainty of the Cherenkov–dominated exposure attributed to the mass composition of primary particles is below 10% which is similar to the same source of the hybrid exposure uncertainty estimated in Ref. [63] for energies around 10^{18} eV. This behaviour is caused by convenient geometries of the incident Cherenkov–dominated events. For such events, the field of view of the FD telescopes covers a large range of slant depths.

In Fig. 3.5, the exposure corresponding to the mixed composition is determined from the mix of the proton and iron nuclei exposures that exhibits the same $\langle \ln A \rangle$ evolution with energy as the one from the GSF model discussed in Section 3.1, see Fig. 1.7. The result is close to the exposure calculated using the 50% + 50% mix of protons and iron nuclei, as documented in Fig. 3.6. The mixed–composition exposure is used as the nominal exposure in the energy spectrum analysis. Its uncertainty due to the not well known mass composition of primary particles is estimated by the difference between the mixed and the pure proton and iron nuclei exposures.

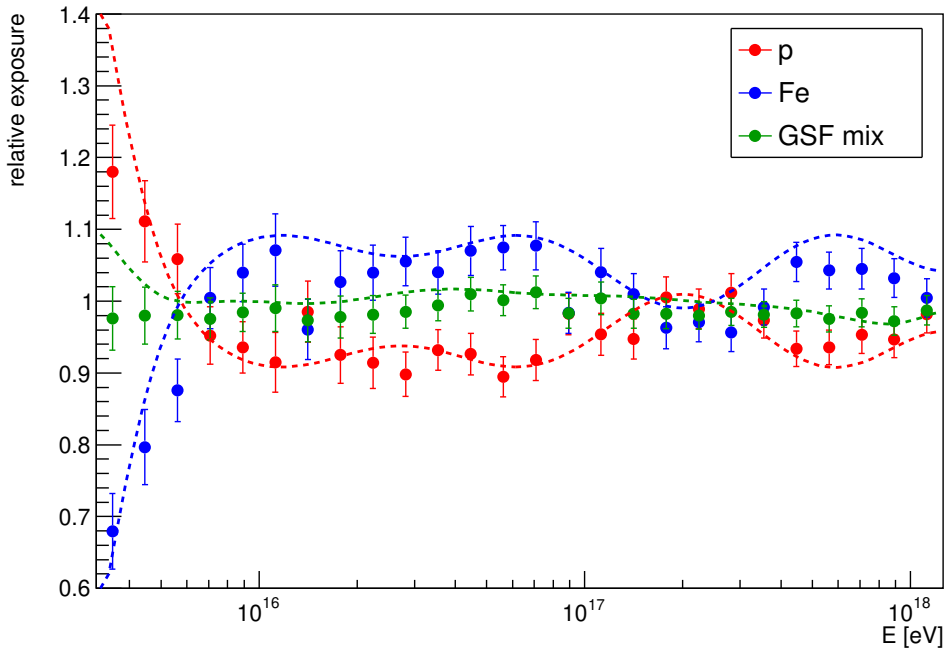

Figure 3.6: Mass composition dependence of the exposure. Differences between exposures from the 50% + 50% mix of protons and iron nuclei and pure beams are shown in red and blue for protons and iron nuclei, respectively. The green color represents the mixed composition exposure defined in the text. Points correspond to the point–by–point differences calculated from the extended Real–MC set, see Appendix B. Lines denote differences based on the fitted exposures.

Knowing the exposure, the raw energy spectrum is calculated. This spectrum is shown in Fig. 3.7.

3.4 Unfolding

An important effect that needs to be taken into account is the correction for the detector and reconstruction response (detector response in the rest of the text), the unfolding correction. This effect is estimated with the use of the Real–MC simulations and is connected to the precision of the PCGF reconstruction documented in Appendix C. The energy reconstruction bias is found to be below 5% of the true MC energy. The reconstruction resolution is better than 20% in the whole energy region between $10^{16} - 10^{18.1}$ eV. These values determine the width of the binning used in the analysis of the differential energy spectrum that is chosen to be 0.1 in the logarithm of energy which corresponds to $\approx 23\%$ of the average energy in the bin.

The complete information about the detector response is provided by the response matrix, $\mathbf{R}$. It is calculated from the migration matrix, $\mathbf{M}$, and the diagonal exposure matrix, $\mathbf{A}$, which has elements equal to the exposure binned in energy

$$\mathbf{R} = \mathbf{M} \cdot \mathbf{A}. \tag{3.12}$$

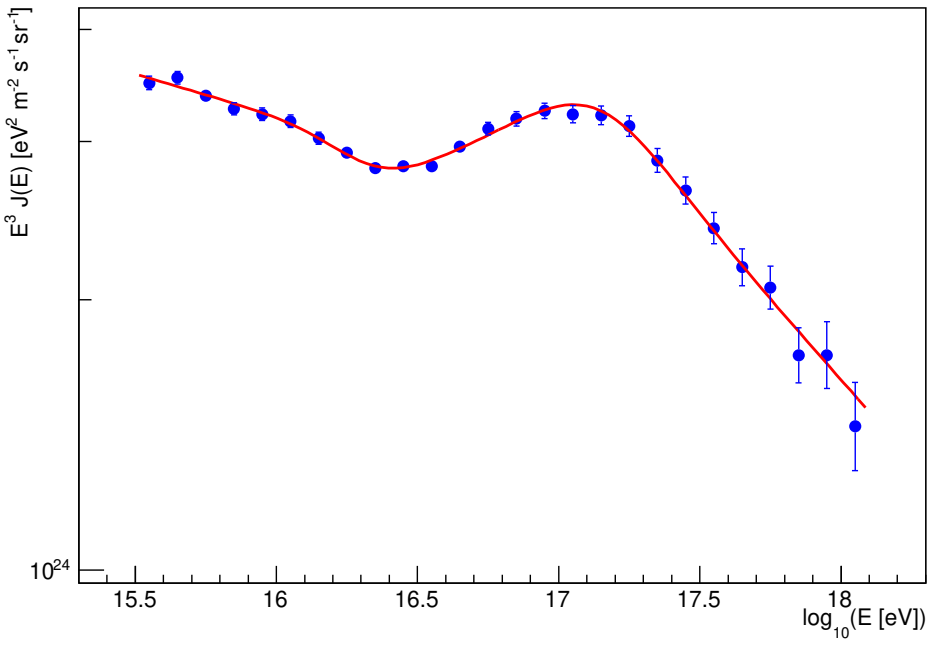

Figure 3.7: Raw energy spectrum (blue). Unfolding correction is not applied. Red line represents a fit by the function defined in Eq. (3.14). χ^2 probability of the fit is $p_{\chi^2} \approx 0.95$. Fit parameters are listed in Tab. 3.2.

The migration matrix captures the differences between the true MC energy, E_{MC}, and its reconstructed value, E_{rec}, stored in columns and rows, respectively. Each column of $\mathbf{M}$ is normalized to 1, including the underflow and overflow bins. Thus, each element M_{ij} represents the fraction of events migrating from the generated energy bin j to the reconstructed energy bin i.

The migration matrix estimated with the use of the extended Real–MC set, see Appendix B, is shown in Fig. 3.8 for the mixed composition defined in Section 3.3. It suffers from statistical fluctuations, caused by the limited simulation set, that would be propagated to the unfolding corrections. To suppress them, a smoothing of the matrix is performed as described in Appendix C. The smoothed migration matrix is shown in Fig. 3.9. The migration from lower to upper energy bins is crucial for the unfolding correction, because the flux of CRs falls steeply with approximately the third power of energy.

After the smoothing, the response matrix is calculated using Eq. (3.12). It is visualised in Fig. 3.10. The response matrix $\mathbf{R}$ is used to calculate the number of would be detected events in E_{rec} bins, $N_{\mathrm{exp},i}$, from any assumed differential energy spectrum J

$$\mathbf{N}_{\mathrm{exp}} = \mathbf{R} \cdot \mathbf{J}_{\mathbf{thr}}, \tag{3.13}$$

where $\mathbf{N}_{\mathrm{exp}}$ stands for the vector composed of $N_{\mathrm{exp},i}$ and vector $\mathbf{J}_{\mathbf{thr}}$ denotes the vector of thrown flux with components calculated as integrals of J in corresponding energy bins. This is utilized in the forward folding procedure that is widely used at the Pierre Auger Observatory to calculate the unfolding corrections.

Within the forward folding method, a functional form of the incident flux

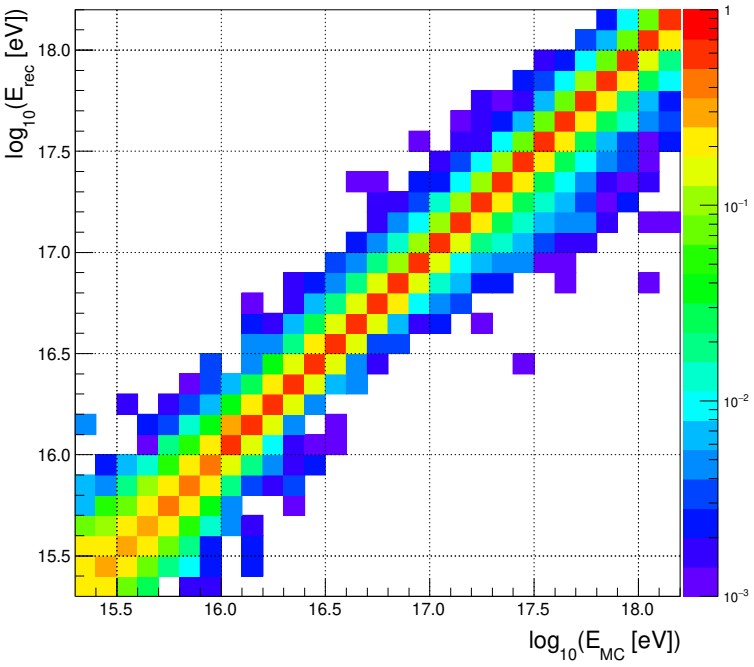

Figure 3.8: Visualization of the migration matrix estimated with the use of the extended Real–MC set, see Appendix B. Matrix is filled directly by the simulated events.

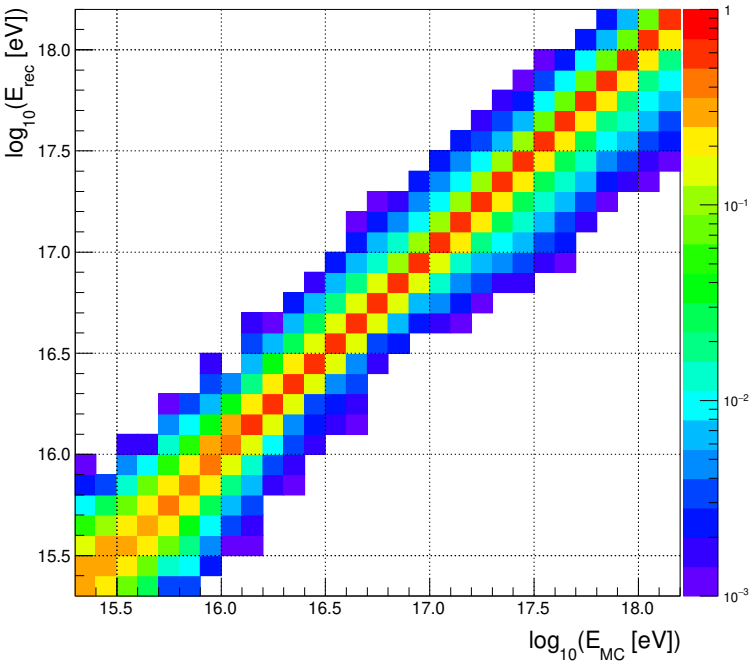

Figure 3.9: Visualization of the smoothed version of the migration matrix shown in Fig. 3.8. Smoothing procedure is described in Appendix C.

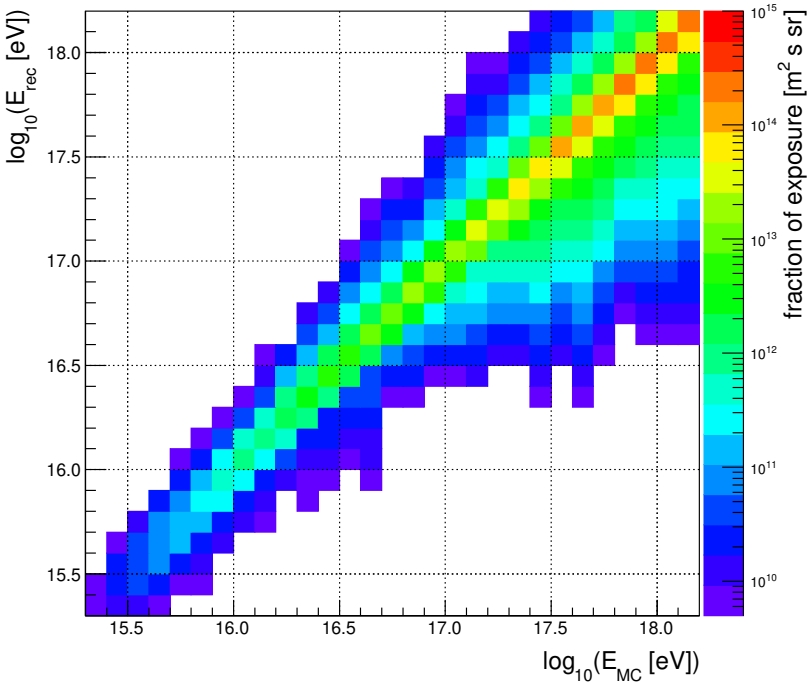

Figure 3.10: Visualization of the response matrix calculated with the use of Eq. (3.12) from the smoothed migration matrix shown in Fig. 3.9.

of CRs is assumed. The function is chosen to be able to describe the raw flux shown in Fig. 3.7. A smooth function is favoured over the broken power law to not produce artificial jumps in the unfolding corrections. The function of the following form is used for the Cherenkov spectrum unfolding

$$J(E) = J_0' \left(\frac{E}{E_{12}'}\right)^{-\gamma_1'} \prod_{i=1}^{3} \frac{1 + \left(E/E_{(i,i+1)}'\right)^{\gamma_{(i)}'}}{1 + \left(E/E_{(i,i+1)}'\right)^{\gamma_{(i+1)}'}}. \tag{3.14}$$

This function is characterized by the flux normalization J_0', four spectral indices $\gamma_1', \gamma_2', \gamma_3', \gamma_4'$, and three energies attributed to the break positions $E_{12}', E_{23}', E_{34}'$. The function fitted to the folded spectrum is shown by the red line in Fig 3.7. Goodness of the fit is described by the $p-$value of a test–statistic defined by the weighted sum of squared deviations which is used in the minimization

$$\chi^2_{\mathrm{w}} = \sum_{i=0}^{n} \frac{(J_i - J(E_i))^2}{\sigma^2_{Ji}}, \tag{3.15}$$

whose distribution follows the $\chi^2_{(n-k)}$ distribution ($p_{\chi^2} \approx 0.95$ for this fit). J_i and σ_{Ji} denote n measured fluxes at energies E_i and their uncertainties, respectively, while k stands for the number of fitted parameters of the flux function $J(E)$. Parameters coming from the fit are listed in Tab. 3.2.

In the unfolding procedure, all these parameters are varied. For each combination, the numbers of would be detected events, $N_{\mathrm{exp},i}$, are calculated with the use of Eq. (3.13). The Pearson's cumulative test–statistic is minimized in order

Table 3.2: Parameters of the Eq. (3.14) fit to the raw spectrum shown in Fig. 3.7. Statistical uncertainties are quoted. χ^2 probability of the fit is $p_{\chi^2} \approx 0.95$.

Parameter	Value $\pm$ $\sigma_{\text{stat.}}$
J_0 [m^{-2} sr^{-1} s^{-1} eV^{-1}]	$(3.20 \pm 0.02) \times 10^{-24}$
$\log_{10}(E_{12}$ [eV])	16.26 ± 0.04
$\log_{10}(E_{23}$ [eV])	16.28 ± 0.04
$\log_{10}(E_{34}$ [eV])	17.14 ± 0.04
γ_1	3.10 ± 0.01
γ_2	5 ± 3
γ_3	2.92 ± 0.02
γ_4	3.35 ± 0.03

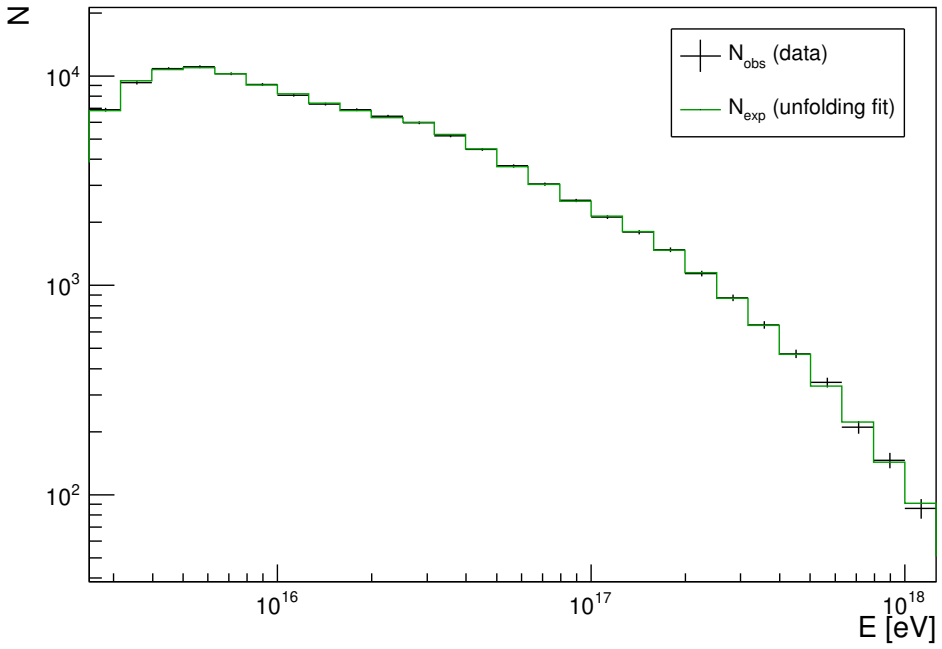

Figure 3.11: Result of the forward folding fit. The measured energy distribution is shown in black and the best matching distribution which arise from the forward folding fit is shown in green. χ^2 probability of the forward folding fit is $p_{\chi^2} \approx 0.68$.

to get the best description of the measured energy distribution (also following $\chi^2_{(n-k)}$)

$$\chi^2_{\text{P}} = \sum_{i=1}^{n} \frac{(N_{\text{obs},i} - N_{\text{exp},i})^2}{N_{\text{exp},i}}, \tag{3.16}$$

where $N_{\text{obs},i}$ stands for the number of observed events and n is the number of energy bins. The result of the forward folding fit is visualized in Fig. 3.11.

The final part of the forward folding method is the calculation of bin–by–bin corrections to the raw energy spectrum. The forward folded flux $\mathbf{J_{fold}}$ is related

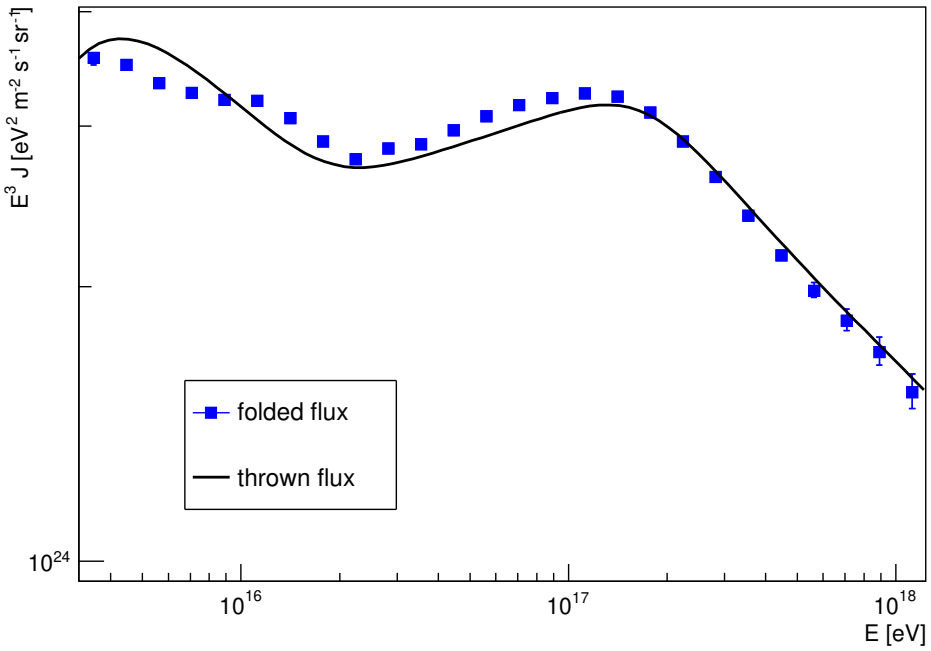

Figure 3.12: Thrown and forward folded fluxes shown in black and blue, respectively. The thrown flux shows the fitted function in Eq. (3.14) and the forward folded flux corresponds to the $\mathbf{J_{fold}}$ vector. Statistical uncertainties (error bars) of the folded flux come from the forward folding fit uncertainty in the thrown energy spectrum.

to the thrown flux $\mathbf{J_{thr}}$ through

$$\mathbf{J_{fold}} = \mathbf{A^{-1}} \cdot \mathbf{R} \cdot \mathbf{J_{thr}}, \tag{3.17}$$

where $\mathbf{A^{-1}}$ is the inverse matrix to the exposure matrix $\mathbf{A}$ defined in Eq. (3.12). Hence, the unfolding correction factors in each energy bin, c_i, are given by

$$c_i = \frac{J_{\mathrm{thr},i}}{J_{\mathrm{fold},i}}. \tag{3.18}$$

The thrown and folded fluxes coming from the forward folding fit are shown in Fig. 3.12 and the correction factors c_i are shown in Fig. 3.13.

The unfolded energy spectrum is shown in Fig. 3.14.

3.5 Systematic uncertainties

This Section deals with effects of systematic uncertainties on the energy spectrum measurement from Cherenkov–dominated events. The set of systematic uncertainties consists of uncertainties in exposure, dominated by the mass composition uncertainty described in Section 3.3, uncertainties in the energy scale, and uncertainty in the invisible energy. The treatment of effect of the energy scale uncertainty on exposure is described in Section 3.5.2.

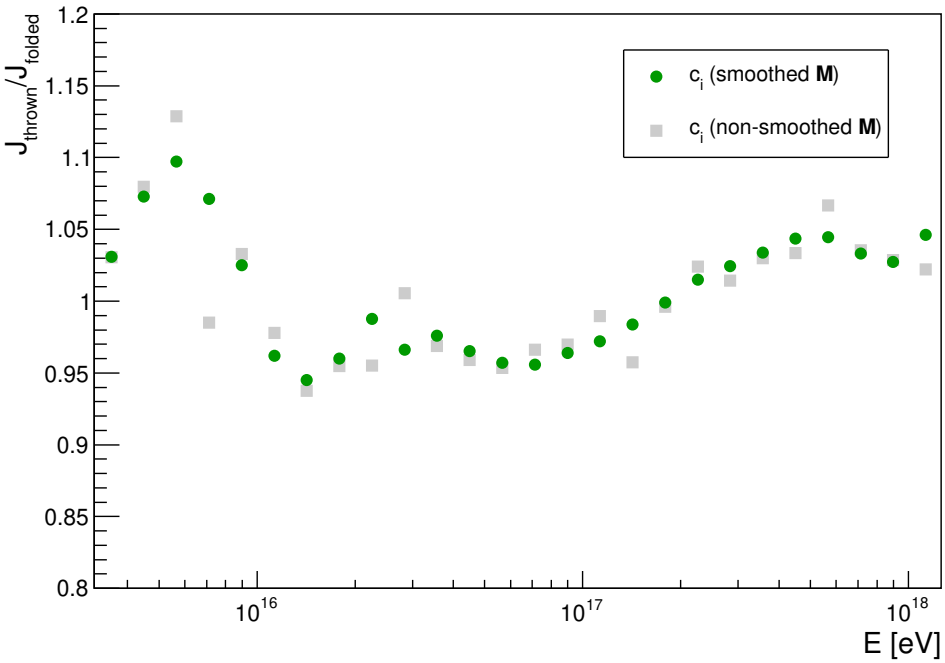

Figure 3.13: Unfolding correction factors to the raw energy spectrum. Correction factors arising from the smoothed **M** used in the analysis are shown by green circles. Gray squares correspond to the unfolding corrections obtained for **M** without smoothing, i.e. producing artificial fluctuations in the spectrum. Statistical uncertainties of the unfolding corrections coming from the forward folding fit are negligible.

3.5.1 Uncertainty in energy scale

The energy scale uncertainty is dominated by the uncertainty in calibration of the FD telescopes summarized in Section 2.10. On top of that, other sources of the energy scale uncertainty have been investigated [60]. Most of effects are common to the fluorescence–dominated and Cherenkov–dominated measurements. Identified and evaluated uncertainties in the energy scale relevant for the Cherenkov analysis are listed in Tab. 3.3. The energy dependent uncertainties evaluated in [60] are taken at the lower energy bound (3×10^{18} eV) that is close to the energies investigated herein.

The FD calibration uncertainty propagates directly to the reconstructed energy.

Uncertainty in the fluorescence yield is conservatively taken as the whole effect. However, its contribution varies within the data sample according to the Cherenkov fraction of the total measured light flux in particular events.

Cherenkov emission model is subject to the uncertainty estimated in Appendix A.

The contribution from the atmosphere is dominated by the uncertainty in the aerosol optical depth and its effect decreases with energy as the EASs are seen from closer distances.

The uncertainty connected to the reconstruction of the longitudinal profile of

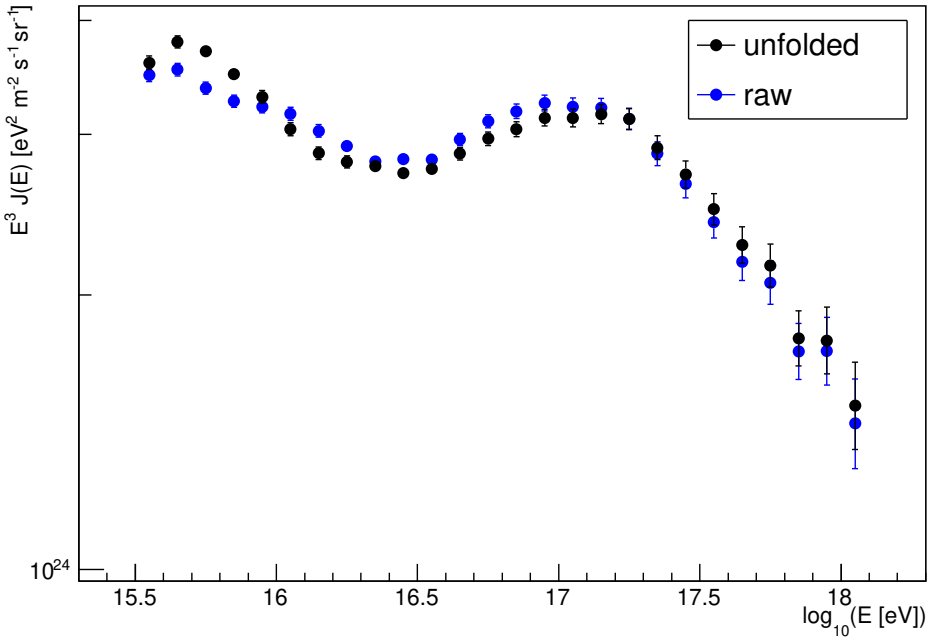

Figure 3.14: Unfolded energy spectrum of CRs derived from Cherenkov–dominated data shown in black. For comparison, the raw spectrum is depicted in blue.

Table 3.3: Systematic uncertainties in the energy scale of the Pierre Auger Observatory relevant for the Cherenkov–dominated measurements. Effects on the reconstructed energy are listed. The values reported in Ref. [60] as well as those calculated within this work are shown.

Quantity	Uncertainty
FD calibration	9.9%
fluorescence yield	3.6%
Cherenkov emission model	3%
atmosphere	3.4%
FD profiles reconstruction	6.5%
FD energy bias	2.5%
energy scale stability	5%
invisible energy	4%
total	**15%**

EASs is divided into several parts. The FD profile reconstruction uncertainty listed in Tab. 3.3 accounts mainly for the uncertainty in light collection, given that the image spot is a convolution of the optical point spread function and the finite width of the shower image. The effect of the apparent shower width in the direct Cherenkov light is evaluated in Appendix A and is accounted for in the Cherenkov emission model uncertainty.

The uncertainty in the FD energy bias, which is also connected to the lon-

gitudinal profile reconstruction, is estimated as a half of the maximum energy bias observed in simulations, see Appendix C. It is connected specifically to the reconstruction of Cherenkov–dominated events.

The energy scale stability is estimated by checking the stability of the SD energy calibration fits, Section 2.10, under different periods and/or under different conditions [60]. This uncertainty can arise both from the SD and/or FD calibration stability. Herein, it is conservatively attributed to the FD.

The invisible energy correction is described in Section 3.1. Above the energy of 10^{17} eV, its uncertainty increases with decreasing energy up to about 15% of its value. Below 10^{17} eV, the uncertainty is stable which arises from the systematic uncertainties of the IceTop measurements. Nevertheless, the effect of the uncertainty in the invisible energy on the total reconstructed energy is only about 4%.

3.5.2 Fiducial volume cuts

A special attention is given to the effect of the energy scale uncertainty on the exposure. A systematic shift in the amount of produced and/or detected light from EASs in Real–MC with respect to reality would cause a wrong assessment of the exposure to particular energies. Such effect would be represented by different number of detected ADC counts in FD pixels than expected from simulations. Motivated by the total energy scale uncertainty reported in Tab. 3.3, the fiducial volume cuts are developed to reduce this effect in case of up to 15% shift in energy.

The impact of the energy scale shift on exposure is estimated from Real–MC simulations by attributing shifted energies to the individual events in the MC sample and re–evaluating the exposure. By assessing lower energies, the lack of ADC counts in MC (excess of ADC counts in reality) is tested and vice versa. For this purpose, the extended Real–MC set has been used as described in Appendix B. If the 15% shift in energy is assumed and no fiducial volume cuts are applied, the impact on the exposure is shown in Fig. 3.15.

The fiducial volume cuts act on the R_{p} distance, see Fig. 2.8, and on the viewing angle VA_{Xmax} under which X_{max} of the EAS is seen. More precisely, VA_{Xmax} denotes the angle between the shower axis and the line connecting the position of the FD telescope with the largest number of triggered pixels and the point on shower axis that corresponds to the shower maximum. The R_{p} and VA_{Xmax} parameters are chosen due to following reasons. The largest amount of light is emitted at the shower maximum, thus the natural parameter that controls the trigger efficiency is the position of the shower maximum with respect to the FD telescope. The R_{p} parameter is chosen because it defines the distance between the shower maximum and the FD telescope for given X_{max} viewing angle VA_{Xmax}. On top of that, the amount of Cherenkov light emitted to particular angle from the shower axis decreases with increasing angle as shown in Fig. 2.4. Hence, VA_{Xmax} is chosen as the second fiducial volume parameter. It controls the amount of Cherenkov light seen by the FD telescope for given R_{p}.

To illustrate the above mentioned effects, the trigger and selection (detection) efficiency is examined in simulations. The number of detected events in the VA_{Xmax}–R_{p} space is shown in Fig. 3.16 for the energy bin of $10^{16.4} - 10^{16.5}$ eV.

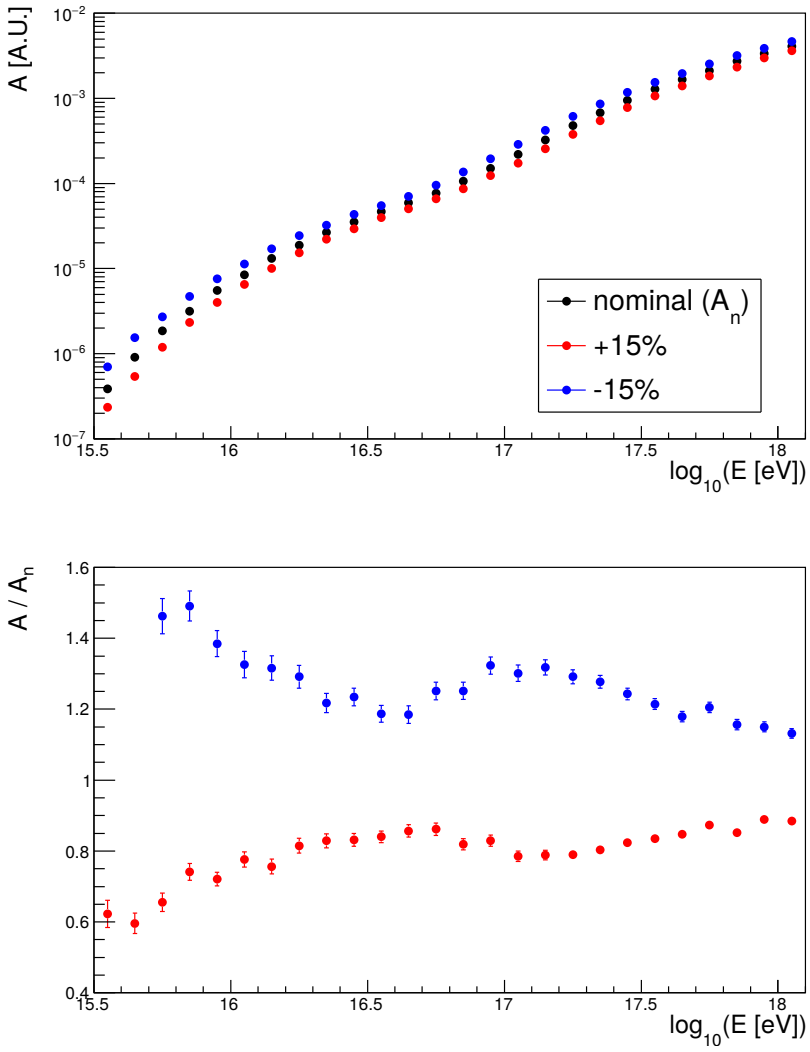

Figure 3.15: Impact of the energy scale uncertainty on exposure without fiducial volume cuts. Blue and red points correspond to the -15% and $+15\%$ shifts in energy, respectively. The relative differences of exposures with respect to the non–shifted case (black) are shown in the bottom inset.

Corresponding detection efficiency is shown in Fig. 3.17. The detection efficiency is compared between energy bins. For this purpose, the relative differences, $(\Delta\mathcal{E})_i$, between the detection efficiencies $\mathcal{E}_i$ and $\mathcal{E}_{i-1}$ in consecutive energy bins i are calculated

$$(\Delta\mathcal{E})_i = 1 - \frac{\mathcal{E}_{i-1}}{\mathcal{E}_i}. \tag{3.19}$$

$(\Delta\mathcal{E})_{15}$ for the example energy bin of $10^{16.4} - 10^{16.5}$ eV is visualized in Fig. 3.18. The fiducial volume is chosen to cover the region of small differences in the detection efficiencies. Following this procedure, a loss of exposure is present by construction because the accepted space of shower geometries at particular energy is reduced.

Using this idea, an analytical form of the fiducial volume cuts have been opti-

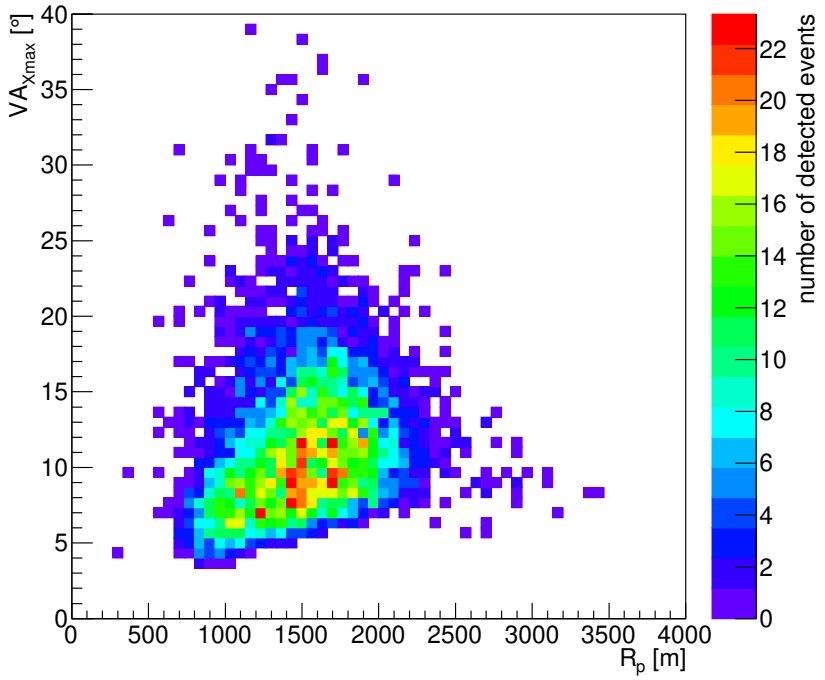

Figure 3.16: Number of detected events in the energy bin of $10^{16.4} - 10^{16.5}$ eV shown in the VA_{Xmax}–R_{p} space.

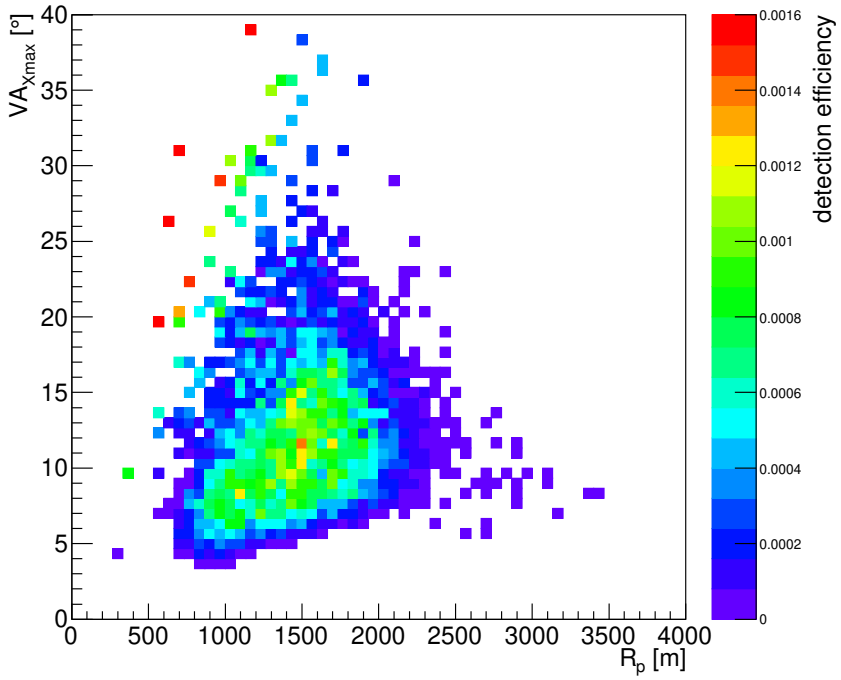

Figure 3.17: Detection efficiency for the same energy bin as in Fig. 3.16.

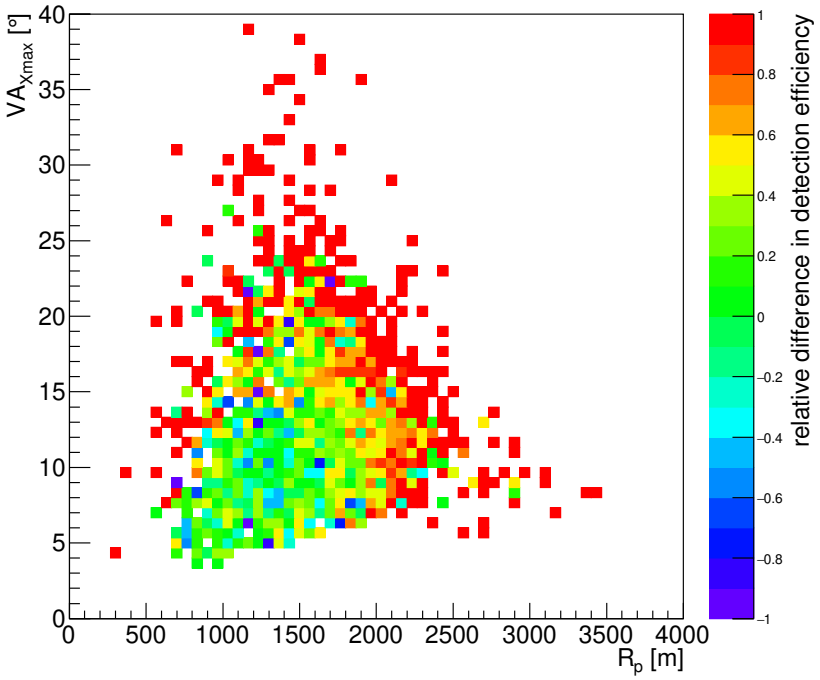

Figure 3.18: Relative difference in the detection efficiencies $(\Delta\mathcal{E})_{15}$ between the bins with energies of $10^{16.4} - 10^{16.5}$ eV and $10^{16.3} - 10^{16.4}$ eV is depicted. Area of small difference (green) corresponds to the fiducial volume. Negative values are caused by statistical fluctuations of Real–MC.

mized to reduce the differences in exposure in the case of the 15% shift in energies. The above described bin–by–bin analysis would lead to the cuts optimized for the shift of about 23% in energy connected to the 0.1 binning in the logarithm of energy. This would be too strict and would cause much larger loss in exposure. Resulting formulas for the maximum accepted $\overline{R_{\rm p}}$ and $\overline{VA}_{\rm Xmax}$ as functions of energy are shown in Fig. 3.19 and read

$$\overline{R_{\rm p}}\ [\rm m] = 141156 - 18104x + 584x^2, \tag{3.20}$$

$$\overline{VA}_{\rm Xmax}\ [^\circ] = \frac{25}{1+\exp\left(-3\left(x-16.9\right)\right)} + 8.5, \tag{3.21}$$

$$x = \log_{10}\left(E/\rm eV\right). \tag{3.22}$$

After the fiducial volume cuts are applied, the energy shift dependence of the exposure is highly reduced, see Fig. 3.20. To obtain the total uncertainty in exposure, the remaining energy shift uncertainty is further summed in quadrature with the energy independent contribution of 5% which is associated with the residuals of the exposure fit in Fig. 3.5, with the on–time calculation described in Ref. [63], and with the limited generation area of Real–MC described in Appendix B. The only effect on exposure that is not included here is the mass composition uncertainty in acceptance which is estimated in Section 3.3.

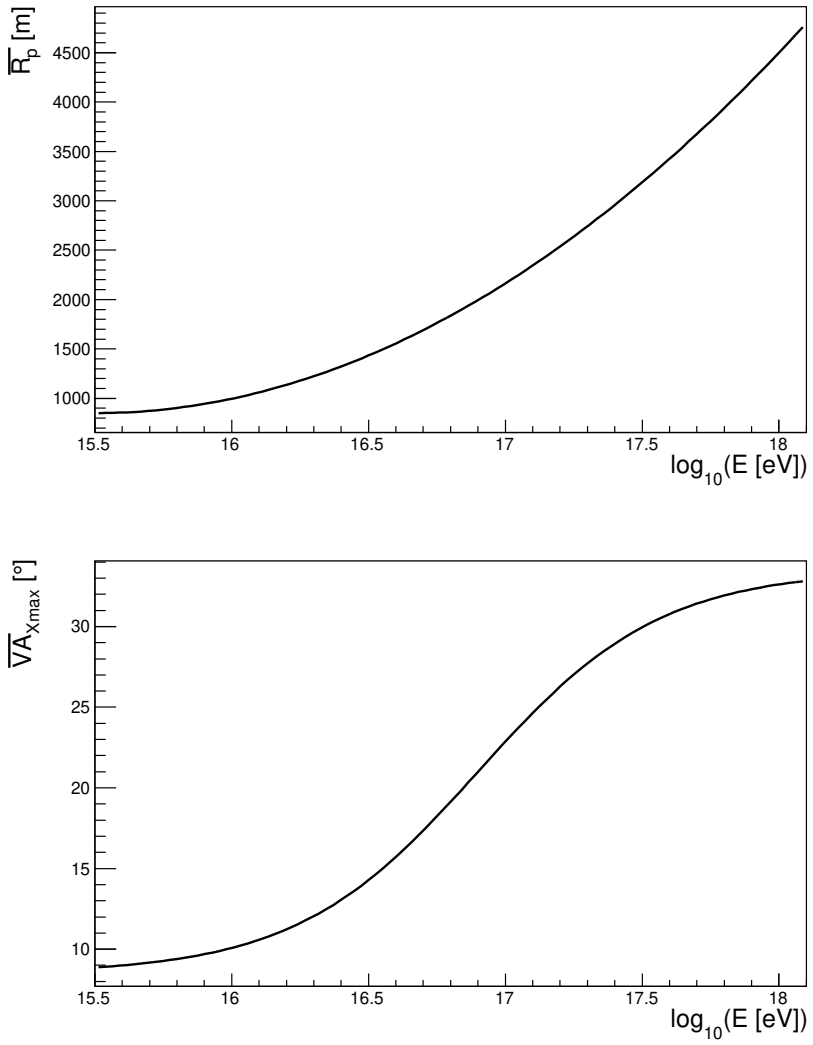

Figure 3.19: Fiducial volume cuts on VA_{Xmax} and R_{p}. Maximum accepted values $\overline{R_{\mathrm{p}}}$ (top panel) and $\overline{VA}_{\mathrm{Xmax}}$ (bottom panel) as functions of energy are depicted. Parametrizations are defined in Eqs. (3.20 and (3.21) for $\overline{R_{\mathrm{p}}}$ and $\overline{VA}_{\mathrm{Xmax}}$, respectively.

3.5.3 Propagation to energy spectrum

After the relevant systematic uncertainties are addressed, their propagation to the flux of CRs is investigated.

The uncertainty in the invisible energy (E_{inv}), Section 3.1, is treated separately from the the rest of energy scale uncertainties listed in Tab. 3.3. By definition, it does not affect the measured quantities, i.e. the number of measured ADC counts discussed in Section 3.5.2. To address the effect of E_{inv}, four different scenarios are assumed and for them the whole analysis is redone (the definition of cuts is unchanged and the exposure calculation, energy assignment to the data, and the unfolding procedure are repeated). They are $\pm\sigma_{syst.}$ shifts in E_{inv} derived in Section 3.1 and two (p and Fe) pure beam scenarios simulated in CONEX by QGSJetII-04 high–energy interaction model. The results of pure proton and

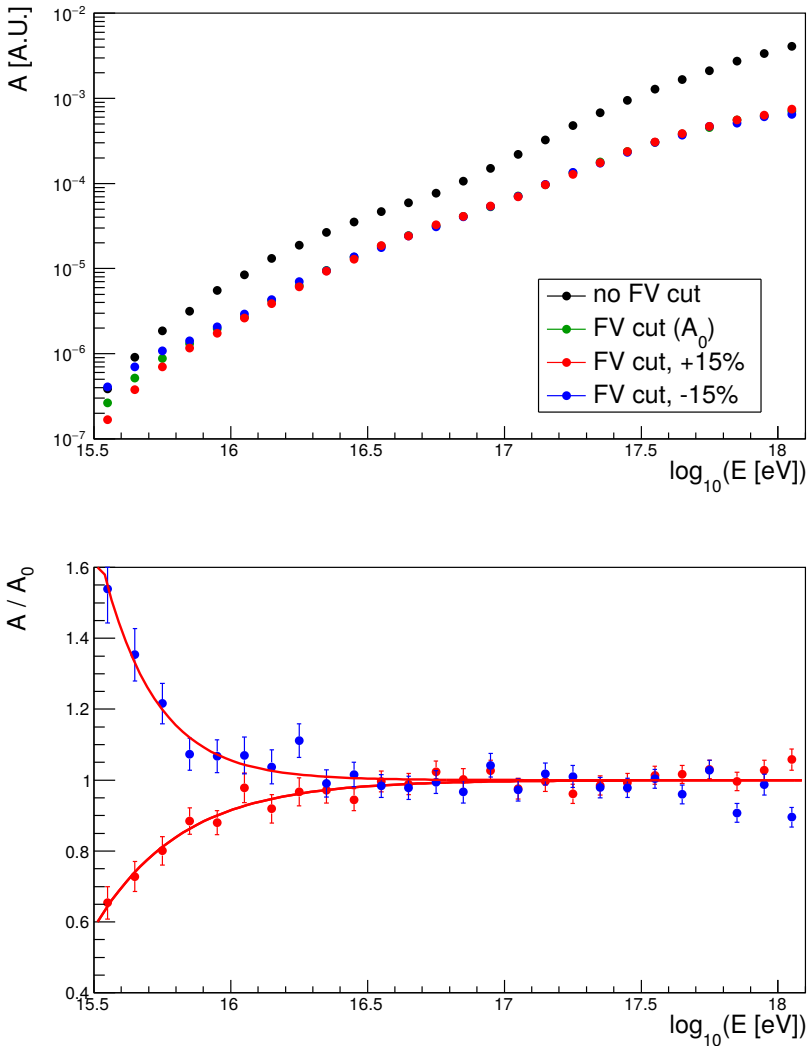

Figure 3.20: Impact of the energy scale uncertainty on exposure after fiducial volume cuts are applied. The color coding is the same as in Fig. 3.15. Green points correspond to the exposure calculated using nominal energies cut by fiducial volume (FV) cuts. To see the loss of exposure, its nominal values without fiducial volume cuts from Fig. 3.15 are depicted as well. In the bottom inset, the residual uncertainty in exposure is parametrized by red lines.

iron nuclei simulations of $E_{\rm inv}$ are disfavoured by the data–driven systematic uncertainties shown in Fig. 3.3. Nevertheless, they are investigated to prove that the break in $E_{\rm inv}$ model at 10^{17} eV, not present in the pure beam cases, is not responsible for the presence of the break in the energy spectrum also around 10^{17} eV. The impact of $E_{\rm inv}$ on the energy spectrum is illustrated in Fig. 3.21. The systematic uncertainty in flux corresponding to $E_{\rm inv}$ model is defined as the region between the blue ($-\sigma_{syst.}$) and red ($+\sigma_{syst.}$) spectra.

Furthermore, also other systematic uncertainties propagated to the CR flux measurement are shown in Fig. 3.22. They are associated with the above mentioned invisible energy model (green boxes), with the mass composition depen-

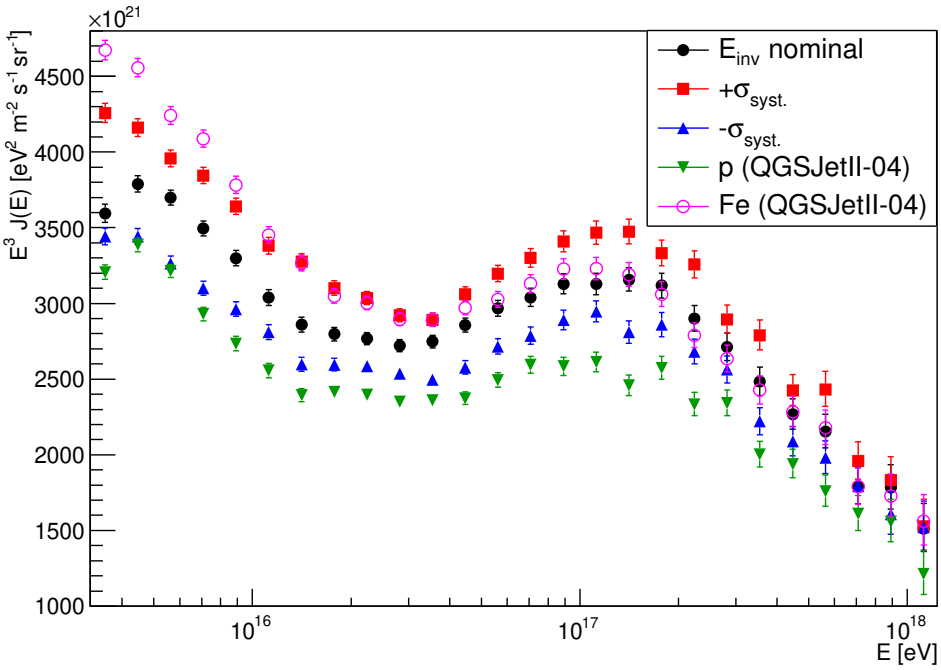

Figure 3.21: Impact of the uncertainty in $E_{\rm inv}$ on the energy spectrum. The energy spectra determined with the use of the nominal (black), $+\sigma_{syst.}$ (red), and $-\sigma_{syst.}$ (blue) systematic uncertainty shifts in $E_{\rm inv}$ are shown. The green and magenta points correspond to $E_{\rm inv}$ determined from the QGSJetII-04 simulated pure beams of protons and iron nuclei, respectively. The pure beam cases are disfavoured by $E_{\rm inv}$ systematics, see Fig. 3.3.

dence of the FD acceptance (dark red boxes) described in Section 3.3, and with the systematic uncertainty in exposure (blue boxes) discussed in Section 3.5.2. However, the most important source of uncertainty is the one in the Auger energy scale (gray boxes), see Tab. 3.3. It is dominated by the absolute uncertainty in the detector calibration and is to a large extent common to all measurements done at the Observatory. The invisible energy estimate compose one part of this uncertainty and is also common to all Auger measurements. Thus, it is not included in the uncertainty uncorrelated between Auger data that is shown by red brackets in Fig. 3.22. On the other hand, the uncertainties in the Cherenkov emission model and the FD energy bias, listed in Tab 3.3, contribute to the Auger uncorrelated uncertainty as they are not common to the hybrid measurements. In Fig. 3.22, the total systematic uncertainty in the energy spectrum determination from Chernekov–dominated data is depicted by black brackets.

The same information as in Fig. 3.22 is shown in Fig. 3.23 where the relative systematic uncertainties in CR flux are evaluated. Above the energy of 10^{16} eV, all contributions to the uncertainty in the energy spectrum are similar in size ($\approx 5-10\%$), except for the absolute energy scale ($\approx 35-50\%$). While the energy scale, which determines the total systematic uncertainty, is crucial for the comparison of the Auger energy spectrum with the results of other experiments, the Auger uncorrelated uncertainty ($\approx 12\%$) is important to properly compare different results provided within the Pierre Auger Collaboration, see Section 3.6.

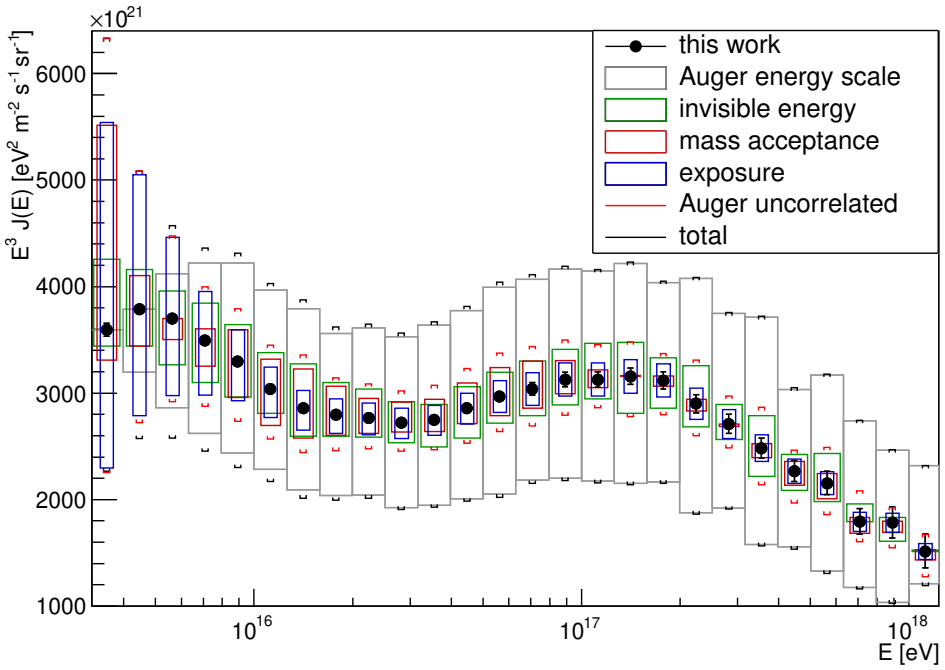

Figure 3.22: Systematic uncertainties propagated to the energy spectrum. Uncertainties associated with the energy scale (gray boxes) and its part E_{inv} (green boxes) described in Sections 3.5.1 and 3.1, respectively, are shown. Uncertainties in exposure visualized in Figs. 3.6 and 3.20 for the mass composition acceptance (red boxes) and the energy scale dependence (blue boxes), respectively, are also depicted. The total systematic uncertainty is denoted by black brackets and the one that is uncorrelated with other Auger measurements is given by red brackets.

3.5.4 Time stability

To test the time stability of the energy spectrum measurement, the data set has been divided into two time periods with roughly the same statistical power. The time of the division is the end of June 2015. For both independent data sets, the energy spectrum has been recalculated and compared with the one obtained for the whole data set. Above the energy of 10^{16} eV, the results are compatible within the statistical uncertainties as shown in Fig. 3.24. Below this energy, a discrepancy of up to $\pm 10\%$ is found which may be connected to the increase of the exposure uncertainty in this energy region.

3.6 Combined spectrum

In Section 2.10, individual estimates of the energy spectrum done at the Pierre Auger Observatory are introduced. Four of them (hybrid, SD 1500 vertical, SD 1500 inclined, and SD 750) share exactly the same energy scale uncertainty of 14% reported in Ref. [60]. It is the absolute uncertainty in the energy determination for the hybrid measurements. As described in Section 2.10, this uncertainty is propagated to the SD measurements through the energy calibration procedure.

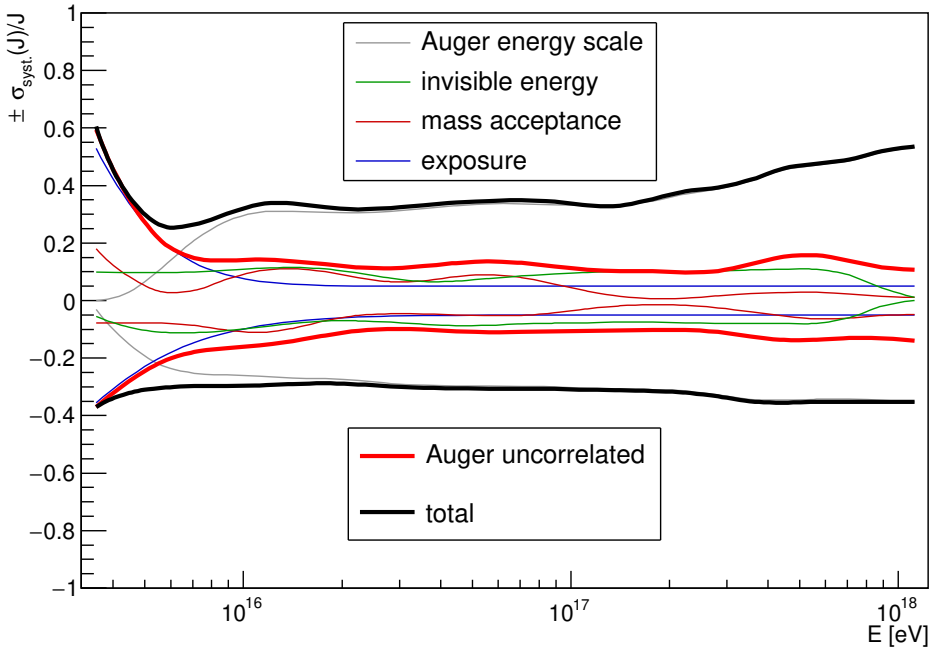

Figure 3.23: Relative systematic uncertainties in the energy spectrum. Systematic shifts in flux corresponding to uncertainties from Fig. 3.22 are shown as functions of energy. Smoothing was applied.

Table 3.4: Systematic uncertainties in the CR flux uncorrelated between the Auger measurements (middle column) and the normalization shifts arising from the spectrum combination (right column). Statistical uncertainties in shifts from the combination fit are listed.

Method	Uncertainty	Normalization shift
hybrid	7%	$-6.5^{+1.0}_{-1.0}$%
SD 1500 vertical	3%	$0.1^{+0.6}_{-0.6}$%
SD 1500 inclined	5.5%	$4.0^{+0.8}_{-0.8}$%
SD 750	4%	$0.4^{+0.8}_{-0.8}$%
Cherenkov–dominated	12%	$2.6^{+1.1}_{-1.1}$%

The Cherenkov–dominated spectrum also share this uncertainty, see Section 3.5.1, although its energy scale uncertainty is a little bit larger due to the presence of additional uncertainties in the Cherenkov emission model and FD energy bias listed in Tab. 3.3.

To combine the Auger energy spectra into one, the systematic uncertainties in CR flux uncorrelated between individual estimates of the energy spectrum have to be derived. For the Cherenkov–dominated analysis, they are estimated in Section 3.5.3 and depicted in Figs. 3.22 and 3.23. Uncorrelated uncertainties of Auger measurements are summarized in Tab. 3.4. For the purpose of the combination presented herein, a small energy dependence of the uncorrelated systematic uncertainties provided by all investigated measurements is neglected.

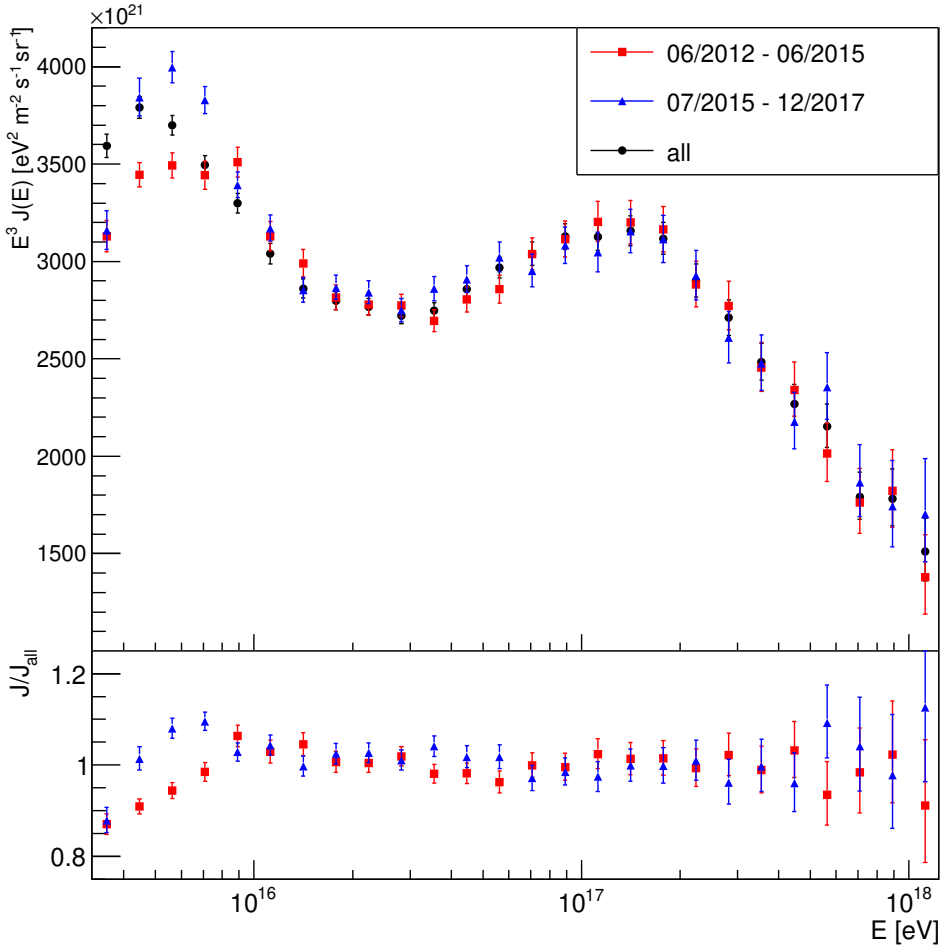

Figure 3.24: Time stability of the energy spectrum. The data set is divided into two parts, 06/2012–06/2015 (red) and 07/2015–12/2017 (blue). For them, the energy spectra are independently derived (top inset). Residuals from the all–data spectrum (black) are shown in the bottom inset.

The combined energy spectrum shown in Fig. 3.25 is calculated following the procedure described in Ref. [64]. This method is based on the maximum likelihood estimate that takes into account systematic uncertainties of individual measurements as well as the statistical power of different spectra. The systematic uncertainties constrain the normalization shifts listed in Tab. 3.4 that arise from the spectrum combination. The normalization shifts are applied to the individual energy spectra to match the most likely overall normalization of the combined spectrum. Larger uncertainty in the Cherenkov–dominated normalization shift is caused by larger uncorrelated uncertainty of the measurement with respect to the rest of the methods and by larger statistical uncertainties in comparison with the SD 750 measurement [65] in the common energy range. Their comparison is shown in Fig. 3.26.

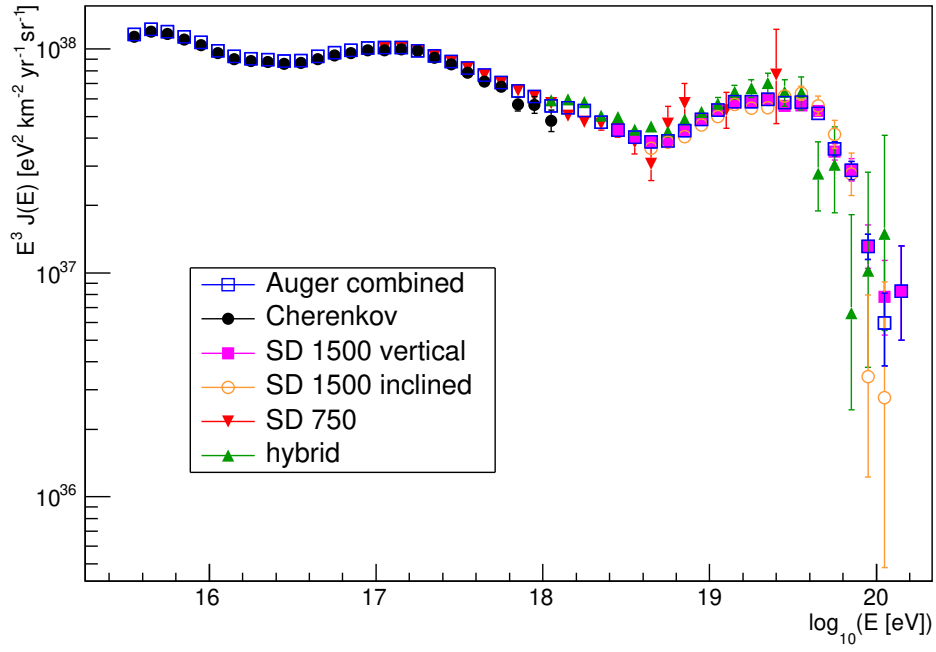

Figure 3.25: Energy spectrum combined from measurements performed at the Pierre Auger Observatory. Markers denote different estimates of the energy spectrum described in Section 2.10. Energy spectrum from Cherenkov–dominated data is depicted by black circles. The combined spectrum is shown by blue squares. Error bars correspond to statistical uncertainties.

3.7 Interpretation

In the energy range of $10^{15} - 10^{18}$ eV, several techniques are used to detect EASs. Predominantly, ground arrays of detectors are used. They measure either the charged particles by scintillator or water–Cherenkov detectors, or the Cherenkov light produced by EASs with the use of non–imaging Cherenkov counters. Advantages of the particle detectors are in their duty cycle and possibility to distinguish between the electromagnetic and muonic components. On the other hand, the Cherenkov counters provide measurements of light integrated over the whole development of EASs. In the near future, the detection of radio emission from EASs may combine advantages of the $\approx 100\%$ duty cycle and the integral measurements of longitudinal profiles of EASs. An exposure of the ground–based particle detectors can be estimated easily, especially above the energy threshold for full efficiency of the array. To the contrary, the exposure of experiments based on the electromagnetic emission from EASs is, in general, energy dependent and rely on simulations.

The Auger energy spectrum derived from Cherenkov–dominated data is compared with measurements of other experiments in Fig. 3.27. Results of different experiments are compatible with the Auger spectrum within its systematic uncertainties. It is worth mentioning that the majority of ground based experiments measuring the charged particles, represented by Tibet [66], Kascade–Grande [67], and IceTop [68] measurements in Fig. 3.27, is calibrated with the use of MC

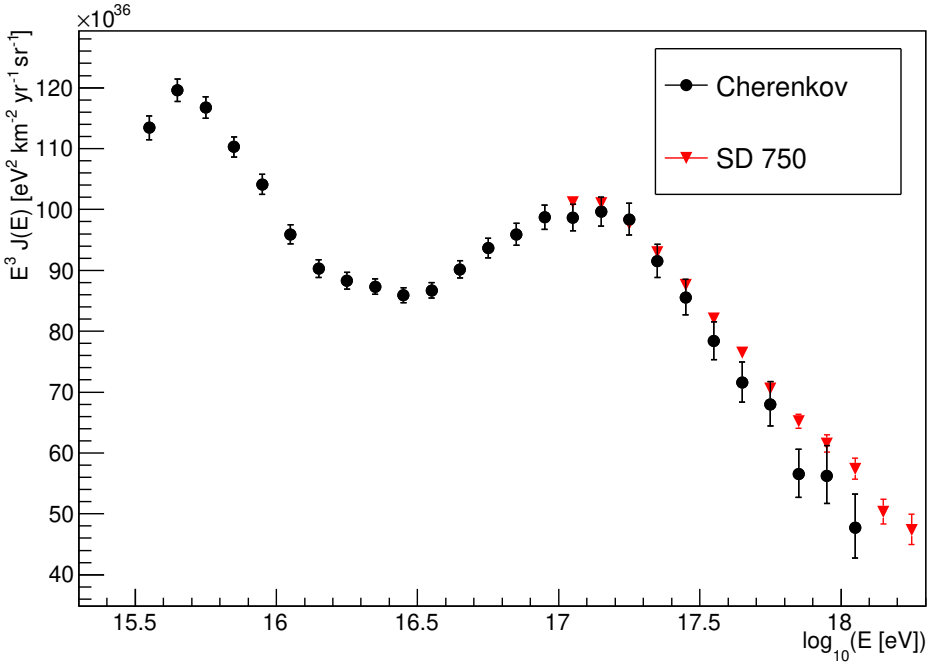

Figure 3.26: Energy spectrum from Cherenkov–dominated data (black circles) compared with the one from the SD 750 measurement [65] (red triangles). Statistical uncertainties are shown.

simulations. The Yakutsk [69] and Tunka [70] experiments use non–imaging Cherenkov counters that allow for less MC dependent calibration. However, the best precision is expected from detectors calibrated with the use of calorimetric energy measurements provided by the FD telescopes, currently implemented at the Pierre Auger Observatory and the Telescope Array (TALE) [54] experiments.

It should be noted that the Cherenkov–domianted data measured by the Auger detectors indicate systematically lower flux than the other experiments. A similar effect is observed also at higher energies [71]. Being under unprecedented control, the energy calibration of the FD telescopes at the Pierre Auger Observatory may explain these discrepancies.

Besides the overall cubic decrease with energy discussed in Section 1.1, the energy spectrum of cosmic rays exhibits several Knee–like and Ankle–like features visible in Fig. 3.25. These features are usually explained as a consequence of the rigidity, R, dependent acceleration in sources

$$R = \frac{Pc}{Ze}, \tag{3.23}$$

where P is the total momentum of a nucleus and Ze denotes its electric charge. Particles with the same R are influenced by magnetic fields in the same way. Thus, if there is a maximum energy $E_{\max}(Z=1)$ up to which protons can be accelerated in a source (a diffusion acceleration allowed by magnetic fields is assumed), the maximum energy for nuclei scales as [72]

$$E_{\max}(Z) = ZE_{\max}(Z=1). \tag{3.24}$$

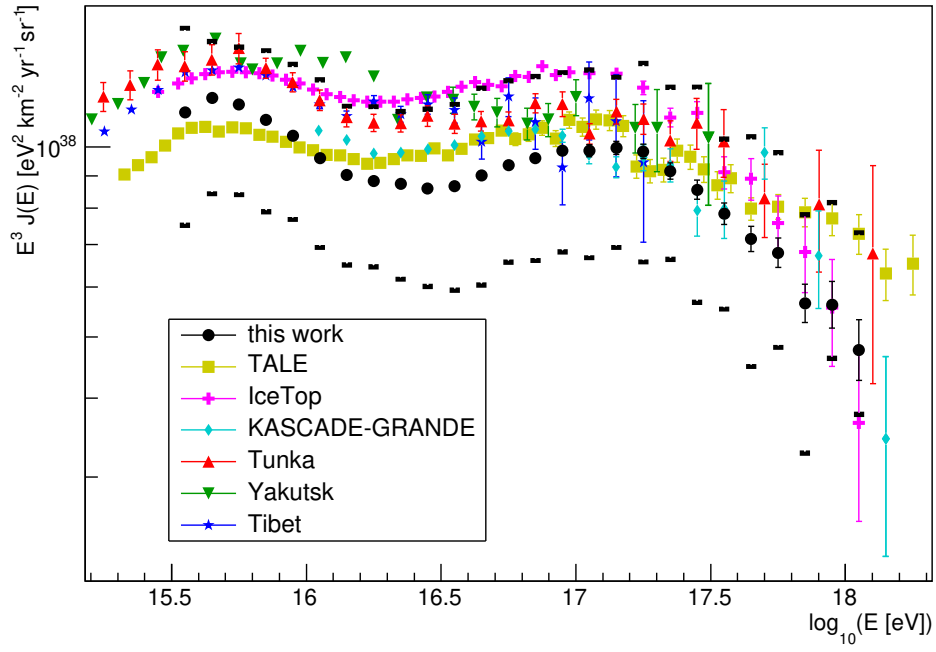

Figure 3.27: Energy spectrum of different experiments compared with the one obtained from Cherenkov–dominated data at the Pierre Auger Observatory (black). The all–particle spectra of Tibet [66], Yakutsk [69], Tunka [70], Kascade–Grande [67], IceTop [68], and TALE [54] are shown. Their results are compatible with the Auger spectrum within its systematic uncertainties denoted by black brackets.

Taking into account different abundances of nuclei with respect to protons in the source matter, the spectral features naturally arise from convolution of energy spectra of individual source–escaping particles. To describe the CR flux from the Knee region ($\approx 10^{15.5}$ eV) up to the highest energies, at least three populations of sources with different $E_{\max}$ are expected [73]. This hypothesis is supported by the mass composition measurements, although still uncertain, that favour rapid changes in $\ln A$ (A denotes the mass number) of CR primaries with energy, see Fig. 1.7. Alternatively, the features at the highest energies can be interpreted by a pure proton spectrum favoured by the Telescope Array measurements [74]. In this case, the Ankle dip at about $10^{18.7}$ eV and the cut–off above $10^{19.7}$ eV are caused by interactions of protons with the cosmic microwave background radiation, namely by the production of electron–positron pairs [75] and the photo–pion production [76, 77], respectively.

Positions of breaks in the energy spectrum as well as derived spectral indices are compared between different experiments. For this purpose, the broken power

law fit is usually performed and reported

$$
\begin{aligned}
J(E) &= \begin{cases}
J_0 \left(\frac{E}{E_0}\right)^{-\gamma_1}, & \text{for } E \leq E_1 \\
J_0 \left(\frac{E_1}{E_0}\right)^{-\gamma_1} \left(\frac{E}{E_1}\right)^{-\gamma_2}, & \text{for } E_1 < E \leq E_2 \\
\ldots & \\
J_0 \left(\prod_{i=0}^{n-1} \left(\frac{E_{(i+1)}}{E_{(i)}}\right)^{-\gamma_{(i+1)}}\right) \left(\frac{E}{E_{(n)}}\right)^{-\gamma_{(n+1)}}, & \text{for } E_{(n)} < E
\end{cases} \\
E_0 &= 10^{16} \text{ eV},
\end{aligned}
\tag{3.25}
$$

where γ_i stand for $n+1$ spectral indices in consecutive energy regions, E_i denote n positions of breaks, and J_0 is the flux normalization at the reference energy E_0. Result of the broken power law fit with two breaks to the Cherenkov–dominated spectrum is visualized in Fig. 3.28. Relevant parameters are given in Tab. 3.5.

In the case of energy spectrum derived from Cherenkov–dominated data, the change of spectral index in the lowest energy bins is highly uncertain. For this reason, the broken power law fit starts at $10^{15.7}$ eV. Note that the broken power law fit of the TALE energy spectrum [54], measured with a very similar technique, that starts also at $10^{15.7}$ eV can be directly compared with the Auger Cherenkov results. It should be pointed out that, although the χ^2 probability of the broken power law fit is $p_{\chi^2} \approx 0.66$, even better description is obtained by fitting the spectrum by the function introduced in Eq. (3.14), see Fig 3.7 with $p_{\chi^2} \approx 0.95$. But the parameters of the spectral function given in Eq. (3.14) can not be, in general, directly compared with parameters of broken power law summarized in Tab. 3.5. Systematic uncertainties listed in Tab. 3.5 are estimated by fitting the spectra obtained by different systematic shifts, see Fig. 3.22, and summing the residuals of parameters in quadrature.

To perform the spectrum fits, a χ^2 minimization with the use of Eq. 3.15 is adopted. Although other methods based on maximum likelihood fits exist as well, differences in fitted spectral features are below the statistical uncertainties of the fitted parameters as described in Ref. [78]. The largest uncertainty with respect to the used fitted procedure is associated with the flux normalization J_0. It can be demonstrated by attributing central energies of the bins, rather than the center of the logarithm of energies, to the measured J_i. This choice is not standard but may represent the energy E_i attributed to the bin as well. If the fit is performed for such a shift in energy, the normalization turns out to be $J_0^+ = (1.026 \pm 0.007) \times 10^{-10}$ km^{-2} sr^{-1} yr^{-1} eV^{-1}, i.e. it is shifted by $\approx +2\%$ with respect to J_0. Another possibility is to shift E_i to the average energies observed in bins. Due to the steeply falling flux, this energy is lower than the center of the logarithm of energies. In this case, the normalization reads $J_0^- = (0.983 \pm 0.006) \times 10^{-10}$ km^{-2} sr^{-1} yr^{-1} eV^{-1}, i.e. is shifted by about -2% with respect to J_0. Nevertheless, the most important result of these checks is that the spectral indices are unchanged and positions of breaks are shifted by only about 10% of the statistical uncertainties of their fitted values.

Two breaks connected by straight lines are easily identified on the spectral curve at low energies, see Fig. 3.28. It is worth emphasizing that the break at

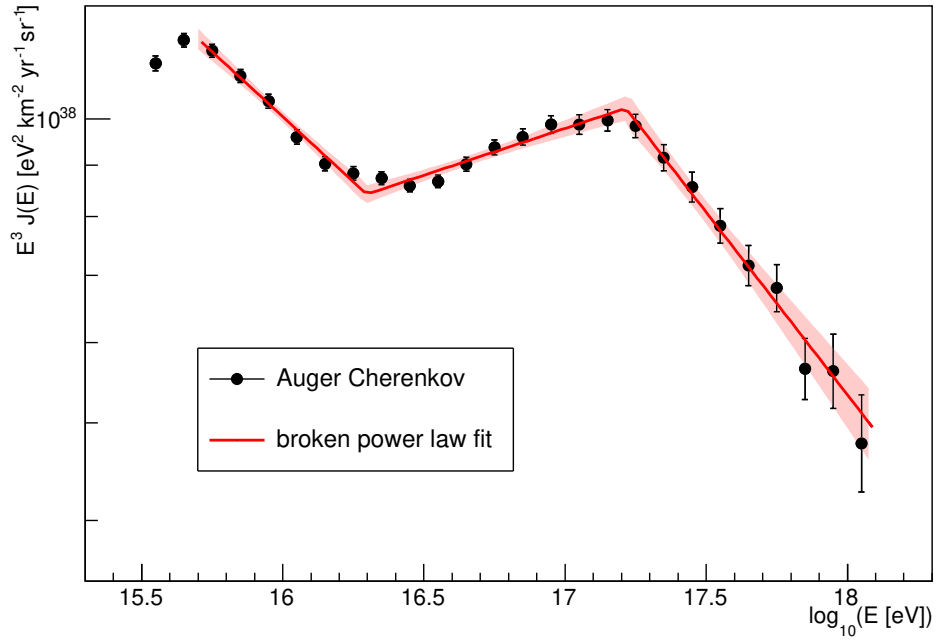

Figure 3.28: Broken power law fit of the Cherenkov–dominated spectrum. Fitted parameters are listed in Tab. 3.5. The red area denotes the region at 95% confidence level around the fitted function. χ^2 probability of the fit is $p_{\chi^2} \approx 0.66$.

Table 3.5: Parameters of the broken power law fit to the Cherenkov–dominated energy spectrum shown in Fig. 3.28. Statistical together with systematic uncertainties are quoted. χ^2 probability of the fit is $p_{\chi^2} \approx 0.66$.

Parameter	Value $\pm$ $\sigma_{\text{stat.}}$ $\pm$ $\sigma_{\text{syst.}}$
J_0 [km^{-2} sr^{-1} yr^{-1} eV^{-1}]	$(1.005 \pm 0.006 \pm 0.4) \times 10^{-10}$
$\log_{10}(E_1$ [eV])	$16.30 \pm 0.02 \pm 0.3$
$\log_{10}(E_2$ [eV])	$17.22 \pm 0.03 \pm 0.2$
γ_1	$3.26 \pm 0.02 \pm 0.2$
γ_2	$2.91 \pm 0.01 \pm 0.06$
γ_3	$3.36 \pm 0.03 \pm 0.2$

$E_2 = 10^{17.22}$ eV named the 2$^{\text{nd}}$ Knee is observed at the Pierre Auger Observatory for the first time.

Conclusion

The low–energy spectrum of cosmic rays in the energy region of $10^{15.5} - 10^{18.1}$ eV was presented. To infer it from the Cherenkov–dominated data measured at the Pierre Auger Observatory, the profile constrained geometry fit technique of the extensive air shower reconstruction was implemented in the Observatory software. Exposure of the fluorescence detector was estimated with the use of Monte Carlo simulations. Unfolding of the detector effects propagating to the energy spectrum measurement was performed by the forward folding method. To be used in the energy spectrum analysis, the invisible energy model was derived utilizing the IceTop data at energies between $10^{15} - 10^{17}$ eV.

Above 10^{17} eV, the invisible energy model is connected to the Pierre Auger Observatory estimates. The invisible energy ranges from about 27% of the total energy at the lowest measured energies to less than 14% at the highest energy part. Derived systematic uncertainties in the invisible energy are about 15% of its value in the energy range probed by the Cherenkov–dominated data.

The exposure for the data taken in the period of 06/2012–12/2017 ranges from 3×10^{-3} km^2 sr yr up to 9.5 km^2 sr yr at energies of $10^{15.5}$ eV and $10^{18.1}$ eV, respectively. The strong energy dependence is caused by increasing aperture of the fluorescence telescopes with energy as the amount of light produced by extensive air showers increase.

The forward folding method is a variation of the bin–by–bin correction unfolding widely used at the Pierre Auger Observatory. The correction itself is not large and accounts at most 10% and 5% of the raw flux at energies below and above 10^{16} eV, respectively. This is achieved by using the reconstruction method providing energy biases lower than 5% and reconstruction resolution about 20% of energy.

The all-particle energy spectrum in the low–energy region exhibits two pronounced features, a hardening from the spectral index $\gamma_1 \approx 3.3$ to $\gamma_2 \approx 2.9$ at about $10^{16.3}$ eV and then a softening to $\gamma_3 \approx 3.4$ around $10^{17.2}$ eV. The detection of these spectral features completes the measurement of the flux of cosmic rays above the Knee region ($\approx 10^{15.5}$ eV) at the Pierre Auger Observatory. The flux determination above $10^{15.5}$ eV is demonstrated by the combined spectrum of all up–to–date energy spectrum estimates performed at the Observatory. The results are compatible within systematic uncertainties with measurements of other experiments, although systematic discrepancies occur.

Systematic uncertainties of the measurement are dominated by the energy scale uncertainty and the uncertainty in exposure at the highest and lowest energies, respectively. The total uncertainties evolve with energy and read from 30% to 60% of the measured flux. The dominating factor is the uncertainty in the absolute calibration of fluorescence telescopes which accounts for 9.9% of energy and is common to all measurements done at the Pierre Auger Observatory.

Appendices

Technical details about the Cherenkov spectrum analysis are given in the following appendices. They summarize mainly the results of the Author's technical work done within the Pierre Auger Collaboration and provide further cross–checks and explanations of methods used in the spectrum analysis.

Appendix A focuses on the description of the Cherenkov light emission. It is based of Refs. [A9, A10, A16]. In Appendix B, details about the Real–MC simulations of the Cherenkov dominated data are provided [A11, A12, A15, A17]. Validity of the Real–MC simulations is cross–checked in Appendix D. Accuracy of the shower reconstruction method is investigated in Appendix C and its technical implementation in the Auger $\overline{\text{Off}}\underline{\text{line}}$ software is described in Appendix E.

A. Cherenkov emission model vs. CORSIKA simulations

As described in Section 2.2.2, the model of Cherenkov light emission in Auger Offline software is based on Ref. [36]. Parametrizations of the light emission in Ref. [36] were done with the use of CORSIKA MC simulations at energies above 10^{17} eV. Usage of this model in reconstructions of showers at lower energies deserves a cross–check. Another simplification in the Offline description of the direct Cherenkov light is in the usage of the same lateral light distribution as the one derived for the fluorescence emission [79].

To check the Cherenkov emission model, a set of CORSIKA MC simulations was prepared within the Pierre Auger Collaboration [80]. Special settings allowing a direct export of the CORSIKA generated Cherenkov photons into Offline were used

- `CHERENKOV`,
- `SLANT`[1)],
- `ECUT` for EM particles of `20 MeV`,
- `TELESCOPE` placed at the HEAT position, see Fig. 1.8.

The energy range of these simulations is $10^{15} - 10^{17}$ eV. The `TELESCOPE` option allows to store all Cherenkov photons reaching the telescope placed at a given position. Thus, realistically simulated optical images of EASs are used to test the Cherenkov emission model. Moreover, the absolute Cherenkov yield and the angular distribution of emitted Cherenkov photons are predicted independently from the Offline models. It is important to note that CORSIKA tracks each particle generated in the EAS and realistically produces Cherenkov photons emitted by charged particles.

These simulations have been processed by the Author in the following steps.

In the first step, the CORSIKA simulations have been reconstructed by the standard reconstruction procedure in Offline with a fixed true MC shower axis. Results are shown in blue in Fig. A.1 where the average reconstruction bias in $E_{\rm cal}$ (left panel) and the distribution of $E_{\rm cal}$ residuals (right panel) are shown. A significant trend in the $E_{\rm cal}$ bias is present. The bias changes by almost 20% in energy over the investigated energy range.

In the second step, the individual Cherenkov photons generated in CORSIKA that reach the telescope have been processed. Using their arrival times, incident directions, and emission points, an overall correction to the angular distributions of emitted photons shown in Fig. 2.4 has been calculated. It is depicted in Fig. A.2 and accounts up to 60% of the original value at viewing angles around 30° where the fluorescence light starts to dominate. The viewing angle is the angle between the shower axis and the line that connects a point on the shower axis and the telescope.

[1)] Due to this option, the simulated energy deposit $E_{\rm cal-MC}$ is summed according to Ref. [A18].

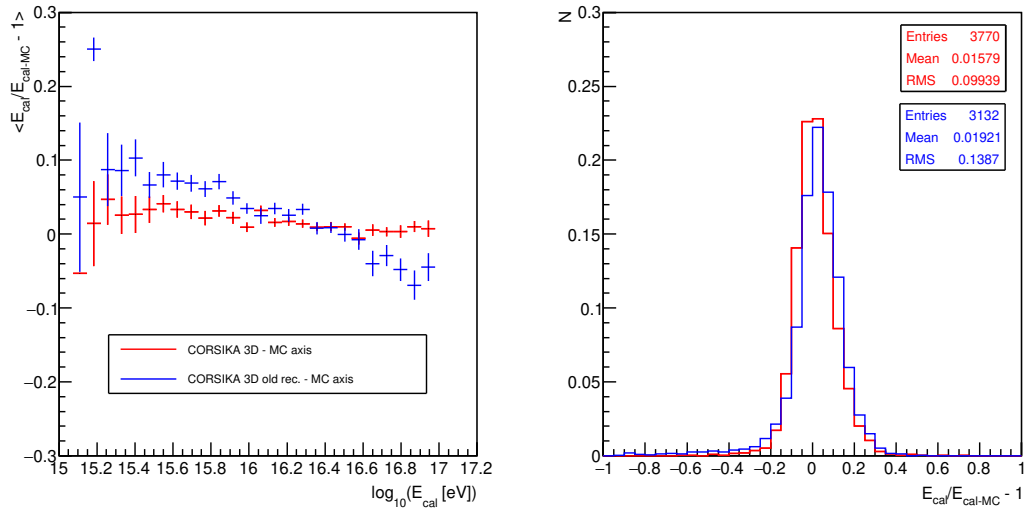

Figure A.1: Offline reconstructions of showers generated in CORSIKA using fixed true MC shower axis. Reconstructions with the uncorrected Cherenkov emission model (blue) and with the corrected one (red) are shown. Average biases in $E_{\rm cal}$ are shown in the left panel and the distributions of $E_{\rm cal}$ residuals are shown in the right panel.

Another correction that is deduced from the CORSIKA simulations is the correction to the lateral light distribution originally derived for the fluorescence light [79]. This correction is implemented at the level of quantiles of cumulative distribution functions (CDFs) of lateral light provided by the model in Ref. [79] which includes a dependence on the shower age defined by Eq. (2.6). Such CDFs are derived for showers generated in CORSIKA directly from distributions of detected photons. Example of the correction function is shown in Fig A.3 for the viewing angle bin of $10^\circ - 11^\circ$. These correction functions are calculated and applied independently for different viewing angles.

After both above mentioned corrections are applied in the reconstruction, the energy bias is highly reduced, see the red points and the distribution in Fig. A.1. It is worth mentioning that the corrections are not tuned in any way to minimize the energy reconstruction bias. The improvement is only a consequence of more precise description of the direct Cherenkov light emission by the corrected model. The persisting residual bias of up to 3% in energy assign the systematic uncertainty in energy determination due to the Cherenkov emission model listed in Tab. 3.3.

With the use of the corrected model of the direct Cherenkov light emission, the CORSIKA showers have been reconstructed again using the shower axis determined by the PCGF. The results are given in magenta in Fig. A.4. Another discrepancy in the reconstructed $E_{\rm cal}$ is documented. This discrepancy is caused by an improper assignment of the emission point to the time of detection in the time fit described in Section 2.4. An effect of the direct Cherenkov light emission on the time fit is sketched in Fig. A.5. To a first approximation, only the light emitted closer to the telescope than the shower axis is detected. The perpendicular distance between the shower axis and the point of Cherenkov photon emission

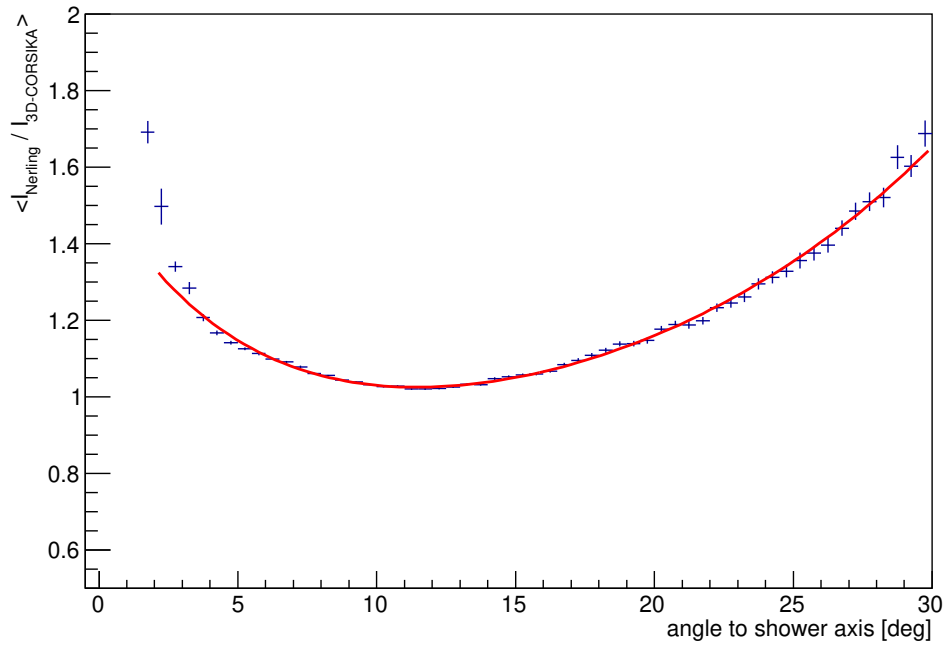

Figure A.2: Overall correction to the angular distributions of emitted photons shown in Fig. 2.4. I_{Nerling} stands for the direct Cherenkov light flux at observer normalized to 1 charged particle estimated with the use of the Nerling's [36] parametrization implemented in Offline. $I_{\mathrm{3D-CORSIKA}}$ denotes the same quantity simulated by CORSIKA. Average over many showers is shown. Red line is the correction newly implemented in Offline.

is denoted as R. Its value depends mainly on the lateral width of the EAS. The D parameter represents the distance between the local shower core in the atmosphere and the emission point of Cherenkov photons perpendicularly projected on the shower axis. This parameter is connected to the shower front curvature and can be extracted from simulations with the use of known shower geometry and known emission points of Cherenkov photons. The distributions of average D and R over many showers are shown in Figs. A.6 and A.7, respectively. The D distance is evaluated directly in meters and produce, after the division by c, ≈ 20 ns correction to the t_0 parameter, see Eq. (2.10). The R parameter is evaluated with respect to the 90% quantile of the lateral width distribution of particles from Ref. [79] which is parametrized in Molière radius of air, R_{M}, at given height above sea level[2)]. The average values coming from the distributions in Figs. A.5 and A.7 are used in the time fit of the PCGF reconstruction as corrections to R_{p} and t_0, respectively.

It is important to note that in the case of fluorescence–dominated events these corrections can be omitted. The D parameter causes only a marginal difference in the shower position on the camera, because a typical duration of the fluorescence–dominated event is about 10-100 μs in contrast to a few hundreds of ns in the

[2)] Thus, the 90% quantile can be thought of as a local Molière radius belonging to the hadron–initiated air showers.

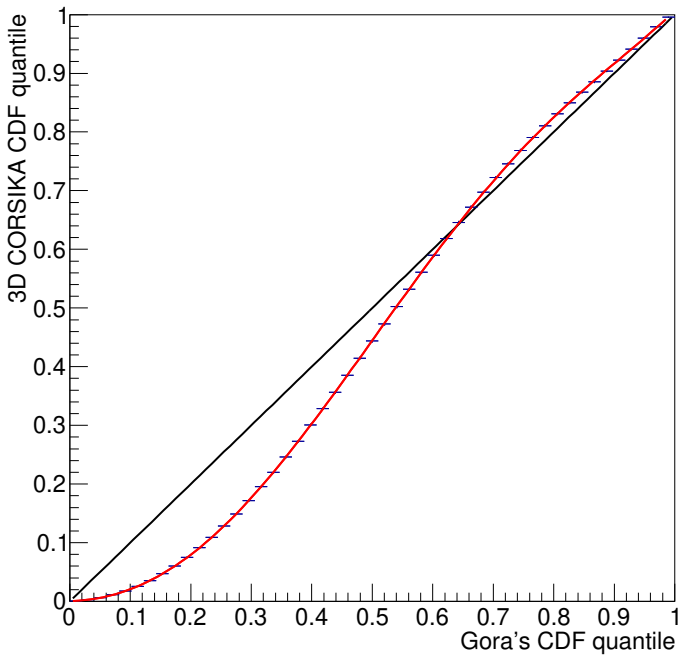

Figure A.3: Correction to the cumulative distribution function of the direct Cherenkov lateral light in a form of quantile–quantile plot. The x axis shows quantiles of CDF calculated with the use of Ref. [79] and y axis gives CDF quantiles calculated directly from the distributions of Cherenkov photons simulated in CORSIKA. Blue points denote the values calculated from simulations and the red line is a parametrization implemented in $\overline{\text{Off}}\underline{\text{line}}$ in the corrected model of direct Cherenkov lateral light. The black line shows an identity line.

case of Cherenkov–dominated events. Because the fluorescence light is emitted isotropically, the light is detected from all around the shower axis which smears the effect of R distance. Moreover, the fluorescence–dominated events are seen, on average, from larger distances and large viewing angles which further suppress the impact of R.

Results of the energy reconstruction after the time fit corrections are applied are shown in Fig. A.4 by green color.

All corrections described herein are used in the reconstruction of really detected events. However, in the case of reconstruction of Real–MC generated showers, the corrections are limited to the one connected to the angular distribution of emitted Cherenkov photons shown in Fig. A.2. This is the only correction that can be easily implemented in the simulations based on the fast CONEX software used for the Real–MC generation, see Appendix B. Thus, only this correction is relevant for the Real–MC reconstruction.

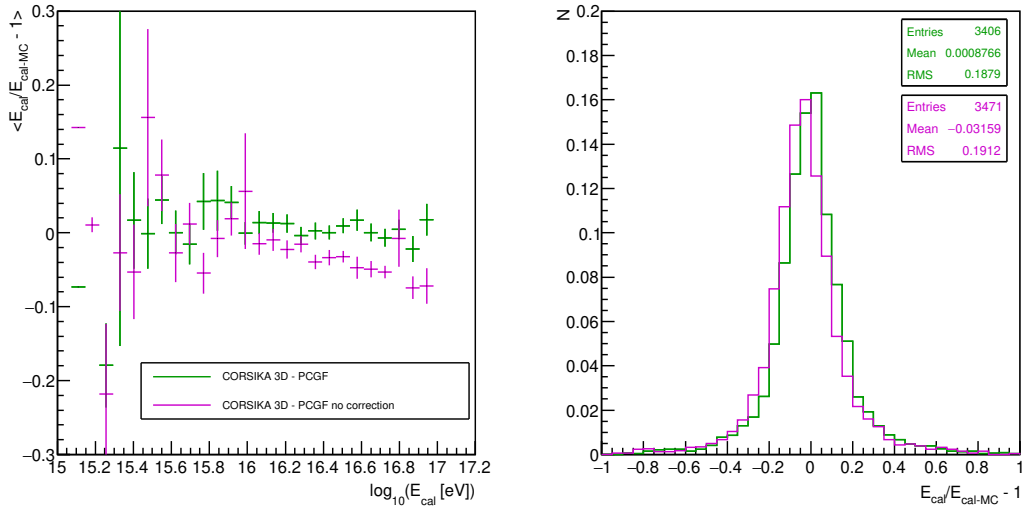

Figure A.4: Offline reconstructions of showers generated in CORSIKA with the shower axis determined by the PCGF. The results obtained with and without the time fit correction are shown in green and magenta, respectively.

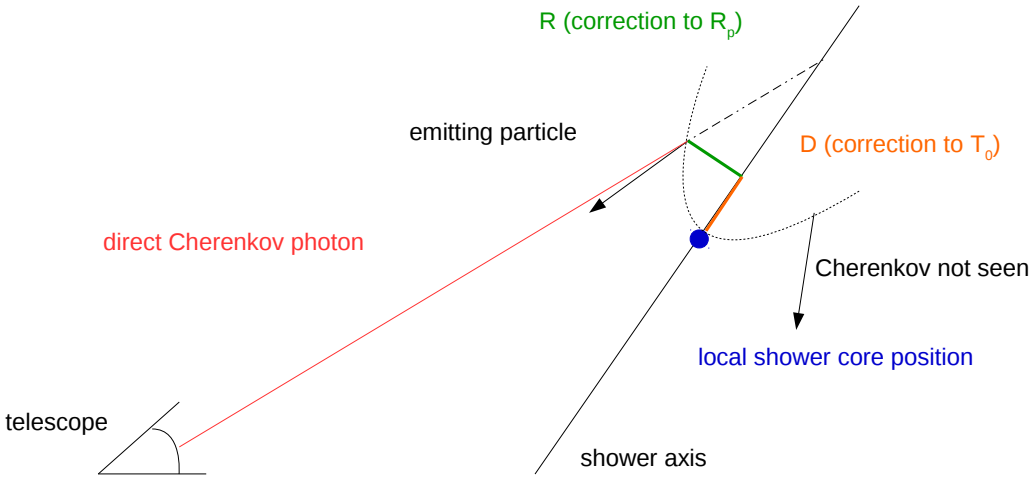

Figure A.5: Sketch of the direct Cherenkov light emission from EASs. Direct Cherenkov photons (red) are emitted around the direction of movement of charged particles (black arrows). The point of emission is not placed exactly on the shower axis, rather its perpendicular distance to the shower axis, R, is shown in green. The local shower core position (blue) on the shower front (dotted line) is advanced with respect to the emitting particles. The distance between the local shower core and a perpendicular projection of the emission point on the shower axis, D, is depicted by orange color.

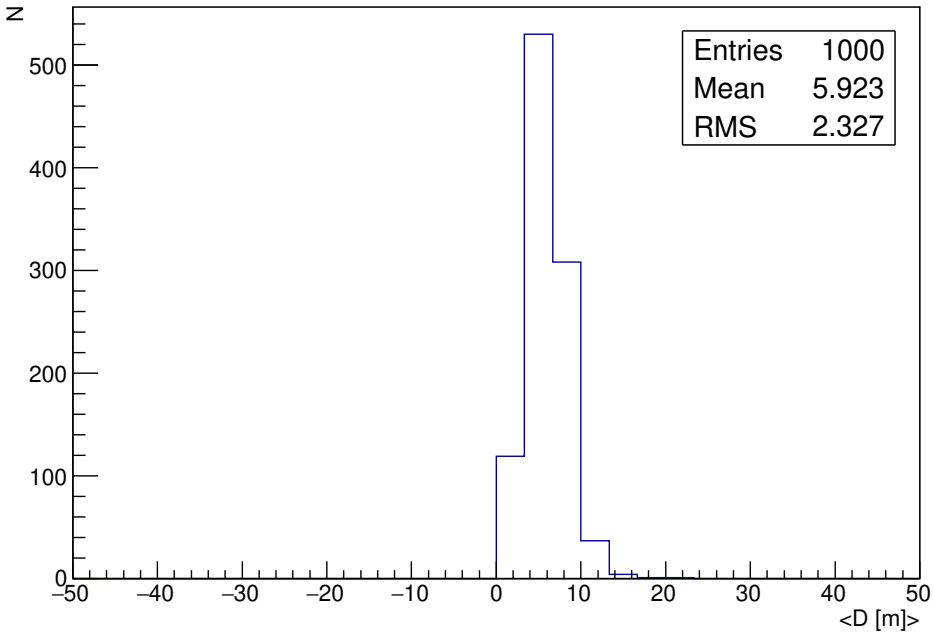

Figure A.6: Distribution of the average D parameter over many simulated showers. The mean value of this distribution is used in the PCGF as a correction to the t_0 parameter in the timing relation Eq. (2.10).

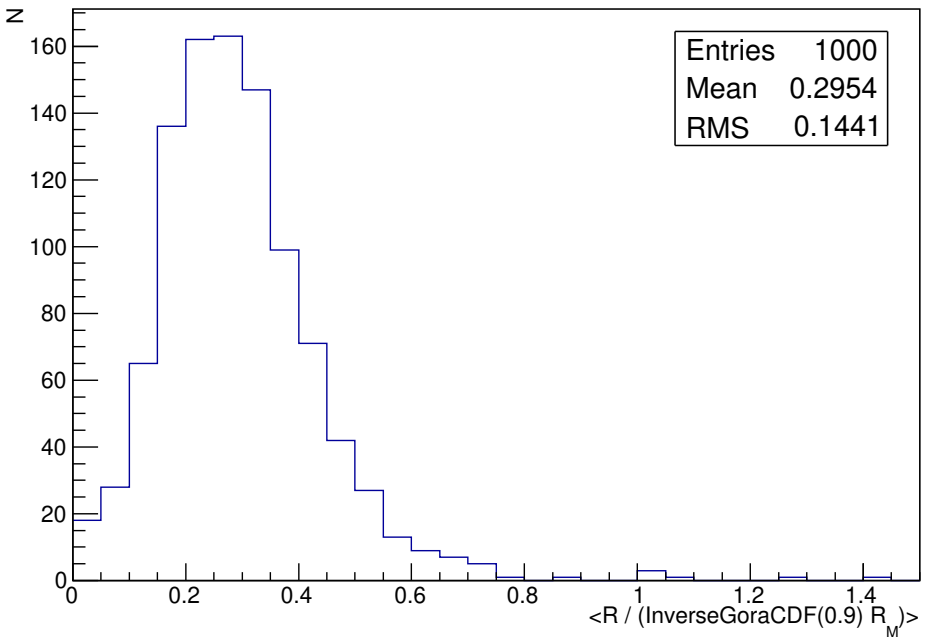

Figure A.7: Distribution of the average R parameter over many simulated showers expressed in the 90% quantile of the lateral width distribution of particles from Ref. [79]. The mean value of this distribution is used in the PCGF as a correction to the R_p parameter in the timing relation Eq. (2.10).

B. Real–MC simulations

The time dependent simulations, Real–MC, are used to mimic the status of the Pierre Auger Observaotry detectors at each particular time as realistically as possible. This approach is utilized to determine the exposure of the HEAT and Coihueco FD telescopes, see Fig. 1.8, in the time period of 06/2012–12/2017 which corresponds to the data set described in Section 3.2.

To study the exposure, showers generated by CONEX [8] with Sybill 2.3c as a high–energy interaction model [81] are used. The energy range of the simulations is $10^{15.3} - 10^{18.2}$ eV, slightly larger than the energy range of the measurement, chosen in order to account for possible bin–to–bin migrations during the unfolding procedure described in Section 3.4. The spectral index of 1.2 is used to make it possible to produce enough MC statistics at high energies. Protons and iron nuclei have been used as primaries to produce two MC sets consisting of 100M of thrown showers each.

The extremely high number of simulated events is dictated by the detector acceptance that is strongly dependent on the shower geometry. To estimate the boundaries of the simulation region, the first set of isotropic simulations with large generation area of 28.2 km was produced. Above this distance, only 1% of would be triggering events at the highest investigated energies is lost. Moreover, they would trigger solely by the fluorescence light and would be cut in the analysis. Then, for each energy bin, the TLT trigger probability is calculated and a viewing angle between the shower axis and the X_{max}–telescope conjunction line is extracted. The maximum accepted viewing angle corresponds to the 10^{-5} trigger probability, see Fig. B.1 for the energy bin of $10^{16.4} - 10^{16.6}$ eV and radial distances of the shower core on the ground $R = 4-5$ km from the HEAT position. The cut level of 10^{-5} is chosen to assure that less than 1% of TLT triggering events is lost in each energy bin across the whole investigated energy range. The complete set of maximum accepted viewing angles is shown in Fig. B.2. This set defines the maximum accepted viewing angles for the final Real–MC simulations. Without this simplification, the amount of necessary computation time would be unmanageable.

In the final simulations, the events are thrown equally inside the circle S centred at the position of the HEAT. The radius of S is restricted independently in each energy bin to the maximum distance with non–zero maximum accepted viewing angle. This fact effectively introduces different normalizations of generated fluxes in each energy bin. All connected effects are corrected for in the final weighting of simulated events to the E^{-3} energy spectrum performed in the analysis. Zenith angles ϑ are chosen such that an isotropic flux on the circle S is produced

$$\frac{\mathrm{d}N}{\mathrm{d}\cos\vartheta} \propto \cos\vartheta. \tag{B.1}$$

The zenith angle range is restricted to $0° - 90°$. Azimuth angles are thrown equally in the range of $0° - 360°$. Events that do not fulfil the maximum viewing angle condition are skipped.

The shower light is simulated inside the $\overline{\mathrm{Off}}\underline{\mathrm{line}}$ framework in the standard way [34]. The improved angular distribution of the direct Cherenkov light emission, described in Appendix A, as well as a more precise formula for the refractive

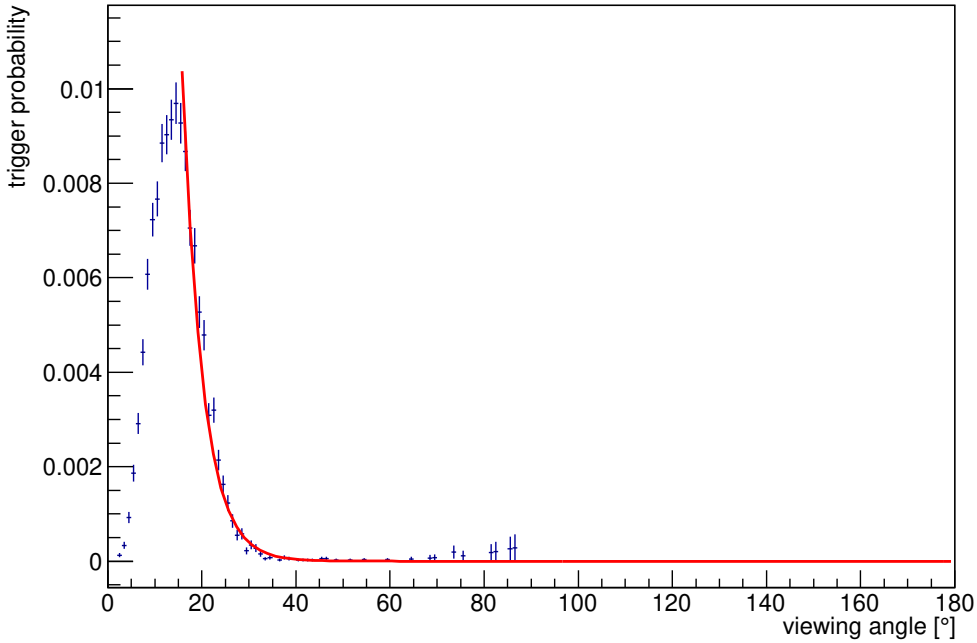

Figure B.1: TLT trigger probability for the energy bin of $10^{16.4} - 10^{16.6}$ eV and radial distances of $4 - 5$ km from the HEAT. Determination of the maximum allowed viewing angle between the shower axis and the $X_{\max}$–telescope conjunction line is visualized. The red line corresponds to the exponential fit of the tail of the distribution. The cut value is placed at the 10^{-5} level of the trigger probability.

index of air depending on the pressure, temperature, and the wavelength of the emitted light are used [A17]. The simulation of response of the FD telescopes is time dependent [63] and the SD response is completely neglected. The SD response can be omitted because only FD data are used. Thus, the CDAS veto is ignored in the Real–MC simulations to assure the same detection settings as used for the FDAS data.

The reconstruction of events is done in the standard way [35], except for changes as follows:

- `FdProfileConstrainedGeometryFitPG` module, see Appendix E, is used to determine the shower axis geometry
- `FdSDPFinder` – minimum number of pixels in SDP = 4 instead of 5
- `FdEnergyDepositFinderKG` – anti–aliasing filter correction is applied [A15] and the improved profile fit with the minimum dimension of the CFM of 200×200 bins is used [A16]

The Detector status selection cuts applied both to the Real–MC and the data sets are (`standard` cuts are available in the ADST package):

- `!isCLF`
- `!isXLF`

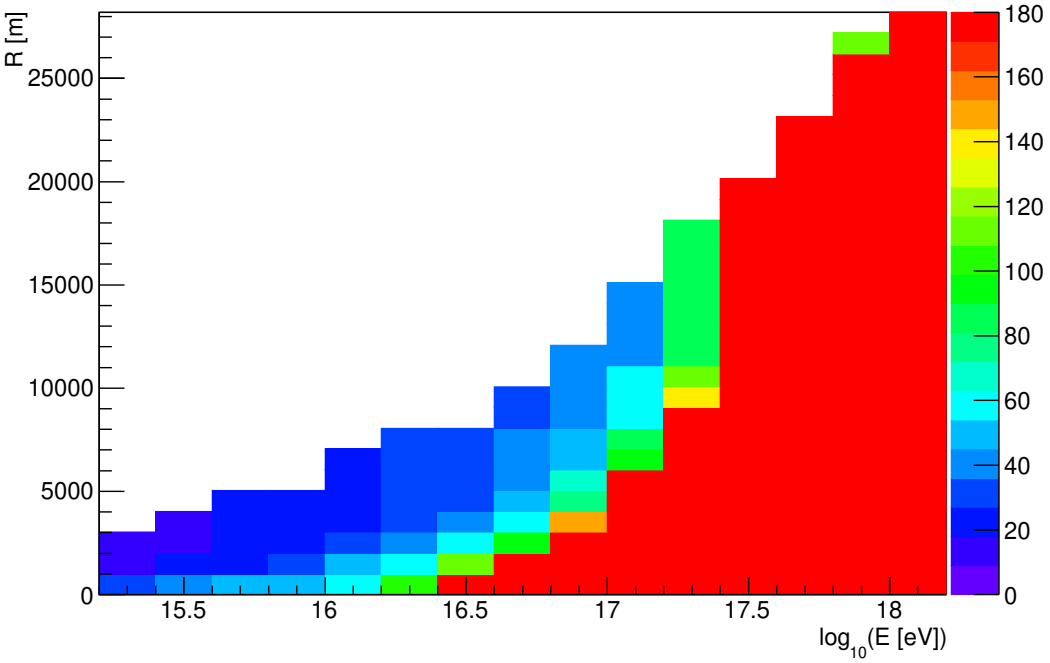

Figure B.2: Maximum accepted viewing angles extracted from the TLT trigger probability binned in the logarithm of energy, E, and in the radial distance between the shower core on the ground and the HEAT position, R.

- `heatOrientationUp`
- `HEATdownCampaignFile` – a special cut for the Real–MC to select only those events that occured during the time periods when HEAT operated in the upward mode
- `badFdPeriodRejection`
- `skipSaturated`
- `noBadPixelsIsInPulse`
- `good10MHzCorrection`
- `hasMieDatabase`
- `maxVAOD 0.1`
- `cloudCutXmaxPRD14 { params:  1 nMinusOne:  21 -10.5 10.5 }`
- `milLgEcalFD 1e-20`
- `RejectFDASVetoPeriods 111000 4`
- hottest mirror $\neq 9$ – to exclude events occurring in the HEAT telescope No. 3 due to calibration problems

- hottest mirror $\neq 6$ for GPS time $> 113 \times 10^7$ s (27 October 2015) – to exclude events occurring in the Coihueco telescope No. 6 in the period of data loss caused by technical problems not reflected by the Real–MC

On top of the Detector status cuts listed above also the Quality cuts are used:

- X_{max} observed
- $\mathrm{GH}(0\ \mathrm{g\ cm^{-2}}) < 0.05 \left(\frac{\mathrm{d}E}{\mathrm{d}X}\right)_{\mathrm{max}}$ – to exclude miss–reconstructed events with unphysical longitudinal profiles
- $R_{\mathrm{p}} < \overline{R_{\mathrm{p}}}$ – fiducial volume cut defined in Eq. (3.20)
- $VA_{\mathrm{Xmax}} < \overline{VA}_{\mathrm{Xmax}}$ – fiducial volume cut defined in Eq. (3.21)
- $30^\circ < \chi_0 < 165^\circ$
- 500 m$< R_{\mathrm{p}} <$ 5000 m
- t_0 error $<$ 35 ns
- R_{p} error $<$ 100 m
- χ_0 error $< 6^\circ$

The last five cuts are defined in a way that they cut events with average biases in the reconstructed energy larger than 15% of the true MC energy.

Besides the Real–MC set used for the exposure calculation, the extended Real–MC set is defined. The extended set is composed of Real–MC simulations that are not cut by the Detector status cuts but with the Quality cuts applied. The only Detector status cut which is applied is the `skipSaturated` cut which excludes events with saturated pixels. Such events occur also in simulations and substantially affect the reconstruction precision. The last two of the Detector status cuts are reflected in the extended set by appropriate weights attributed to events occurring in corresponding FD telescopes. This procedure helps to increase the statistics of simulations while not affecting the reconstruction precision. The extended Real–MC set is used to test the reconstruction performance and calculate relative differences in exposure. But it can not be used for the exposure calculation itself where the absolute normalization is crucial.

Validity of the Real–MC simulations is cross–checked with reconstructed parameters taken from the data set in Appendix D.

C. Accuracy of the PCGF method

Accuracy of the PCGF method of the shower axis determination is investigated with the use of the extended Real–MC set defined in Appendix B. Selected outputs of the reconstruction which are checked are the total reconstructed energy $E_{\rm rec}$, pointing direction of the shower axis, shower axis parameters $R_{\rm p}$, χ_0, t_0, see Eq. (2.10), and the shower core position on the ground[1)].

Average bias in $E_{\rm rec}$ as a function of logarithm of energy is shown in Fig. C.1. Maximum obtained value is about 5% of the true MC energy which corresponds to the 2.5% uncertainty in the FD energy bias listed in Tab. 3.3. Distributions of differences between the reconstructed $\log_{10}(E_{\rm rec}[{\rm eV}])$ and the true MC values $\log_{10}(E_{\rm MC}[{\rm eV}])$ of the logarithm of energy are depicted for four energy intervals that are marked in the insets in Fig. C.2. In all accuracy plots, as well as in the whole analysis of the energy spectrum, the MC events are weighted according to E^{-3} which roughly resembles the observed flux. On top of that, the mixture of protons and iron nuclei corresponding to $\langle \ln A \rangle$ from the global spline fit model is used, see Fig. 1.7.

Similar plots as for $E_{\rm rec}$ are shown in Figs. C.3–C.8 for the $R_{\rm p}$, χ_0, and t_0 parameters of the shower axis. In the distributions corresponding to the two higher energy intervals, the tails are present for minority of events, notice the logarithmic scale in the plots. These tails are responsible for larger geometry reconstruction biases at higher energies. The miss–reconstructed events are those that possess lower fraction of Cherenkov light which improves the accuracy of the PCGF reconstruction as discussed in Section 2.7. This assumption is confirmed by

[1)] In this Appendix, the ground is defined as the horizontal plane with an altitude equal to the altitude of the Coihueco building.

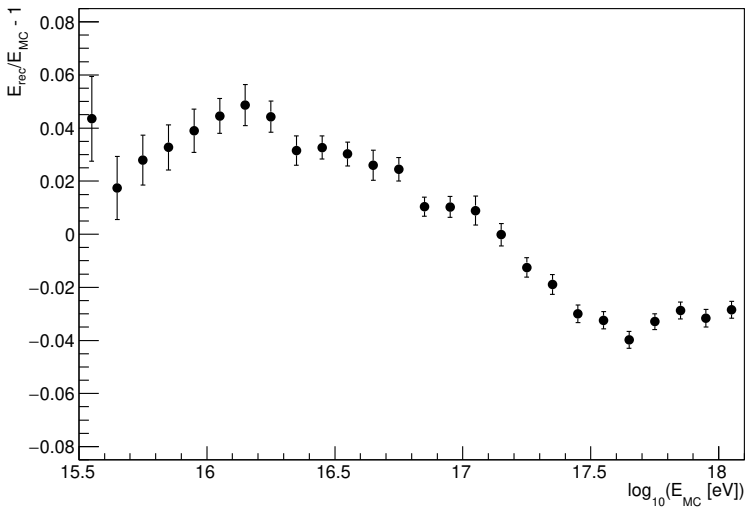

Figure C.1: Average bias in $E_{\rm rec}$ as a function of logarithm of energy.

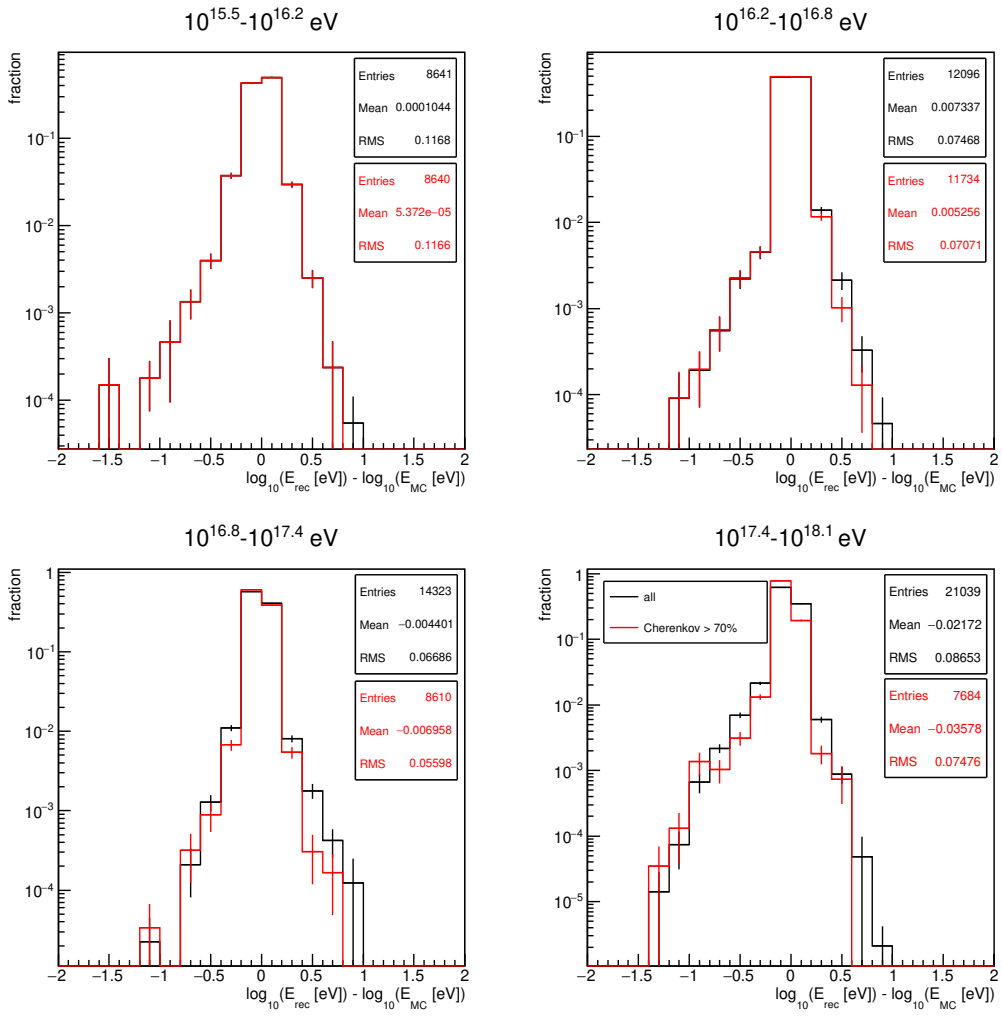

Figure C.2: Distributions of differences between the reconstructed $\log_{10}(E_{\mathrm{rec}}[\mathrm{eV}])$ and the true MC values $\log_{10}(E_{\mathrm{MC}}[\mathrm{eV}])$ of the logarithm of energy. Four energy intervals that label insets are shown. The distributions in black correspond to the selection applied in the analysis of the energy spectrum. In red, the distributions with an additional cut on the total Cherenkov light fraction above 70% are shown.

selecting only those events with the total Cherenkov fraction above 70% shown by red distributions[2)]. In this case, the tails are suppressed at a cost of important loss of events at higher energies. In principle, the Cherenkov fraction cut can be used for the energy spectrum analysis, but the improvement in the energy reconstruction is small, see Fig. C.2. For this reason, the cut on Cherenkov fraction is not applied in the analysis.

[2)] Selection is done with the use of reconstructed light profiles which means that some outliers are still present. This is caused by miss–interpreting the light fluxes in a case of too wrongly estimated shower axis.

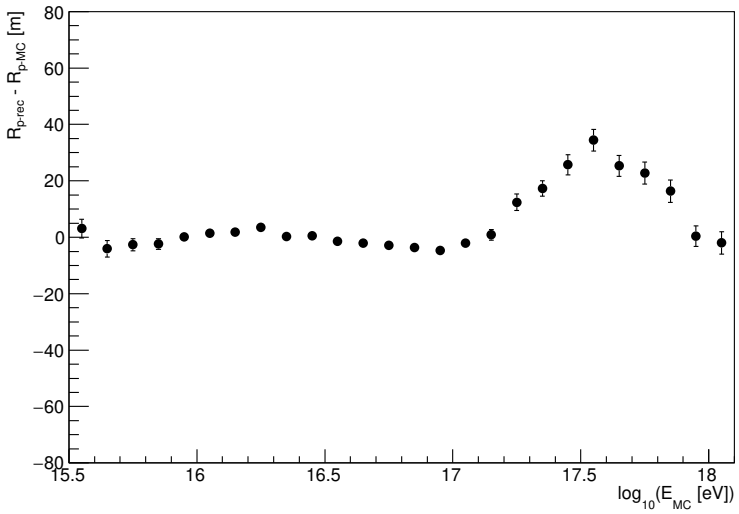

Figure C.3: Average bias in R_{p} as a function of the logarithm of energy.

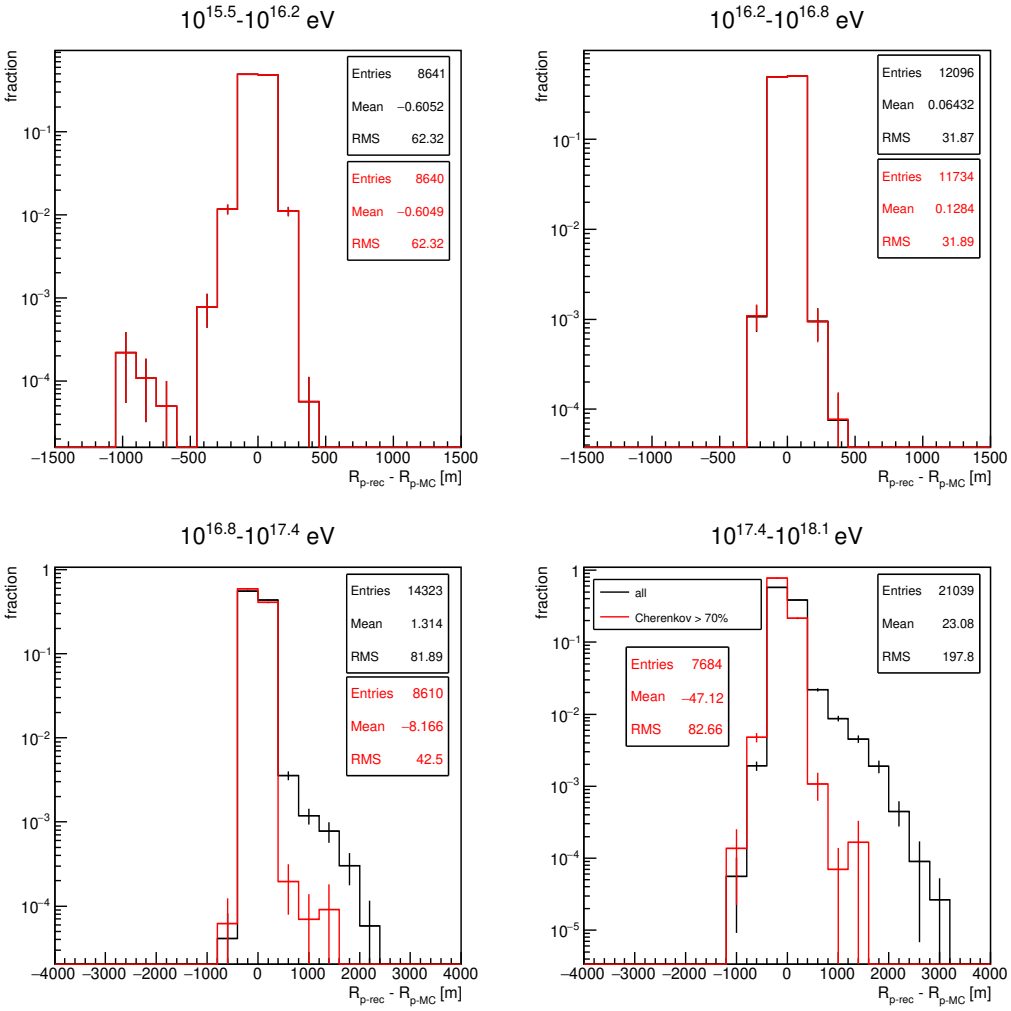

Figure C.4: Distributions of differences between the reconstructed and the true MC values of R_{p}. Color coding is explained in Fig. C.2.

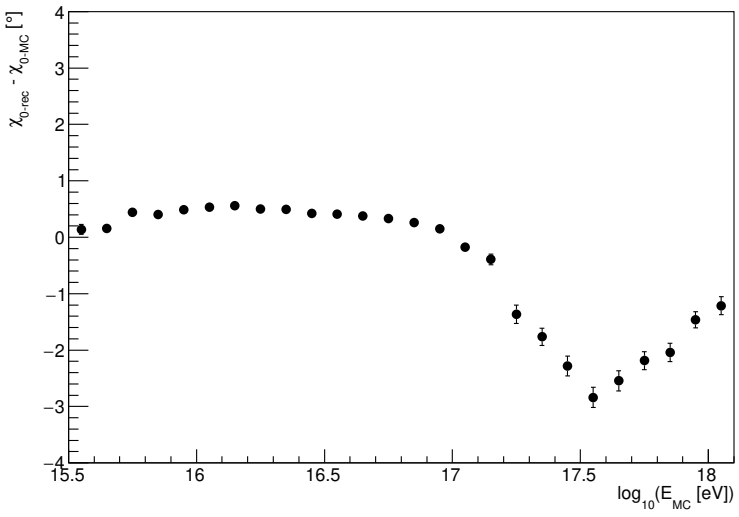

Figure C.5: Average bias in χ_0 as a function of the logarithm of energy.

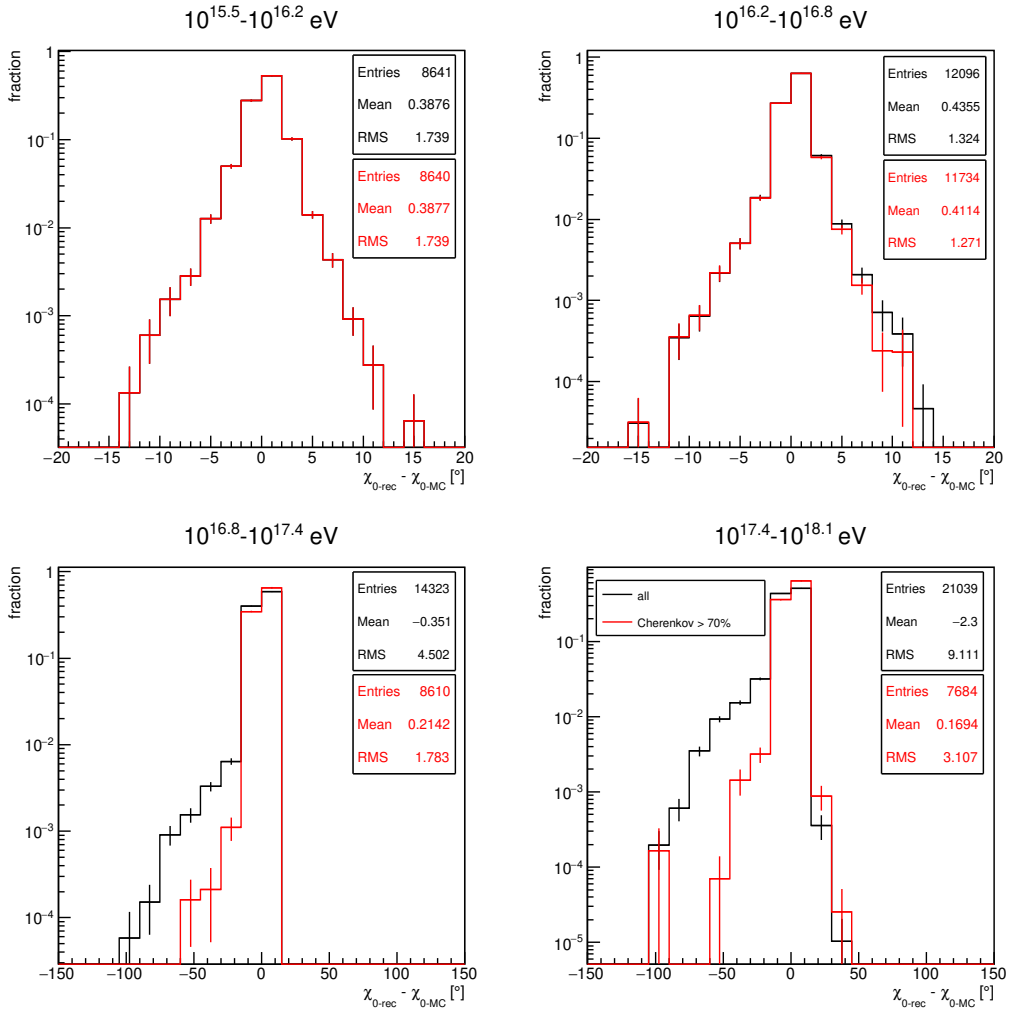

Figure C.6: Distributions of differences between the reconstructed and the true MC values of χ_0. Color coding is explained in Fig. C.2.

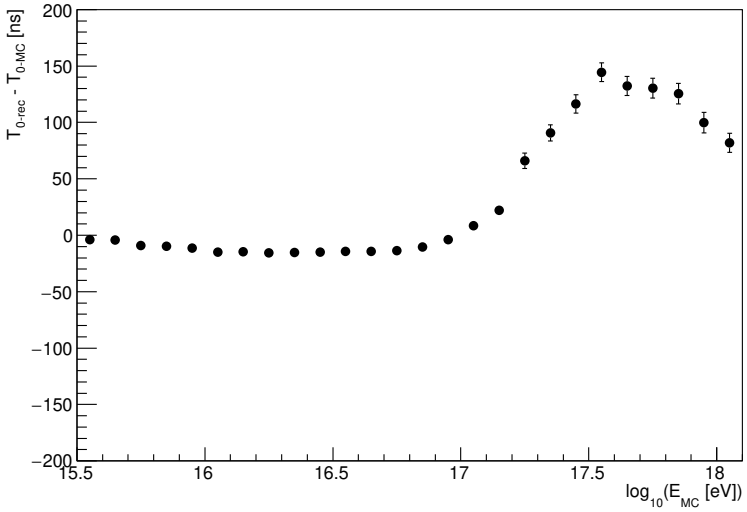

Figure C.7: Average bias in t_0 as a function of the logarithm of energy.

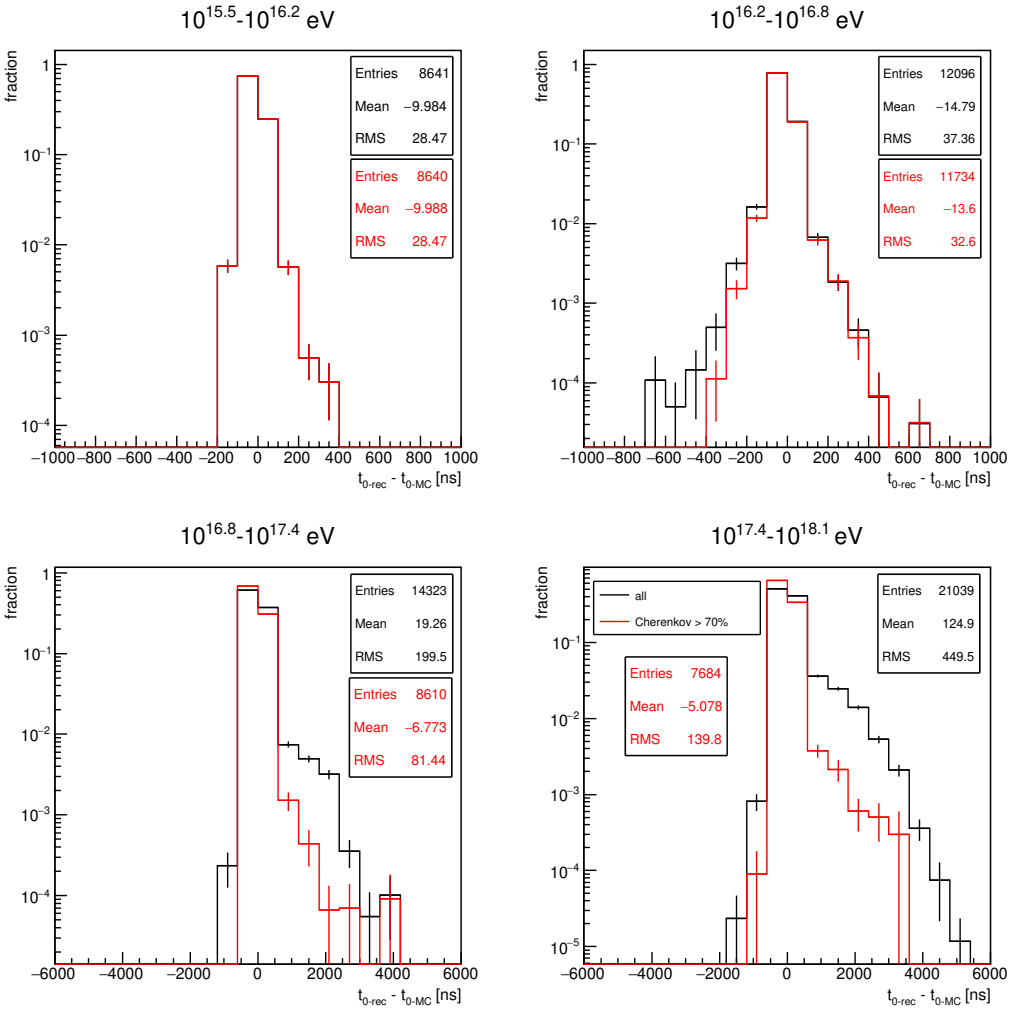

Figure C.8: Distributions of differences between the reconstructed and the true MC values of t_0. Color coding is explained in Fig. C.2.

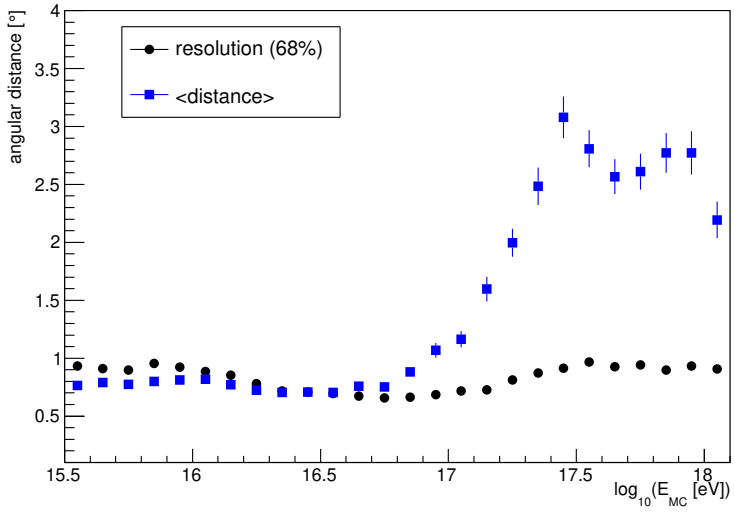

Figure C.9: Angular resolution of the PCGF reconstruction and the average angular distance between the generated and reconstructed shower axis directions are shown in black and blue, respectively. The resolution, defined as the 68% quantile of the angular deviation distribution, is less affected by reconstruction tails than the average distance value.

Nevertheless, the angular resolution of the shower axis direction is almost unaffected by the presence of tails of outliers described above. The angular resolution is defined as the 68% quantile of the distribution of angular deviations between the reconstructed and true MC directions of incident events. The angular resolution as a function of the logarithm of energy is shown in black in Fig. C.9. The resolution is better than 1° over the whole energy range. A similar quantity is the average angular distance between the reconstructed and true MC directions of the shower axis shown in blue in Fig. C.9. The average angular distance is more affected by the reconstruction tails than the resolution. The average distance is related to the average bias in χ_0 shown in Fig. C.5, thus they roughly coincide.

Distributions of differences between the reconstructed and generated shower cores (impact points of events on the ground) are depicted in Fig. C.10. The resolution of the shower core position as well as the average distance between the reconstructed and generated shower cores are shown in Fig. C.11. These quantities are defined in the same way as those for the angular distributions (except for the Cartesian rather than spherical coordinates that are used).

The last and the most important ingredient for the energy spectrum analysis that is investigated in this Appendix is the migration matrix $\mathbf{M}$. Its form directly obtained from the Real–MC simulations is shown in Fig. 3.8. $\mathbf{M}$ is closely connected to the distributions of reconstruction differences in the logarithm of energy shown in Fig. C.2. Actually, it is composed of distributions of E_{rec} binned in 0.1 in the logarithm of energy as described in Section 3.4. Example of the distribution in the E_{MC} bin of $10^{16.8} - 10^{16.9}$ eV is given in Fig. C.12.

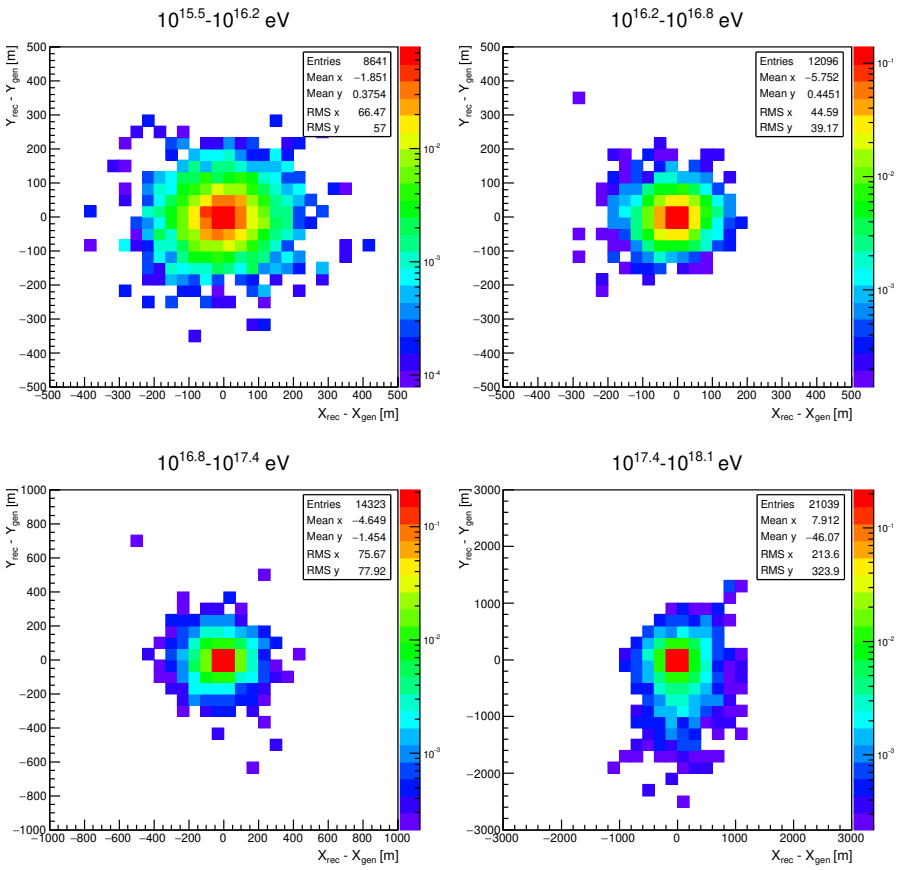

Figure C.10: Distributions of differences between the reconstructed and generated shower core positions. X and Y stand for coordinates in the Auger reference coordinated system (`SiteCS`) and are evaluated in the plane at altitude of the Coihueco building.

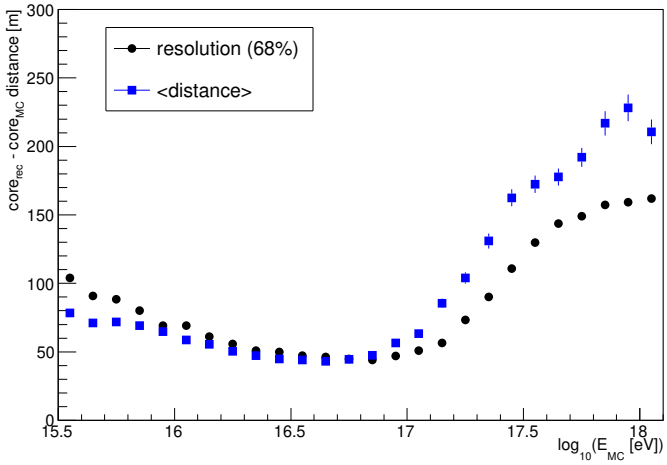

Figure C.11: Resolution of the shower core position in the PCGF reconstruction (black) and the average distance between the generated and reconstructed shower cores (blue) are depicted. Definition of the resolution is the same as in the case of angular resolution shown in Fig. C.9.

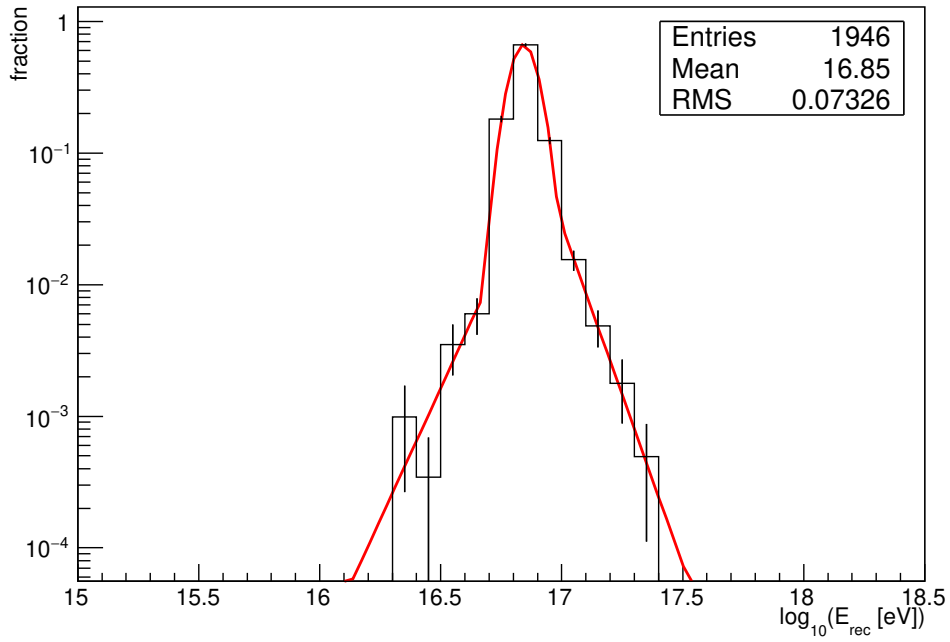

Figure C.12: Distribution of the logarithm of E_{rec} in the E_{MC} bin of $10^{16.8} - 10^{16.9}$ eV (black). Red line corresponds to the fit by Gaussian function with exponential tails.

In Fig. C.12, the red line denotes the fit by Gaussian function with exponential tails (GEF). This function is characterized by the normalization factor (n), center (μ) and standard deviation (σ) parameters of the Gaussian part, two parameters that control the point of change from the Gaussian to the exponential part, and two parameters determining the exponential decrease. To smooth $\mathbf{M}$, the GEFs are fitted to all E_{MC} bins (columns) of $\mathbf{M}$ and further processed. The Gaussian part of GEF is the most responsible for the bin–to–bin migration in a sense, that the statistical fluctuations in the unfolding corrections are diminished if Gaussian parameters are smoothed. The n, μ, and σ parameters of GEF coming from the bin–by–bin fits are shown in Figs. C.13, C.14, and C.15, respectively. In these figures, the red lines represent fits of the parameters. In the case of n and σ, the fits are performed with the logistic function. Residuals of μ from the center of the logarithmic E_{MC} bin depicted in Fig. C.14 are fitted by the conjunction of two 2^{nd} order polynomial functions. These fits are used to smooth n, μ, and σ parameters of GEFs which are then used to fill $\mathbf{M}$. The last correction is, that the normalization in each E_{MC} bin is adjusted in a way that the integral of the smoothed GEF function in the energy range of $10^{15} - 10^{18.5}$ eV matches exactly the fraction of events observed in the same energy range in the non–smoothed matrix.

The σ parameter defines the resolution of the energy reconstruction. The value of ± 0.08 in the logarithm of energy corresponds to $+20\%$ and -17% of the energy in linear scale.

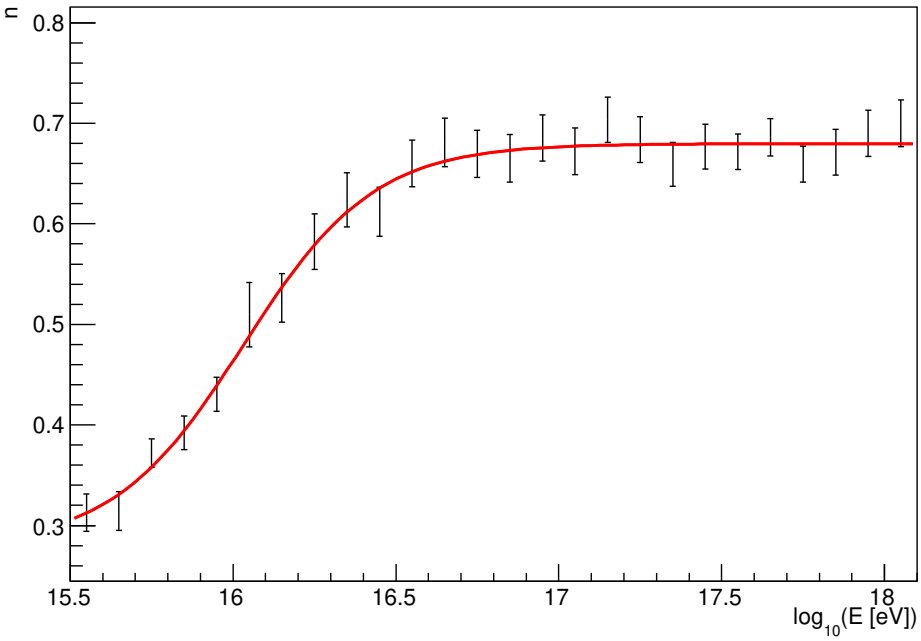

Figure C.13: The n parameter used in the smoothing of the migration matrix as a function of the logarithm of energy.

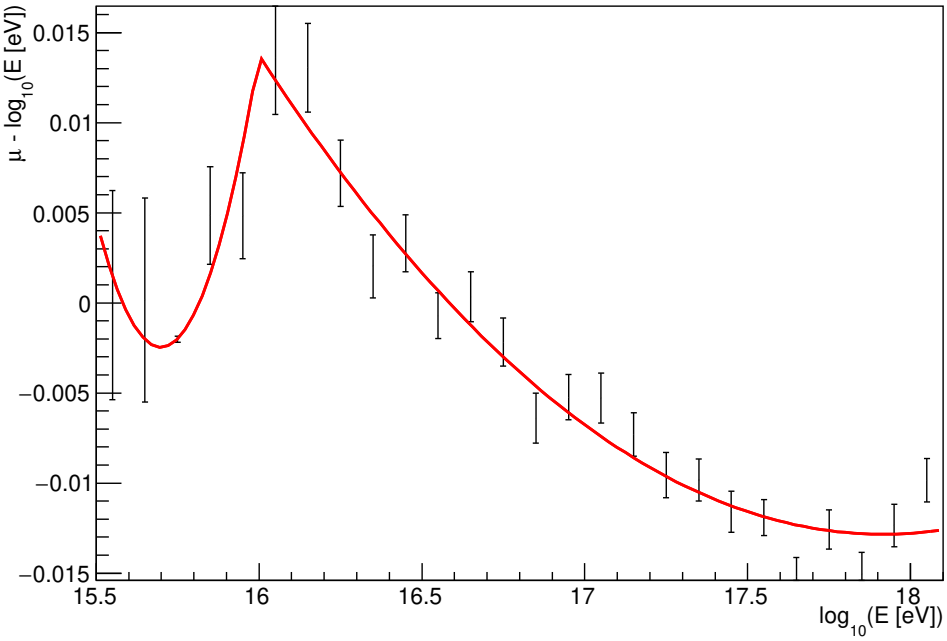

Figure C.14: The μ parameter used in the smoothing of the migration matrix as a function of the logarithm of energy. The first order dependence on the logarithm of energy is subtracted from the μ value.

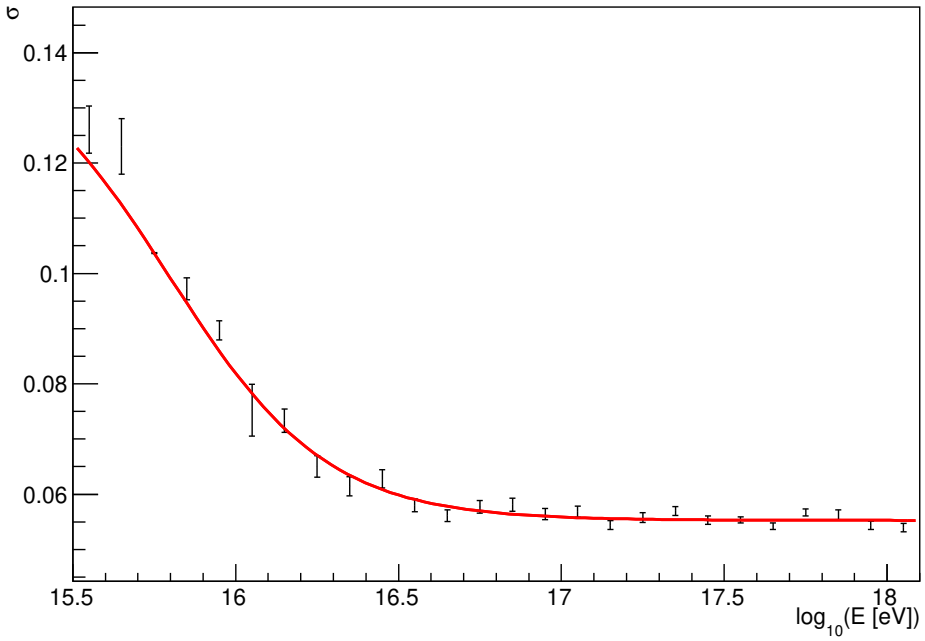

Figure C.15: The σ parameter used in the smoothing of the migration matrix as a function of the logarithm of energy. This parameter defines the resolution of the energy reconstruction.

D. Validity of Real–MC simulations

To test whether the Real–MC simulations resemble the measured data well, the distributions of reconstructed quantities are compared between the data and Real–MC events.

The distributions of R_{p} and χ_0 parameters of the shower axis, see Eq. (2.10), X and Y coordinates of the shower core defined in Appendix C, zenith and azimuth angles of the shower axis, and the total Cherenkov fraction of the light flux measured by the FD telescopes are shown in Figs. D.1–D.7, respectively. In all plots, the red and blue rectangles correspond to the proton and iron nuclei simulations and the black distributions denote the data. More precisely, the sizes of rectangles stand for the 68% confidence intervals coming from the statistical uncertainty of simulations. The same statistical uncertainties of the data are marked by black error bars.

It is worth noting that the distributions attributed to pure protons and iron nuclei are shifted between each other in several cases, e.g. in the distributions of the zenith angles in Fig. D.5. This discrepancy is caused by different longitudinal profiles of showers induced by different primaries. The corresponding uncertainty in exposure is estimated in Section 3.3.

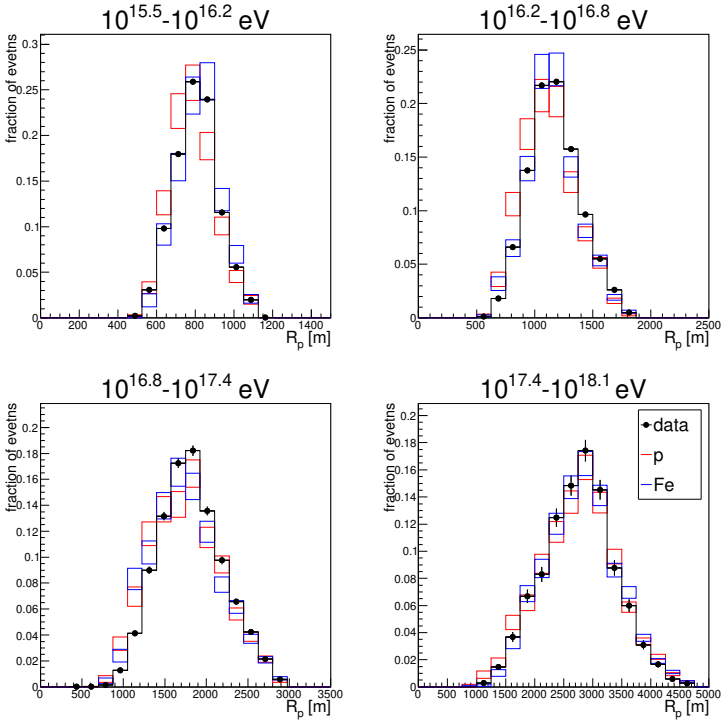

Figure D.1: Distributions of the R_{p} parameter in the data and Real–MC. Four energy bins marked in titles of the insets are shown. Blue and red rectangles correspond to the statistical uncertainties of the proton and iron nuclei simulations, respectively. Data are depicted in black with statistical error bars.

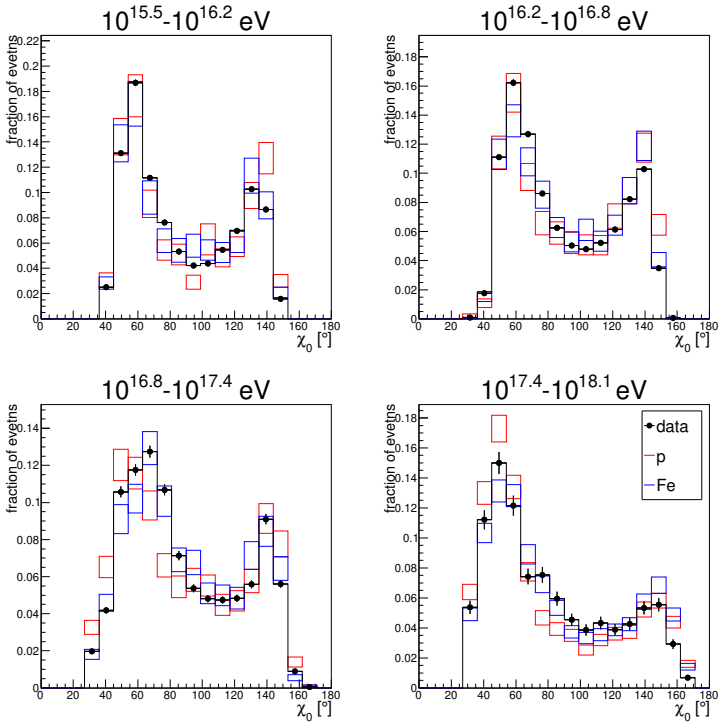

Figure D.2: Distributions of the χ_0 parameter in the data and Real–MC. Meaning of the signs is the same as in Fig. D.1.

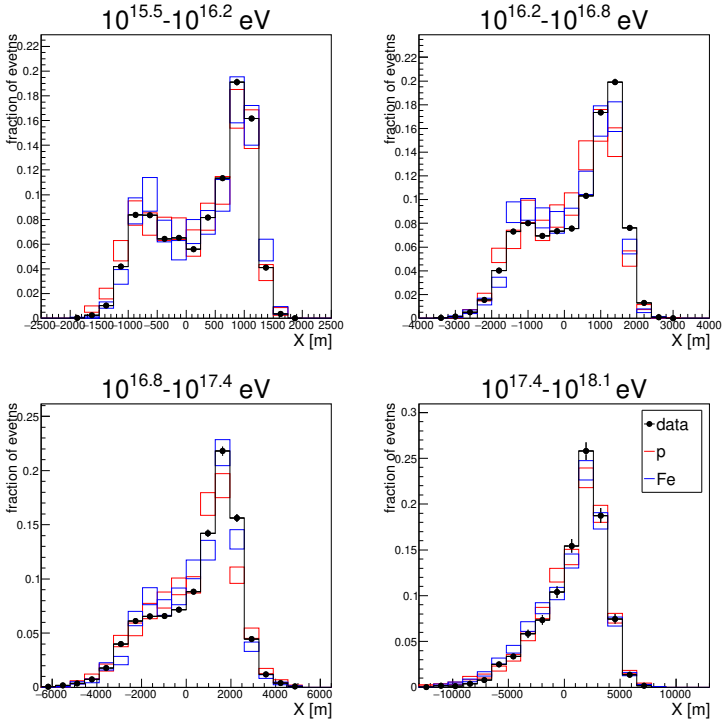

Figure D.3: Distributions of the X coordinate of the shower core in the data and Real–MC. Meaning of the signs is the same as in Fig. D.1.

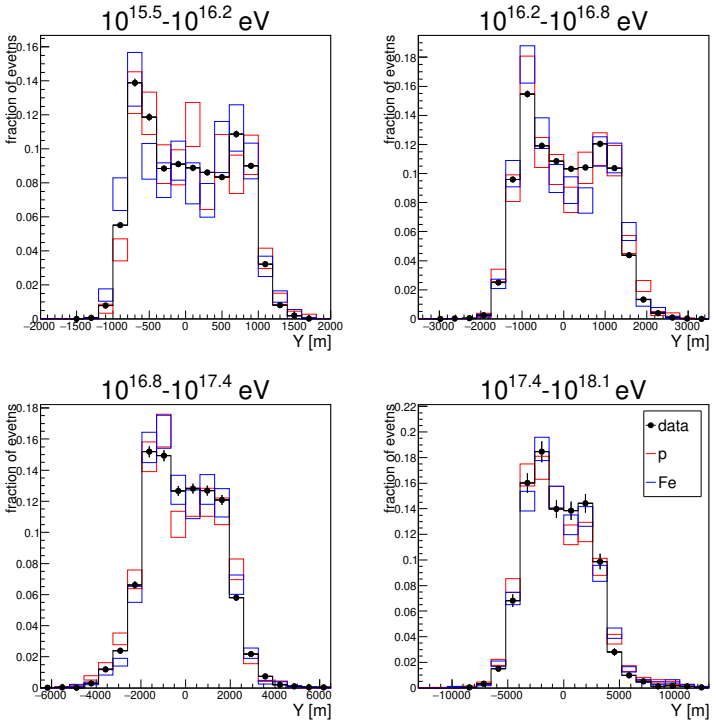

Figure D.4: Distributions of the Y coordinate of the shower core in the data and Real–MC. Meaning of the signs is the same as in Fig. D.1.

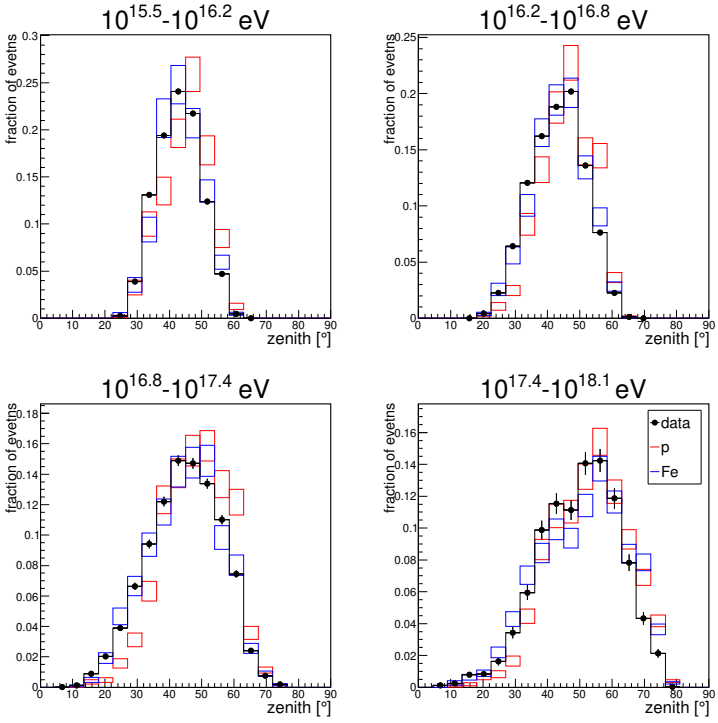

Figure D.5: Distributions of the zenith angle of the shower axis in the data and Real–MC. Meaning of the signs is the same as in Fig. D.1.

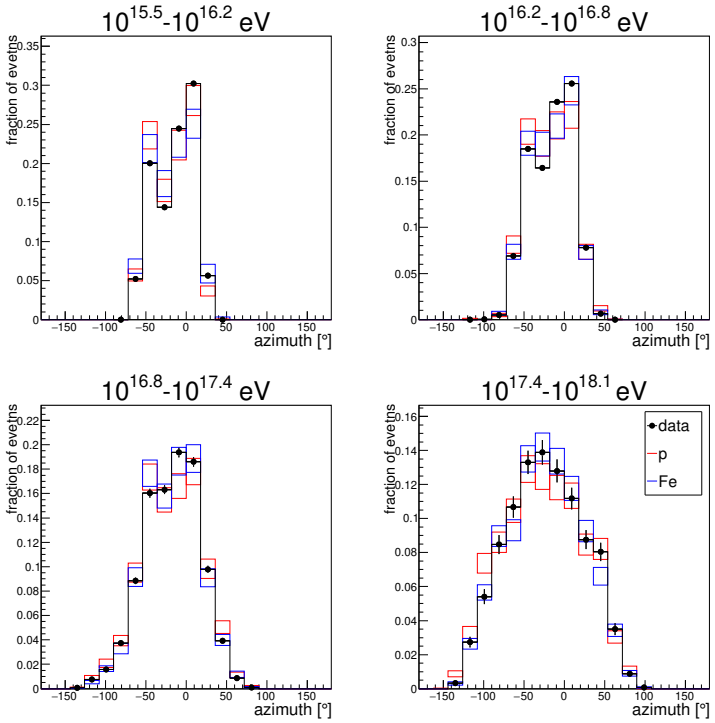

Figure D.6: Distributions of the azimuth angle of the shower axis in the data and Real–MC. Meaning of the signs is the same as in Fig. D.1.

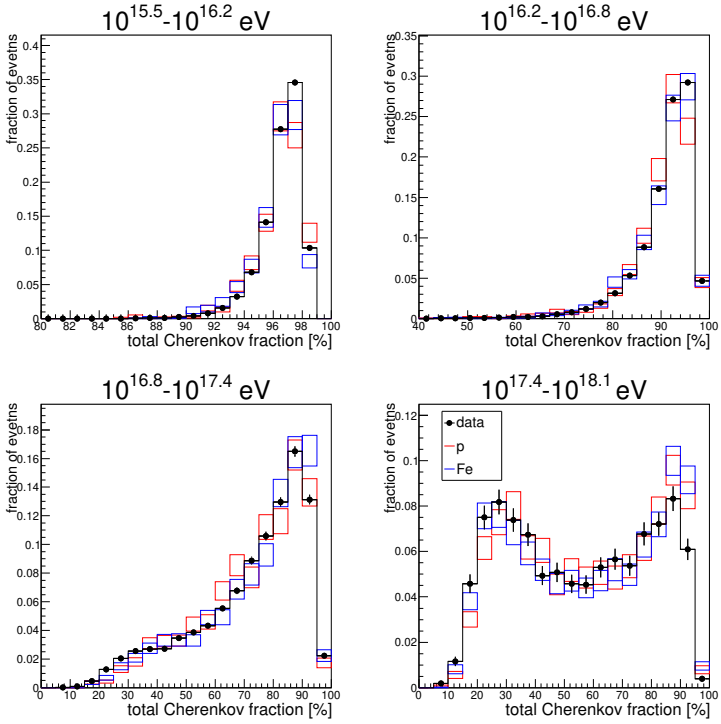

Figure D.7: Distributions of the total Cherenkov fraction of the light flux measured by the FD telescopes in the data and Real–MC. Meaning of the signs is the same as in Fig. D.1.

E. PCGF implementation in the Offline software

The profile constrained geometry fit (PCGF) is implemented in the Auger Offline software [30] as the `FdProfileConstrainedGeometryFitPG` module (`PCGF`). It is configured through the `XML` file with options described in Section E.1. The idea of the PCGF reconstruction procedure is explained in Section 2.7.

The `PCGF` module provides the telescope based reconstruction similarly to `HybridGeometryFinderWG` which means that appropriate compatible modules have to be used. Placement of the `PCGF` module in the `sequenceFile` is after the `FdAxisFinderOG` module. The module stands after `FdAxisFinderOG` because the PCGF uses the time fit for which the time fit pixels have to be identified. The identification of pixels is performed by the `FdAxisFinderOG` module for each physical set of telescopes placed at the same location (eye) separately. Otherwise, the results of `FdAxisFinderOG` are not used.

The PCGF is technically realized by two consecutive reconstruction phases out of which the first one is always a discrete scan in χ_0. In the first reconstruction phase, the `PCGF` module chooses the telescope with the largest number of time fit pixels (hottest mirror) and all consecutive calculations are performed in the `LocalCoordinateSystem` defined at the position of the hottest mirror. This is especially important for compound eyes consisting of telescopes placed at different positions like the HECO (HEAT+Coihueco). The main issue for the first scan phase is that the aperture light is not available yet. This is because the shower geometry and thus also the position of a shower image on the FD camera is not known. To deal with that, three options of the aperture light calculation can be used, see Section E.1. Two of them are based on the external `FdApertureLightFinderKG` module and are not discussed here in detail. The third option uses an internal modification of the `FdApertureLightFinderKG` code. This modification is based on an idea that although the shower axis is not estimated yet, the shower–detector plane (SDP) is already determined. Thus, the first estimate of the aperture light can be done by integrating signals in all FD pixels around the SDP at given time. The angular distance ζ' from the SDP where the signals are integrated is optimized in the code to get the best signal to noise ratio. After the first estimate of the aperture light is done, the scan in χ_0 is performed. For each χ_0, the R_p and t_0 parameters of the shower axis are determined with the use of the timing relation Eq. (2.10) and SDP projections in all telescopes of the eye which may be compound. This procedure is done by a maximum likelihood fit in which the optional corrections to the time fit discussed in Appendix A are implemented. Knowing the geometry, the complex likelihood L that includes also a part coming from the shower longitudinal profile is constructed as described in Section 2.7. Routines used for the energy deposit profile and profile fit calculations are called directly from the `FdEnergyDepositFinderKG` module. The most likely χ_{0-1} is the output of the first scan phase.

The second phase of the reconstruction can either have a form of another scan or the `Minuit` minimization. The `Minuit` minimization turned out to produce unstable results in some cases thus is not used in the energy spectrum analysis.

Using the geometry defined by χ_{0-1}, the aperture light is calculated with the use of the standard procedure re-implemented in the internal aperture light finder from the `FdApertureLightFinderKG` module. The χ_{0-1} is close to the true value of χ_0 thus the aperture light profile is accurate. Then, the very same procedure as in the first scan phase is used. In the case of the second scan, rather than the `Minuit` minimization, it is performed in the interval of $[\chi_{0-1} - 3^\circ, \chi_{0-1} + 3^\circ]$. The scan step is 10 times finer than the one set in the `XML` file for the first scan phase. If the likelihood reaches maximum at the border of the second scan interval, the interval is prolonged by another 3° in the corresponding direction.

The output of the second reconstruction phase defines the reconstructed geometry. The uncertainty of χ_0 reported by the `PCGF` module is estimated from the $+1$ difference in $-2 \log L$. Uncertainties of R_p and t_0 are marginalized for the reconstructed χ_0 and come from the maximum likelihood fit that is used to calculate them.

E.1 XML configuration

Options that can be configured in the `PCGF XML` read:

- `apLightMethod` – method for the aperture light calculation used inside the `PCGF` module only
  - `eInternal` – internal method described above, pixels around the SDP are used in the first scan phase
  - `eExternal` – aperture light calculated by `ApertureLightFinderKG` before the `PCGF` is used
  - `eCallForEach` – `ApertureLightFinderKG` is called for each trial geometry
- `eyeCut` – to use the PCGF only for selected eyes specified in a format `abcdef` where `a-f` are 0 (do not use PCGF) or 1 (use PCGF) consecutively for HECO, HEAT, Coihueco, Loma Amarilla, Los Morados, and Los Leones eyes, respectively
- `checkUnderground` – geometries that produce light reaching any of the FD telescopes from behind (unphysical) are skipped
- `prescan` – additional scan phase is put before the first scan phase with 4 times larger step than the one defined in `scanStep`; the first scan phase is then done only in the interval of χ_0 between the first and last values with non–infinite value of L (infinite denotes skipped geometries or failed fits)
- `scanOnly`
  - `0` – Minuit minimization in the second reconstruction phase
  - `1` – scan in the second reconstruction phase
- `scanStep` – scan step used in the first scan phase

- `scanStart` – starting χ_0 of the first scan phase or the `prescan` if applied
- `scanStop` – ending χ_0 of the first scan phase or the `prescan` if applied
- `leavingAtmoIsError` – shower profiles for which the CFM predicts light coming from regions above the atmosphere defined in Offline are skipped
- `onlyDirectLight` – only the direct Chernekov light contribution to the light flux is used in the longitudinal profile reconstruction to calculate L
- `delZeroLightFlux` – measured light fluxes in time bins compatible within statistical uncertainty with zero are removed from the light flux used to calculate L
- `useLightFlux` – use the longitudinal profile fit based on the maximum likelihood fit of the measured light flux, otherwise the χ^2 fit of the Gaisser–Hillas function to the energy deposit profile is used
- `useNoiseBins` – include time bins with no signal in FD pixels into the light profile used to determine L
- `skipNegativeT0` – geometries with negative t_0 are skipped; such events are going from behind the hottest mirror telescope and do not produce Cherenkov light flux in its aperture
- `antiAliasingFilterCorrection` – correction for the anti–aliasing filter response of the FD electronics is applied [A15]
- `TimeFitModel` – model for the light propagation through the atmosphere according to Ref. [82]
  - 0 – vacuum atmosphere
  - 1 – reduced speed of light
- `TimeFitDeexcitation` – de–excitation time connected to the N_2 fluorescence is taken into account in the time fit [82]
- `emissionPointCorrection` – correction to the apparent shower position in the time fit explained in Appendix A
- `denseMatrixDim` – minimum dimension of the Cherenkov–Fluorescence Matrix used in the longitudinal profile fit [A16]
- `profile` – settings used in the longitudinal profile determination, identical with options in the `FdEnergyDepositFinderKG` configuration
- `zetaOptimization` – settings for the internal aperture light finder, identical with the `FdApertureLightFinderKG` configuration
  - `borderMargin` – to apply different margin between the `BorderPixels` and the position of the shower image on the FD camera
    - 0 – the ζ angle is used like in the `FdApertureLightFinderKG` module

The configuration used in the reconstruction of the data for the energy spectrum analysis reads:

```
<apLightMethod> eInternal </apLightMethod>
<eyeCut> 100000 </eyeCut>
<checkUnderground> 1 </checkUnderground>
<prescan> 1 </prescan>
<scanOnly> 1 </scanOnly>
<scanStep unit="degree"> 1.  </scanStep>
<scanStart unit="degree"> 1.  </scanStart>
<scanStop unit="degree"> 179.  </scanStop>
<leavingAtmoIsError> 0 </leavingAtmoIsError>
<onlyDirectLight> 0 </onlyDirectLight>
<delZeroLightFlux> 0 </delZeroLightFlux>
<useLightFlux> 1 </useLightFlux>
<useNoiseBins> 1 </useNoiseBins>
<skipNegativeT0> 1 </skipNegativeT0>
<antiAliasingFilterCorrection> 1 </antiAliasingFilterCorrection>
<TimeFitModel> 0 </TimeFitModel>
<TimeFitDeexcitation> 0 </TimeFitDeexcitation>
<emissionPointCorrection> 1 </emissionPointCorrection>
<denseMatrixDim> 100 </denseMatrixDim>

<profile>
  <gaisserHillasType> eClassic </gaisserHillasType>
  <gaisserHillasShapeParameters type="eClassic">
    <par id="1">
      <name> eX0 </name>
      <unit> g/cm2 </unit>
      <mean> -121*g/cm2 </mean>
      <sigma> 172*g/cm2 </sigma>
      <range unit="g/cm2"> -1000 500 </range>
      <step unit="g/cm2"> 10 </step>
    </par>
    <par id="2">
      <name> eLambda </name>
      <unit> g/cm2 </unit>
      <mean> 61*g/cm2 </mean>
      <sigma> 13*g/cm2 </sigma>
      <range unit="g/cm2"> 10 150 </range>
      <step unit="g/cm2"> 5 </step>
    </par>
  </gaisserHillasShapeParameters>
  <kUnivConstrained>
    <constrained> 1 </constrained>
    <function variables="Ecal">
      332.6*g/cm2 + 13.67*g/cm2 * log10(Ecal/eV)
    </function>
```

```
    <ksigma unit="g/cm/cm"> 29.  </ksigma>
  </kUnivConstrained>
</profile>

<zetaOptimization>
  <minZetaAngle unit="degree"> 0.5 </minZetaAngle>
  <maxZetaAngle unit="degree"> 4.5 </maxZetaAngle>
  <stepZetaAngle unit="degree"> 0.1 </stepZetaAngle>
  <safetyMargin unit="degree"> 0.5 </safetyMargin>
  <borderMargin unit="degree"> 0 </borderMargin>
</zetaOptimization>
```

Bibliography

[1] The Pierre Auger Project Design Report. Technical report, 1996. FERMILAB-PUB-96-024.

[2] A. Aab et al. The Pierre Auger Cosmic Ray Observatory. *Nucl. Instrum. Meth. A*, 798:172–213, 2015.

[3] J. J. Beatty and S. Westerhoff. The highest-energy cosmic rays. *Annual Review of Nuclear and Particle Science*, 59(1):319–345, 2009.

[4] M. Tanabashi et al. Review of Particle Physics. *Phys. Rev. D*, 98(3):030001, 2018.

[5] A. Haungs, H. Rebel, and M. Roth. Energy spectrum and mass composition of high-energy cosmic rays. *Rept. Prog. Phys.*, 66:1145–1206, 2003.

[6] W. Heitler. *Quantum theory of radiation*. 1954.

[7] J. Matthews. A Heitler model of extensive air showers. *Astropart. Phys.*, 22:387–397, 2005.

[8] T. Bergmann, R. Engel, D. Heck, N. N. Kalmykov, S. Ostapchenko, T. Pierog, T. Thouw, and K. Werner. One-dimensional Hybrid Approach to Extensive Air Shower Simulation. *Astropart. Phys.*, 26:420–432, 2007.

[9] D. Heck, J. Knapp, J. N. Capdevielle, G. Schatz, and T. Thouw. *CORSIKA: a Monte Carlo code to simulate extensive air showers.* February 1998. FZKA–6019.

[10] T. K. Gaisser and A. M. Hillas. Reliability of the method of constant intensity cuts for reconstructing the average development of vertical showers. In *International Cosmic Ray Conference*, volume 8 of *International Cosmic Ray Conference*, pages 353–357, 1977.

[11] T. Pierog and K. Werner. EPOS Model and Ultra High Energy Cosmic Rays. *Nucl. Phys. Proc. Suppl.*, 196:102–105, December 2009.

[12] T. Pierog, Iu. Karpenko, J. M. Katzy, E. Yatsenko, and K. Werner. EPOS LHC: Test of collective hadronization with data measured at the CERN Large Hadron Collider. *Phys. Rev. C*, 92(3):034906, 2015.

[13] S. Ostapchenko. Monte Carlo treatment of hadronic interactions in enhanced Pomeron scheme: I. QGSJET-II model. *Phys. Rev. D*, 83:014018, 2011.

[14] S. Ostapchenko. LHC data on inelastic diffraction and uncertainties in the predictions for longitudinal extensive air shower development. *Phys. Rev. D*, 89(7):074009, 2014.

[15] R. S. Fletcher, T. K. Gaisser, P. Lipari, and T. Stanev. Sibyll: An event generator for simulation of high energy cosmic ray cascades. *Phys. Rev. D*, 50:5710–5731, November 1994.

[16] F. Riehn, R. Engel, A. Fedynitch, T. K. Gaisser, and T. Stanev. The hadronic interaction model Sibyll 2.3c and extensive air showers. 2019. arXiv:1912.03300 [hep-ph].

[17] J. R. Horandel. Cosmic rays from the knee to the second knee: 10^{14} to 10^{18} eV. *Mod. Phys. Lett. A*, 22:1533–1552, 2007.

[18] A. Yushkov for the Pierre Auger Collaboration. Mass composition of cosmic rays with energies above $10^{17.2}$ eV from the hybrid data of the Pierre Auger Observatory. *PoS*, ICRC2019:482, 2019.

[19] J. Gonzalez. Measuring the Muon Content of Air Showers with IceTop. In *20th International Symposium on Very High Energy Cosmic Ray Interactions (ISVHECRI) Nagoya, Japan*, 2018.

[20] H. P. Dembinski, R. Engel, A. Fedynitch, T. K. Gaisser, F. Riehn, and T. Stanev. Data–driven model of the cosmic–ray flux and mass composition from 10 GeV to 10^{11} GeV. *PoS*, ICRC2017:533, 2018.

[21] A. Aab et al. The Pierre Auger Observatory Upgrade - Preliminary Design Report. 2016. arXiv:1604.03637 [astro-ph.IM].

[22] J. Abraham et al. The Fluorescence Detector of the Pierre Auger Observatory. *Nucl. Instrum. Meth. A*, 620:227–251, 2010.

[23] M. Ave et al. Measurement of the pressure dependence of air fluorescence emission induced by electrons. *Astropart. Phys.*, 28:41–57, 2007.

[24] M. Ave et al. Precise measurement of the absolute fluorescence yield of the 337 nm band in atmospheric gases. *Astropart. Phys.*, 42:90–102, 2013.

[25] A. Castellina. AugerPrime: the Pierre Auger Observatory Upgrade. *EPJ Web Conf.*, 210:06002, 2019.

[26] J. Abraham et al. Properties and performance of the prototype instrument for the Pierre Auger Observatory. *Nucl. Instrum. Meth. A*, 523:50–95, 2004.

[27] A. Etchegoyen. AMIGA, Auger Muons and Infill for the Ground Array. In *Proceedings, 30th International Cosmic Ray Conference (ICRC 2007): Merida, Yucatan, Mexico, July 3-11, 2007*, volume 5, pages 1191–1194, 2007.

[28] V. Revenu. Overview of MHz air shower radio experiments and results. *AIP Conf. Proc.*, 1535(1):56–62, 2013.

[29] Ch. Williams. Microwave Detection of Cosmic Ray Air Showers at the Pierre Auger Observatory, an R&D Effort. *Phys. Procedia*, 37:1341–1348, 2012.

[30] S. Argiro et al. The Offline Software Framework of the Pierre Auger Observatory. *Nucl. Instrum. Meth. A*, 580:1485–1496, 2007.

[31] A. Aab et al. The Pierre Auger Observatory: Contributions to the 36^{th} International Cosmic Ray Conference (ICRC 2019). 2019. arXiv:1909.09073 [astro-ph.HE].

[32] R. Brun and F. Rademakers. ROOT - An object oriented data analysis framework. *Nucl. Instrum. Meth. A*, 389:81–86, February 1997.

[33] M. Unger, B. R. Dawson, R. Engel, F. Schussler, and R. Ulrich. Reconstruction of Longitudinal Profiles of Ultra-High Energy Cosmic Ray Showers from Fluorescence and Cherenkov Light Measurements. *Nucl. Instrum. Meth. A*, 588:433–441, 2008.

[34] R. Ulrich, J. Bluemer, R. Engel, et al. Manual of fluorescence detector simulation in Offline. GAP2008–014.

[35] M. Unger. Shower Profile Reconstruction from Fluorescence and Cherenkov light. GAP2006–010.

[36] F. Nerling, J. Bluemer, R. Engel, and M. Risse. Universality of electron distributions in high-energy air showers: Description of Cherenkov light production. *Astropart. Phys.*, 24:421–437, 2006.

[37] M. Giller, A. Smialkowski, and G. Wieczorek. An extended universality of electron distributions in cosmic ray showers of high energies and its application. *Astropart. Phys.*, 60:92–104, 2015.

[38] A. Schmidt, T. Asch, M. Kleifges, H.-J. Mathes, and H. Gemmeke. New Third Level Trigger for the Fluorescence Telescopes. GAP2007–118.

[39] D. Kuempel, K.-H. Kampert, and M. Risse. Geometry reconstruction of fluorescence detectors revisited. *Astropart. Phys.*, 30:167–174, 2008.

[40] P. Sokolsky. Final results from the High Solution Fly's Eye (HiRes) experiment. *Nucl. Phys. Proc. Suppl.*, 212-213:74–78, 2011.

[41] A. Aab et al. Data-driven estimation of the invisible energy of cosmic ray showers with the Pierre Auger Observatory. *Phys. Rev. D*, 100(8):082003, 2019.

[42] K. Louedec and R. Losno. Atmospheric aerosols at the Pierre Auger Observatory and environmental implications. *Eur. Phys. J. Plus*, 127:97, 2012.

[43] B. Keilhauer and M. Will. Description of Atmospheric Conditions at the Pierre Auger Observatory Using Meteorological Measurements and Models. *Eur. Phys. J. Plus*, 127:96, 2012.

[44] S. Y. Ben Zvi et al. The Lidar System of the Pierre Auger Observatory. *Nucl. Instrum. Meth. A*, 574:171–184, 2007.

[45] J. Chirinos. Remote Sensing of Clouds using Satellites, Lidars, CLF/XLF and IR Cameras at the Pierre Auger Observatory. *EPJ Web Conf.*, 89:03012, 01 2015.

[46] P. Abreu et al. Identifying Clouds over the Pierre Auger Observatory using Infrared Satellite Data. *Astropart. Phys.*, 50-52:92–101, 2013.

[47] P. Abreu et al. Description of Atmospheric Conditions at the Pierre Auger Observatory using the Global Data Assimilation System (GDAS). *Astropart. Phys.*, 35:591–607, 2012.

[48] P. Abreu et al. Techniques for Measuring Aerosol Attenuation using the Central Laser Facility at the Pierre Auger Observatory. *JINST*, 8:P04009, 2013.

[49] M. Mostafa. The Hybrid Activities of the Pierre Auger Observatory. *Nucl. Phys. Proc. Suppl.*, 165:50–58, 2007.

[50] T. Fujii et al. Detection of ultra–high energy cosmic ray showers with a single–pixel fluorescence telescope. *Astropart. Phys.*, 74:64–72, 2016.

[51] T. Fujii et al. Observing ultra–high energy cosmic rays with prototypes of the Fluorescence detector Array of Single–pixel Telescopes (FAST) in both hemispheres. *PoS*, ICRC2019:259, 2019.

[52] T. Abu-Zayyad et al. The surface detector array of the Telescope Array experiment. *Nucl. Instrum. Meth. A*, 689:87–97, 2013.

[53] R. U. Abbasi et al. First observation of the Greisen–Zatsepin–Kuzmin suppression. *Phys. Rev. Lett.*, 100:101101, 2008.

[54] R. U. Abbasi et al. The Cosmic-Ray Energy Spectrum between 2 PeV and 2 EeV Observed with the TALE detector in monocular mode. *Astrophys. J.*, 865(1):74, 2018.

[55] D. Veberic and M. Roth. SD Reconstruction; Offline Reference Manual. GAP2005–035.

[56] K. Kamata and J. Nishimura. The Lateral and the Angular Structure Functions of Electron Showers. *Prog. Theor. Phys. Suppl.*, 6:93–155, 1958.

[57] J. Hersil, I. Escobar, D. Scott, G. Clark, and S. Olbert. Observations of extensive air showers near the maximum of their longitudinal development. *Phys. Rev. Lett.*, 6:22–23, Jan 1961.

[58] V. Verzi for the Pierre Auger Collaboration. Measurement of the energy spectrum of ultra–high energy cosmic rays using the Pierre Auger Observatory. *PoS*, ICRC2019:450, 2019.

[59] A. Aab et al. Reconstruction of Inclined Air Showers Detected with the Pierre Auger Observatory. *JCAP*, 1408:019, 2014.

[60] B. Dawson for the Pierre Auger Collaboration. The Energy Scale of the Pierre Auger Observatory. *PoS*, ICRC2019:231, 2019.

[61] I. Valino for the Pierre Auger Collaboration. The flux of ultra–high energy cosmic rays after ten years of operation of the Pierre Auger Observatory. *PoS*, ICRC2015:271, 2016.

[62] H. P. Dembinski et al. Report on Tests and Measurements of Hadronic Interaction Properties with Air Showers. In *Ultra High Energy Cosmic Rays (UHECR 2018) Paris, France, October 8-12, 2018*, 2019.

[63] P. Abreu et al. The exposure of the hybrid detector of the Pierre Auger Observatory. *Astropart. Phys.*, 34:368–381, 2011.

[64] I. C. Maris, M. Roth, F. Schüssler, and M. Unger. Combining the energy spectra measured at the Pierre Auger Observatory. GAP2007–090.

[65] A. Coleman for the Pierre Auger Collaboration. Measurement of the cosmic ray flux near the second knee with the Pierre Auger Observatory. *PoS*, ICRC2019:225, 2019.

[66] M. Amenomori et al. The All–particle spectrum of primary cosmic rays in the wide energy range from 10^{14} eV to 10^{17} eV observed with the Tibet–III air–shower array. *Astrophys. J.*, 678:1165–1179, 2008.

[67] W. D. Apel, J. C. Arteaga-Velázquez, K. Bekk, M. Bertaina, J. Blümer, H. Bozdog, I. M. Brancus, P. Buchholz, E. Cantoni, A. Chiavassa, et al. The spectrum of high–energy cosmic rays measured with KASCADE–Grande. *Astroparticle Physics*, 36(1):183–194, Aug 2012.

[68] M. G. Aartsen et al. Cosmic ray spectrum and composition from PeV to EeV using 3 years of data from IceTop and IceCube. *Phys. Rev. D*, 100(8):082002, 2019.

[69] A. A. Ivanov, S. P. Knurenko, and I. Ye. Sleptsov. Measuring extensive air showers with Cherenkov light detectors of the Yakutsk array: the energy spectrum of cosmic rays. *New Journal of Physics*, 11(6):065008, Jun 2009.

[70] V. V. Prosin et al. Results from Tunka–133 (5 years observation) and from the Tunka–HiSCORE prototype. *EPJ Web Conf.*, 121:03004, 2016.

[71] O. Deligny for the Pierre Auger and Telescope Array Collaborations. The energy spectrum of ultra–high energy cosmic rays measured at the Pierre Auger Observatory and at the Telescope Array. *PoS*, ICRC2019:234, 2019.

[72] B. Peters. Primary cosmic radiation and extensive air showers. *Il Nuovo Cimento*, 22(4):800–819, November 1961.

[73] T. K. Gaisser, T. Stanev, and S. Tilav. Cosmic Ray Energy Spectrum from Measurements of Air Showers. *Front. Phys.(Beijing)*, 8:748–758, 2013.

[74] Y. Tsunesada. Highlights from Telescope Array. 2011. arXiv:1111.2507 [astro-ph.HE].

[75] V. S. Berezinsky and S. I. Grigor'eva. A Bump in the ultrahigh–energy cosmic ray spectrum. *Astron. Astrophys.*, 199:1–12, 1988.

[76] K. Greisen. End to the cosmic ray spectrum? *Phys. Rev. Lett.*, 16:748–750, 1966.

[77] G. T. Zatsepin and V. A. Kuzmin. Upper limit of the spectrum of cosmic rays. *JETP Lett.*, 4:78–80, 1966.

[78] A. Schulz and M. Roth. Details and technical notes on fitting the energy spectrum. GAP2017–043.

[79] D. Gora, R. Engel, D. Heck, P. Homola, H. Klages, J. Pekala, M. Risse, B. Wilczynska, and H. Wilczynski. Universal lateral distribution of energy deposit in air showers and its application to shower reconstruction. *Astropart. Phys.*, 24:484–494, 2006.

[80] A. M. K. Awad. *Measurements of the maximum depth of air shower profiles at LHC energies with the High–Elevation Auger Telescopes*. PhD thesis, Universität Karlsruhe, 2019. GAP2019–037.

[81] E.-J. Ahn, R. Engel, T. K. Gaisser, P. Lipari, and T. Stanev. Cosmic ray interaction event generator SIBYLL 2.1. *Phys. Rev. D*, 80:094003, Nov 2009.

[82] D. Kuempel. Geometry Reconstruction of Fluorescence Detectors Revisited. GAP2007–099.

Author's publications

[A1] V. Novotny. Study of the highest energy cosmic rays. Master's thesis, Charles University in Prague, 2013.

[A2] V. Novotny, D. Nosek, and J. Vicha. Accuracy of shower parameters in stereo reconstruction. GAP2013–110.

[A3] V. Novotny, D. Nosek, and J. Vicha. Stereo Reconstruction at the Pierre Auger Observatory. In J. Safrankova and J. Pavlu, editors, *WDS'14 Proceedings of Contributed Papers - Physics*, pages 48–55, Prague, 2014. MATFYZPRESS.

[A4] V. Novotny and D. Nosek. Shower velocity determined in stereo method. GAP2016–010.

[A5] V. Novotny and D. Nosek. Velocity of showers seen in stereo regime. GAP2016–053.

[A6] V. Novotny and D. Nosek. Discrepancies in laser shot velocities. GAP2016–054.

[A7] V. Novotny, D. Nosek, and J. Blazek. Mass–dependent parameters of extensive air showers with anomalous longitudinal profiles. *Astron. Nachr.*, 340(1-3):234–236, 2019.

[A8] V. Novotny, D. Nosek, and J. Ebr. A branching model for hadronic air showers. *PoS*, ICRC2015:500, 2016.

[A9] V. Novotny and D. Nosek. Description of longitudinal profiles of showers dominated by Cherenkov light. GAP2017–022.

[A10] V. Novotny and D. Nosek. Description of longitudinal profiles of showers dominated by Cherenkov light. *PoS*, ICRC2017:338, 2018.

[A11] V. Novotny, D. Nosek, and J. Vicha. Energy spectrum of cosmic rays derived from Cherenkov–dominated data sample. GAP2017–067.

[A12] V. Novotny, D. Nosek, and J. Vicha. Energy spectrum of cosmic rays derived from Cherenkov–dominated data sample – HECO update. GAP2018–055.

[A13] V. Novotny. Energy spectrum of cosmic rays measured with the Pierre Auger Observatory. In *Proceedings, 52nd Rencontres de Moriond on Very High Energy Phenomena in the Universe: La Thuile, Italy, March 18-25, 2017*, pages 23–30, 2017.

[A14] V. Novotny for the Pierre Auger Collaboration. Measurement of the spectrum of cosmic rays above $10^{16.5}$ eV with Cherenkov–dominated events at the Pierre Auger Observatory. *PoS*, ICRC2019:374, 2019.

[A15] V. Novotny. Energy reconstruction of Cherenkov–rich events in HEAT. Auger Collaboration Meeting, March 2016.

[A16] V. Novotny. Status of the spectrum from Cherenkov–dominated events. Auger Collaboration Meeting, November 2019.

[A17] V. Novotny. prezentation in the phone call of the Cherenkov–rich events reconstruction working group. `https://www.auger.unam.mx/AugerWiki/CherenkovRichPhoneMeetings`, 7 September, 2017.

[A18] V. Novotny, E. dos Santos, J. Vicha, and A. Yushkov. Napoli + Praha library. Comparison between the Napoli and Praha CORSIKA productions. GAP2019–068.

List of Figures

List of Tables

List of Abbreviations

ADC	analog–to–digital converter
ADST	Advanced Data Summary Trees
AERA	Auger Engineering Radio Array
AMBER	Air–shower Microwave Bremsstrahlung Experimental Radiometer
AMIGA	Auger Muons and Infill for the Ground Array
CDF	cumulative distribution function
CFM	Cherenkov–Fluorescence Matrix
CIC	constant intensity cut
CLF	central laser facility
CR	cosmic rays
EAS	extensive air shower
EASIER	Extensive Air Shower Identification using Electron Radiometer
EM	electromagnetic
FADC	flash analog–to–digital converter
FAST	Fluorescence detector Array of Single–pixel Telescopes
FD	fluorescence detector
FLT	First Level Trigger
FV	fiducial volume
GEF	Gaussian function with exponential tails
GH	Gaisser–Hillas
GSF	global spline fit
HEAT	High Elevation Auger Telescopes
LDF	lateral distribution function
MC	Monte Carlo
MIDAS	Microwave Detection of Air Showers
PCGF	profile constrained geometry fit
SD	surface detector
SDP	shower–detector plane
SLT	Second Level Trigger
TLT	Third Level Trigger
UHECR	ultra high energy cosmic rays
VEM	vertical equivalent muon
XLF	extended laser facility